GEOCIÊNCIAS
USP
INSTITUTO DE GEOCIÊNCIAS

DISSERTAÇÃO DE MESTRADO
N° 815

STRUCTURAL CONTROL AND GENESIS OF THE AU-QUARTZ VEINS FROM THE SERRA DO CAVALO MAGRO OROGENIC GOLD DEPOSIT, SOUTHERN RIBEIRA BELT, BRAZIL.

Isaac Siles Malta

Prof. Dr. Frederico Meira Faleiros
Orientador

Pós Graduação em Geociências
Programa de Mineralogia e Petrologia

USP
Universidade
de São Paulo

UNIVERSIDADE DE SÃO PAULO
INSTITUTO DE GEOCIÊNCIAS

Structural control and genesis of the Au-quartz veins from the Serra do Cavalo Magro orogenic gold deposit, southern Ribeira Belt, Brazil

ISAAC SILES MALTA

Dissertação apresentada ao Programa de Geociências (Mineralogia e Petrologia) para obtenção do título de Mestre em Ciências.

Área de concentração: Petrologia Ígnea e Metamórfica.

Orientador: Prof. Dr. Frederico Meira Faleiros

SÃO PAULO

2018

Serviço de Biblioteca e Documentação do IGc/USP
Ficha catalográfica gerada automaticamente com dados fornecidos pelo(a) autor(a)
via programa desenvolvido pela Seção Técnica de Informática do ICMC/USP

Bibliotecários responsáveis pela estrutura de catalogação da publicação:
Sonia Regina Yole Guerra - CRB-8/4208 | Anderson de Santana - CRB-8/6658

Malta, Isaac Siles
Structural control and genesis of the Au-quartz veins from the Serra do Cavalo Magro orogenic gold deposit, southern Ribeira Belt, Brazil / Isaac Siles Malta; orientador Frederico Meira Faleiros. -- São Paulo, 2018.
67 p.

Dissertação (Mestrado - Programa de Pós-Graduação em Mineralogia e Petrologia) -- Instituto de Geociências, Universidade de São Paulo, 2018.

1. Depósito de ouro orogênico da Serra do Cavalo Magro. 2. Veios de quartzo auríferos. 3. Processos de falhamento sísmico. 4. Inclusões fluidas. 5. Precipitação de ouro. I. Faleiros, Frederico Meira, orient. II. Título.

UNIVERSIDADE DE SÃO PAULO
INSTITUTO DE GEOCIÊNCIAS

Structural control and genesis of the Au-quartz veins from the Serra do Cavalo Magro orogenic gold deposit, southern Ribeira Belt, Brazil

ISAAC SILES MALTA

Orientador: Prof. Dr. Frederico Meira Faleiros

Dissertação de Mestrado

Nº 815

COMISSÃO JULGADORA

Dr. Frederico Meira Faleiros

Drª. Maria José Maluf de Mesquita

Dr. Rafael Rodrigues de Assis

SÃO PAULO

2018

To my wife,

Bruna Coldebella

ACKNOWLEDGEMENTS

First of all, I would like to express my gratitude to my advisor Prof. Dr. Frederico Meira Faleiros for the useful comments, remarks, and engagement through the learning process of this master's dissertation. He always kept the office door open whenever I ran into a trouble or had a question about my research or writing.

Thanks to Prof. Dr. Renato de Moraes and Prof. Dr. Gergely A. J. Szabó for introducing me to the metamorphic petrology world and gave me the chance to work as a T.A. during field works in the Metamorphic Petrology Course for undergraduate students.

I would like to thank Prof. Dr. Maria José M. Mesquita and Prof. Dr. Rafael Rodrigues de Assis for provided valuable comments and suggestions on the master's dissertation.

I would like to thank Dr. Marcelo Barbosa de Andrade (Physics Institute of São Carlos - USP) for the support in performing laser Raman spectroscopic analyses in fluid inclusions.

I thank the support of the technical and administrative staff of the Geosciences Institute (USP), in particular to Samuel, Marcos, Leandro, José Paulo, Rosa, Roger, Sônia, and Angélica.

Thanks to my colleagues Thereza, Dina, Fabíola, and Fernando. A special thank goes to Melina for helping me in the formatting of images and graphics.

My sincere thanks goes to the forest rangers of the Parque Estadual de Intervales (SP) Paulinho and Zé for assisting me during field works and in collecting rock samples.

Many thanks go to my family from Cuiabá (MT), even though you are so far away, regular contact and encouragement has kept me focused on finishing this master's dissertation.

I would like to thank my wonderful wife Bruna Coldebella for the patience and constant support she gave me along the two years of work.

Finally, but not least, this project would not be possible without the financial support of the São Paulo Research Foundation (FAPESP), grant 2016/11584-1.

"A man who dares to waste one hour of time has not discovered the value of life"

Charles Darwin

RESUMO

O depósito de ouro orogênico da Serra do Cavalo Magro localiza-se na Faixa Ribeira Meridional, Brasil. Os veios de quartzo de ouro estão hospedados em rochas metassedimentares e metabásicas caliminianas (1500-1450 Ma) e rochas graníticas ediacaranas (610-600 Ma). A modelagem petrológica indica que as condições de pico metamórfico das rochas hospedeiras imediatas aos veios ocorreram a 560 °C e 7 kbar (clorita-biotita filito) e a 625 °C e 6,8 kbar (granada-biotita filito). A mineralização aurífera ocorre tanto em veios de quartzo extensionais como em veios de cisalhamento estruturalmente controlados por zonas de cisalhamento transcorrentes sinistrais de segunda e terceira ordem de direção NE. Os veios extensionais verticais e sub-horizontais NNW são orientados entre 55 a 85° em relação aos planos de falhas, indicando que as zonas de cisalhamento foram severamente desorientadas para reativação friccional. A deformação nas zonas de cisalhamento foi acomodada pela recristalização de agregados de quartzo por bulging, enquanto agregados de feldspato derivados de protólitos graníticos sofreram fluxo cataclástico ou foram substituídos por epidoto-sericita produzindo filonitos. O ouro precipitou durante estágios de deformação dos veios ao longo de microfraturas em veios de cisalhamento milonitizados com quartzo previamente submetido à recristalização por bulging. Os fluidos mineralizantes registram a coexistência de inclusões fluidas de CO_2-N_2, H_2O-NaCl-$CaCl_2$ e H_2O-CO_2-N_2-NaCl-$CaCl_2$ de baixas a moderadas salinidades (1-18% em peso de NaCl eq.). Dados microtermométricos indicam condições de aprisionamento de 240 a 260 °C e de 0.4 a 2.5 kbar, registrando variações hidrostáticas a supralitostáticas da pressão de fluidos. Inclusões hipersalinas aquosas e multifásicas (H_2O-NaCl-$CaCl_2$-KCl) de alta temperatura (475 °C, 25-33% em peso de NaCl eq.) são consideradas não relacionadas com a mineralização de ouro. Fortes flutuações de pressão de fluidos na ordem de 0.4 a 1.6 kbar estão associadas a ciclos de terremotos e ao comportamento falha-válvula. Nesse cenário, a mineralização aurífera estaria associada à imiscibilidade de fluidos. Há evidências de mistura fluidos restrita, mas esse processo é interpretado como não relacionado à mineralização. Dados geocronológicos disponíveis e relações estruturais-petrológicas das rochas hospedeiras e zonas de cisalhamento sugerem que a mineralização foi formada entre 580-540 Ma durante episódios após o pico metamórfico. Os fluidos hidrotermais mineralizantes foram provavelmente produzidos por reações de devolatilização durante o metamorfismo progressivo em níveis profundos, os quais foram subsequentemente canalizados ao longo de sistemas de falhas e zonas de cisalhamentos transcorrentes em rochas que já foram metamorfizadas e devolatilizadas em épocas anteriores.

Palavras-chave: Depósito de ouro orogênico da Serra do Cavalo Magro; Veios de quartzo auríferos; processos de falhamento sísmico; Inclusões fluidas; Precipitação de ouro; Comportamento falha-válvula

ABSTRACT

The Serra do Cavalo Magro orogenic gold deposit is located in the southern Ribeira Belt, Brazil. Gold-quartz veins are hosted by Calymmian (1500-1450 Ma) metasedimentary and metabasic rocks and Ediacaran (610-600 Ma) granitic rocks. Petrological modeling indicates peak metamorphic conditions from 560 °C and 7 kbar (chlorite-biotite phyllite) to 625 °C and 6.8 kbar (garnet-biotite phyllite) recorded in immediate host rocks. Gold mineralization occurs in extensional and shear quartz veins structurally-controlled by NE-trending second-third order sinistral transcurrent shear zones. NNW-trending, vertical and subhorizontal extensional veins are oriented 55-85° in relation to the fault planes, indicating that the shear zones were severely misoriented for frictional reactivation. Deformation within the shear zones was accommodated by bulging recrystallization of quartz aggregates, while feldspar aggregates from granitic protoliths underwent cataclastic flow or were replaced by sericite-epidote producing phyllonites. Gold precipitated during stages of vein deformation within microfractures in mylonitized shear veins with quartz previously subjected to bulging recrystallization. Ore-fluids are recorded in coexisting CO_2-N_2, H_2O-NaCl-$CaCl_2$ and H_2O-CO_2-N_2-NaCl-$CaCl_2$ fluid inclusions of low to moderate salinities (1-18 wt.% NaCl eq.). Microthermometric data indicate entrapment conditions of 240-260 °C and 0.4-2.5 kbar, recording hydrostatic to supralithostatic fluid pressure conditions. High-temperature H_2O-NaCl-$CaCl_2$-KCl brine inclusions (up to 475 °C, 25-33 wt.% NaCl eq.) are considered unrelated with gold mineralization. Strong fluid pressure fluctuations from 0.4 to 1.6 kbar are associated with earthquake cycles and the fault-valve behavior. In this scenario, gold mineralization was associated with fluid immiscibility. There is evidence for restricted fluid mixing, but this process is interpreted as unrelated with gold mineralization. Available geochronological data and structural-petrological relationships with host rocks and shear zones indicate that mineralization was formed within 580-540 Ma in post-peak metamorphic episodes. The hydrothermal ore-fluids were likely produced by devolatilization reactions during prograde metamorphism at deeper levels. Subsequently, the metamorphic-hydrothermal fluids were channeled upwards within the strike-slip shear zones into rocks that have been metamorphosed and devolatilized at earlier times.

Keywords: Serra do Cavalo orogenic gold deposit; Au-quartz veins; Seismic faulting processes; Fluid inclusions; Gold precipitation; Fault-valve behavior

TABLE OF CONTENTS

LIST OF FIGURES

LIST OF TABLES

CHAPTER 1 INTRODUCTION

1.1 Theme Presentation

The southern Ribeira Belt is considered as an important metallogenetic province, which comprises major base metal and non-metallic deposits largely distributed in the Ribeira Valley (São Paulo and Paraná States). Since 1970s this region has been the target of several geochemical recognition projects with the purpose to find mineral resources (e.g., Addas and Vinha, 1975; Morgental et al., 1975, 1978; Silva et al., 1981; Pinto and Borin Junior, 1982; Chiodi Filho et al., 1983; Borin Junior and Ferrari, 1986; Drews and Vasconcelos, 1992). These works indicated relevant anomalies of Cu, Pb, and Zn ores that served as a guide to detecting areas to prospect gold and sulfides. Thus, the Piririca, Ivaporunduva, and Morro do Ouro auriferous deposits were found as well as other occurrences, including primarily the Serra do Cavalo Magro (e.g., Paiva and Morgental, 1980; Morgental et al., 1981; Paiva and Addas, 1982; Nogueira, 1990; Câmara, 1992; Lopes Jr. et al., 1994, 1995).

The first gold ore discovery at Serra do Cavalo Magro dates back 1930's, when pathfinders found it in alluviums of the Forquilha river and its tributaries. But it was between 1960's and 1970's that illegal miners extracted primary gold until the landowner company *Banespa S/A Mineração e Empreendimentos* demanded to the army suspension of all activities. Detailed studies emerged after Addas et al., (1985) perform geological mapping allied with geochemical and geophysical investigations, and estimated gold reserves of 8.000 tons with an average content of 20.0 g/ton. Nowadays, the Serra do Cavalo Magro region is part of the Intervales State Park (SP) and cannot be economically explored because was transformed into an environmental protection area that contains remnants of the Atlantic Forest biome.

As no further study has been conducted since 1980's, the current state of knowledge about the structural controls and Au-quartz veins genesis remains unclear. This dissertation was based on multi-technique approach that included field geology, petrography, microstructural, whole-rock geochemistry, mineral chemistry, metamorphic modelling, microthermometry and Raman spectroscopy of fluid inclusions. The achieved results aided to determine the structural controls, lithotypes, mineral assemblages, metamorphic P-T conditions, and fluid evolution during stages of quartz veins crystallization and gold mineralization. Furthermore, this research helped in the understanding of how the metamorphic devolatilization (e.g., Phillips and Powell, 2010), fault-valve activity (e.g., Sibson et al., 1988; Boullier and Robert, 1992; Cox, 1995, 1999; Robert et al., 1995; Henderson and McCaig, 1996; Nguyen et al., 1998; Sibson and Scott, 1998; Kolb et al., 2004; Faleiros et al., 2007, 2014), and hydrothermal fluid flow control the

Au-transport and precipitation mechanisms (e.g., Mikucki, 1998; Dugdale and Hagemann, 2001; Hagemann and Lüders, 2003; Faleiros et al., 2014; Garofalo et al., 2014; Klein, 2014; Wang et al., 2015; Yang et al., 2016, 2017) in orogenic gold deposits (e.g., Groves et al., 1998, 2003, Goldfarb et al., 2001, 2005; Goldfarb and Groves, 2015).

1.2 Location and Access

The project area (Fig. 1) is located at Serra do Cavalo Magro area, nearby the Saibadela and Guapiruvú neighborhoods, Sete Barras city (Brazilian State of São Paulo). The access from the São Paulo city to Sete Barras city was through of Régis Bittencourt (BR-116) and Nequinho Fogaça (SP-139) highways. From there, the route was facilitated by SP-139 highway until STB-344 and STB-436 secondary roads, which led to the Saibadela and Guapiruvú head offices, both of the Intervales State Park (SP).

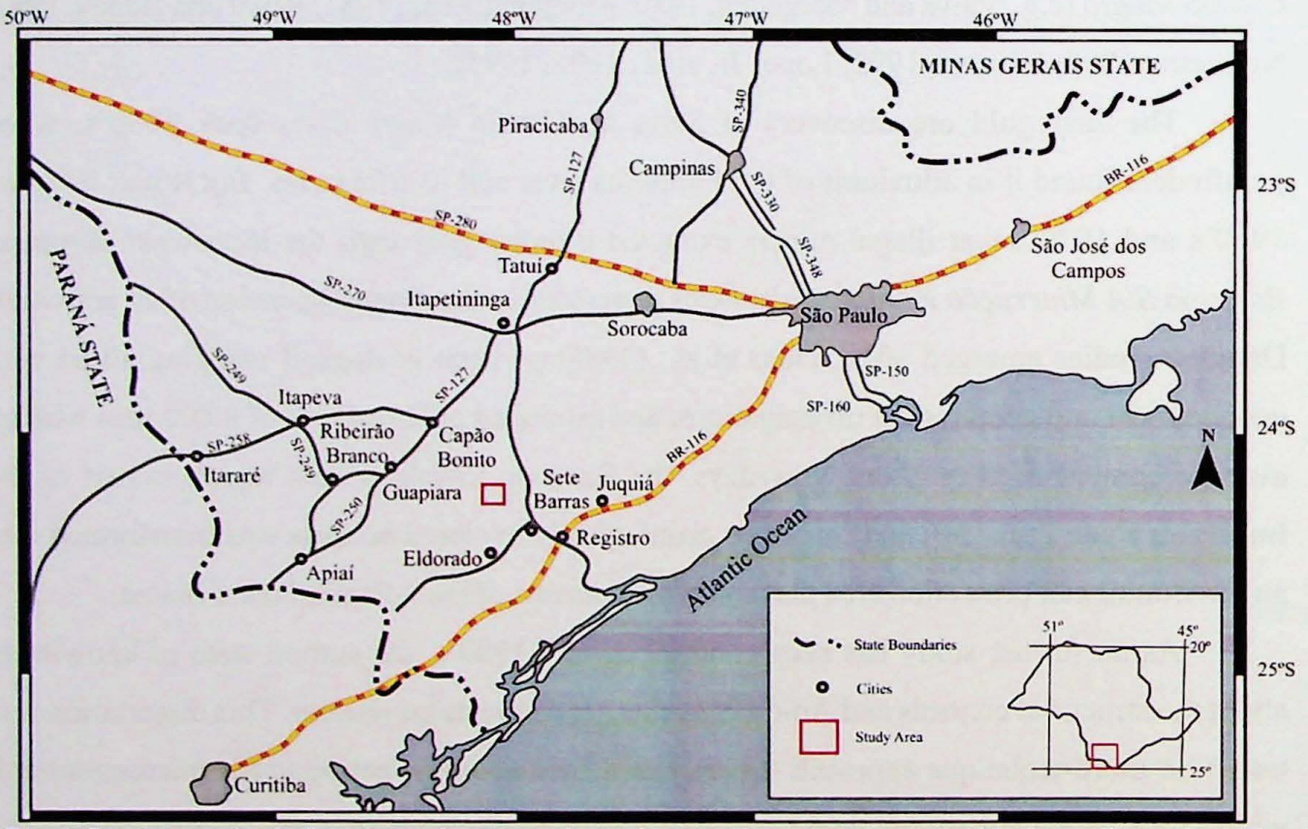

Fig. 1. Road map with the location and access to the study area. The map uses geographical coordinates in decimal degrees (WGS-84 datum).

1.3 Research Aims

The fundamental goal of this master's dissertation is based on determining the structural control and Au-quartz veins genesis at Serra do Cavalo Magro region to elaborate a descriptive-genetic model that can be used to discover similar deposits in the southern and central portions of the Ribeira Belt. Furthermore, this research should aid in the understanding of the geological, structural, and metamorphic evolution of an unexplored area at Apiaí Terrane, southern Ribeira

Belt, Brazil.

The second component of this project is divided into four specific aims, comprising to:

(1) Characterize the geometry, shape and orientation of Au-quartz veins on the macro- and microscopic scales and their relationships from local to regional structures;

(3) Infer the paleo-stress and kinematic regimes at moment of veins formation;

(3) Determine the compositions, temperatures, and pressures involved at the entrapment of ore-fluids during veins crystallization and/or deformation;

(4) Determine the metamorphic P-T conditions of host rocks.

1.4 Questions to Answer

This master's dissertation has six main issues, which motivated its accomplishment and served as a guideline to achieve the purpose objectives:

(1) Are the Au-quartz veins genetically linked to the larger structures such as folds, local and regional shear zones, or the Agudos Grandes Granite intrusion?

(2) The gold mineralization was formed during the veins crystallization or in a posterior episode of deformation and circulation of fluids?

(3) What is the P-T conditions and fluid composition of the Au-quartz veins?

(4) What is/are the mechanism(s) that control the Au-transporting and precipitation?

(5) What is/are the fluid sources involved during veining and gold mineralization?

(6) What is the metamorphic P-T peak conditions of host rocks?

CHAPTER 2 MATERIALS AND METHODS

2.1 Literature Review

The initial stage consisted of detailed literature review about the geological evolution of the southern Ribeira Belt, Apiaí Terrane, and especially of the Serra do Cavalo Magro deposit, based on regional and local studies acquired at the Institute of Geoscience (IGc) Library through the database search systems offer by SIBiUSP (Integrated System of Libraries of the University of São Paulo). In addition, a systematic research including orogenic gold deposits, metamorphic devolatilization, seismic faulting processes, Au-transporting and precipitation mechanisms, and the applied techniques such as scanning electron microscopy (SEM), whole-rock geochemistry (X-ray fluorescence), mineral chemistry (EMPA), metamorphic modelling, and fluid inclusion (microthermometry and laser Raman spectroscopy) was accomplished.

2.2 Geological Mapping

Geological mapping involved outcrops description (Fig. 2), systematic sampling of the Au-quartz veins and host rocks, as well as recognition of their spatial distribution, stratigraphic stacking, and contact relationships. The equipment utilized for data acquisition were: base map (1:20.000), field book, magnifying glass, bags, labels, geological hammer, compass (Clar-type), digital camera, and Global Position System (GPS).

2.3 Structural Analysis

The structural analysis involved standard procedures for the recognition and description of geometric and kinematic relationships among tectonic structures in the field, structural data collection with compass (foliations, lineations, folds and faults) and their hierarchization based on the superposition criteria (Turner and Weiss, 1963; Fleuty, 1964; Hobbs et al., 1976; Ramsay and Huber, 1983; McClay, 1987). The data obtained were statistically treated using the software Stereo 32 (version 1.0.3; Roller and Trepmann, 2011) for elaboration of stereoplots.

2.4 Petrographic and Microstructural Analysis

A total of 40 thin sections from the host rocks and Au-quartz veins were petrographically examined to identify the mineralogy, microstructures, and textural features (Blenkinsop, 2000; Passchier and Trouw, 2005; Bucher and Grapes, 2011). Photomicrographs were taken using an Olympus Camedia C-5050 camera coupled to an Olympus BXP-50 microscope, at Petrographic Microscopy Laboratory, Institute of Geoscience, University of São Paulo.

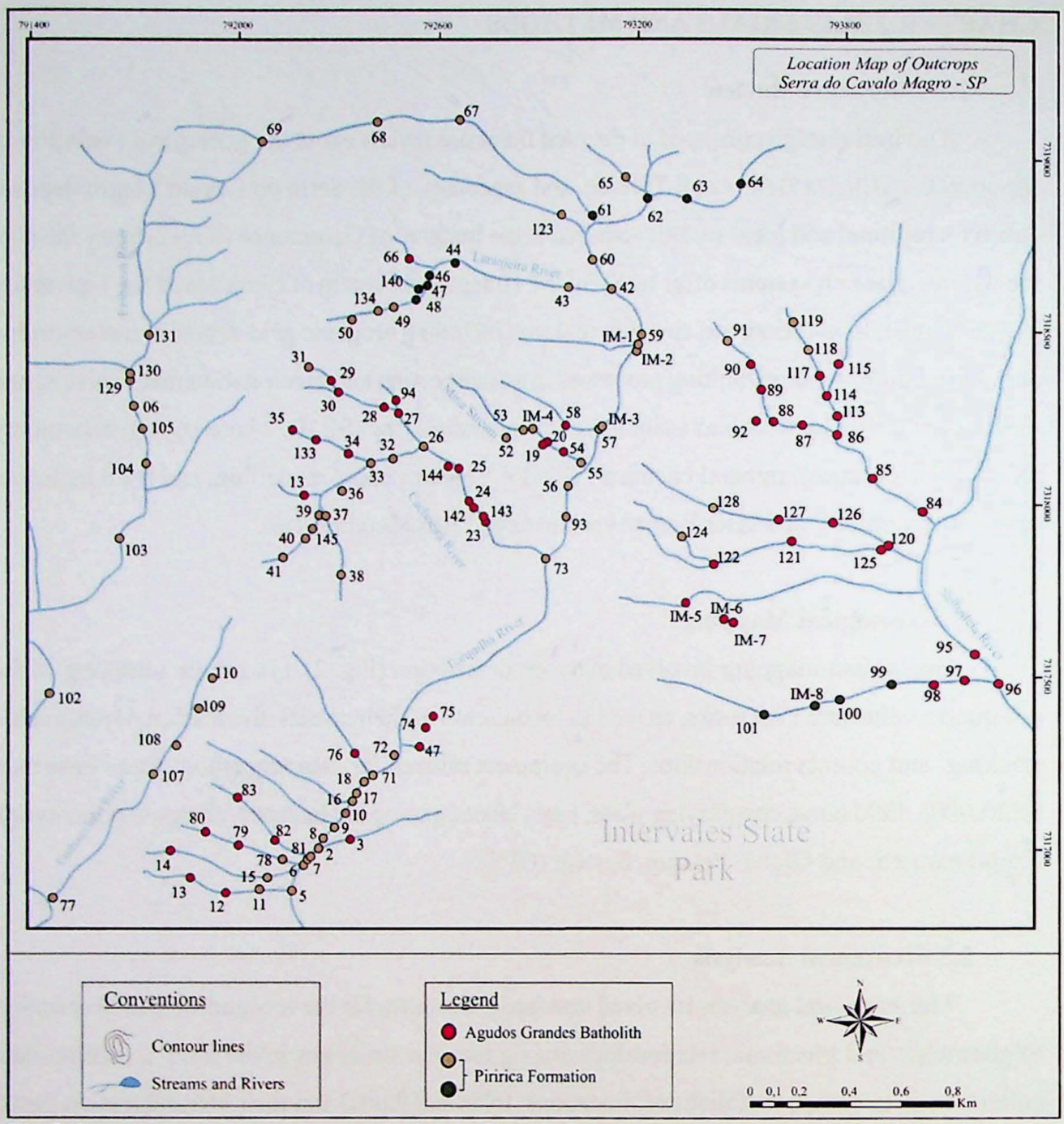

Fig. 2. Location map of outcrops recognized at the Serra do Cavalo Magro deposit integrated with available data from Addas et al. (1985). The map uses geographical coordinates in Universal Transverse Mercator (UTM) (WGS-84 datum).

2.5 Scanning Electron Microscopy

SEM analyses were performed on 8 polished thin sections (100 μm-thick) from the host rocks and Au-quartz veins to complement mineralogical and texture data as well identify all ore minerals. The equipment used was a FEI Quanta 600F scanning electron microscope under high vacuum conditions of 20 kV, 14 mm of working distance, and spot size of 5.8 μm. The analyses were carried out in the Technological Characterization Laboratory at the Department of Mining and Petroleum Engineering - Polytechnic School, University of São Paulo.

2.6 Fluid Inclusion Microthermometry

Microthermometric analyses were accomplished on 8 doubly-polished sections (100 μm thick) of the Au-quartz veins at Fluid Inclusion Laboratory, Institute of Geoscience, University of São Paulo, using a CHAIXMECA heating-freezing stage MTM-85. The stage was calibrated with the Merck MSP standard for high temperatures and Merck Signotherm standard for low-temperatures. The precision estimates were ± 0.1 °C for temperatures of CO_2 homogenization (T_hCO_2), and CO_2 melting (T_mCO_2), ± 0.2 °C for clathrate dissociation (T_dCl) and ice melting (T_mIce), ± 1 °C for eutectic melting of aqueous-carbonic and aqueous inclusions (T_E) and ± 2 °C for total homogenization (T_h). Physico-chemical properties of trapped fluids and isochores were calculated with the computer software packages FLUIDS and CLATHRATES (Bakker, 1997, 2003).

2.7 Raman Spectroscopy

Raman spectroscopy analyses were carried out in representative gaseous fluid inclusions at Structural Crystallography Facility, Physics Institute of São Carlos, University of São Paulo. The equipment used was a Raman Spectroscopy System Horiba LabRAM HR Evolution UV-VIS-NIR. Quantitative data were estimated considering the peak areas of gaseous components from the Raman spectra and the wavelength-dependent Raman scattering efficiencies for a laser beam of 532 nm (CO_2 v1: 1 (Garrabos et al., 1980), CO_2 2v2: 1.5 (Kerkhof and Olsen, 1990); N_2: 1 (Andersen et al., 1993), CH_4 v1: 7.5 (Kerkhof, 1987), following the procedures described in Burke (2001).

2.8 Whole-rock Geochemistry

Bulk chemical compositions of seven phyllite rock samples were carried out at the X-ray Fluorescence Laboratory, NAP-Geoanalítica Facility, University of São Paulo. Whole-rock samples were crushed using a hydraulic press and then powdered in an agate shatter box. Major element analyses were performed in fused pellet discs using an automatic AXIOS-MAX Advanced PANalytical X-Ray fluorescence spectrometer following the methods described by (Mori et al., 1999). Detection limits are 0.002 wt.% (MnO), 0.003 wt.% (TiO_2, P_2O_5), 0.01 wt.% (Fe_2O_3, MgO, CaO, K_2O, loss on ignition - LoI), 0.02 wt.% (Al_2O3, Na_2O), and 0.03 wt.% (SiO_2).

2.9 Mineral Chemistry

Major element concentrations (SiO_2, TiO_2, Cr_2O_3, Al_2O_3, FeO, MnO, MgO, CaO, Na_2O,

and K_2O) of garnet, muscovite, biotite, chlorite, and felsdpar from 2 representative phyllite rock samples (IM-1b and IM-4b), as well as garnet X-ray compositional elemental maps (Fe, Ca, Mn, and Mg) were acquired, using a JXA-8530 HyperProbe Electron Probe Microanalyzer (EMPA), at the Electron Microprobe Laboratory, NAP-Geoanalítica Facility, University of São Paulo. Operating conditions were 15 kv accelerating voltage, 20 nA beam current, and spot size of 5 μm diameter. Data processing was based on the calculation of mineral structural formulas using Microsoft Excel 2016 spreadsheets.

2.10 Metamorphic Modelling

P-T isochemical phase diagrams were constructed for rock compositions representative of garnet-absent (sample IM-1b) and garnet-bearing (sample IM-4b) phyllites, using the Perple_X software (Connolly, 2005), version 6.7.5, and the internally consistent thermodynamic database of Holland and Powell (2011). Samples were modeled in the MnO-Na_2O-CaO-K_2O-FeO-MgO-Al_2O_3-SiO_2-H_2O-TiO_2-Fe_2O_3 (MnNCKFMASHTO) system. The solution models for chlorite, chloritoid, muscovite, biotite, garnet, staurolite, and ilmenite are from White et al. (2014), while epidote is from Holland and Powell (2011) and feldspar is from Fuhrman and Lindsley (1988). Quartz, titanite, and rutile are considered as pure phases, while H_2O is considered as saturated phase component. The Fe_2O_3 content was adjusted for each single bulk rock composition to reproduce the minor Fe-Ti-oxide phases observed in thin sections.

CHAPTER 3 TECTONIC SETTING

3.1 Ribeira Belt

The Ribeira Belt is a NE-trending collisional orogen parallel to the coastline of SE Brazil which forms a central branch of the Mantiqueira Orogenic System (Fig. 3; e.g., Almeida et al., 1981; Brito Neves et al., 1999; Heilbron et al., 2004, 2017). The framework of this orogen was controlled by crustal-scale transcurrent fault systems related to an oblique collision between the São Francisco, Paranapanema, Luís Alves, and Congo cratons during the Neoproterozoic (e.g., Campanha and Sadowski, 1999; Campanha and Brito Neves, 2004; Faleiros et al., 2010, 2011a, 2016). As result, the Ribeira Belt displays a complex evolution history involving reworking of distinct tectonic blocks, which includes allochthonous Archaean to Paleoproterozoic basement rocks, Mesoproterozoic and Neoproterozoic volcanosedimentary successions, besides I-, S-, and hybrid-type granites that intruded basement and supracrustal rocks (e.g., Faleiros, 2008, Faleiros et al., 2010, 2011a, 2016).

The southern Ribeira Belt is divided into fault-bounded composite terranes called Apiaí, Curitiba, Luís Alves, and Paranaguá, whose contrasting geological evolution is represented by distinct rocks, structures, ages, geochemical and isotopic signatures, and metamorphic histories (e.g., Faleiros, 2008; Faleiros et al., 2010, 2011a, b, 2012, 2016; Faleiros and Pavan, 2013). Available U-Pb geochronological data (e.g., Hackspacher et al., 2000; Weber et al., 2004; Campanha et al., 2008, 2015, Siga Jr. et al., 2009, 2011) revealed that the Apiaí terrane records a juxtaposition of three main tectonic events with ages ranged from Calymmian (1500-1400 Ma), to Setnian to Tonian (1200-880 Ma), and Ediacaran (630-580 Ma).

The Serra do Cavalo Magro deposit is located at the Apiaí terrane. This domain is mostly characterized by supracrustal rocks from the Açungui supergroup (Campanha, 1991; Campanha and Sadowski, 1999), which includes the Votuverava, Lajedo and Itaiacoca groups, Água Clara and Iporanga formations, and Serra das Andorinhas sequence (Faleiros et al., 2012). Metapelitic and amphibolitic rocks from the Votuverava group underwent a Neoproterozoic (630-620 Ma) Barrovian-type clockwise P-T-t loop metamorphism with conditions ranging from greenschist to amphibolite facies (Faleiros, 2003, 2008; Faleiros et al., 2010). Paleoproterozoic basement rocks occurs in the cores of broad antiforms (Betara and Tigre units), being primarily composed of mylonitic syenogranites with geochemical affinities of A-type granites and zircon U-Pb ages of 1748-1772 Ma (Cury et al., 2002). Furthermore, this terrane was intruded by Neoproterozoic granitic plutons (650-580 Ma) formed in accretionary, collisional and post-collisional tectonic events (e.g., Janasi et al., 2001; Prazeres Filho, 2005; Silva et al., 2005).

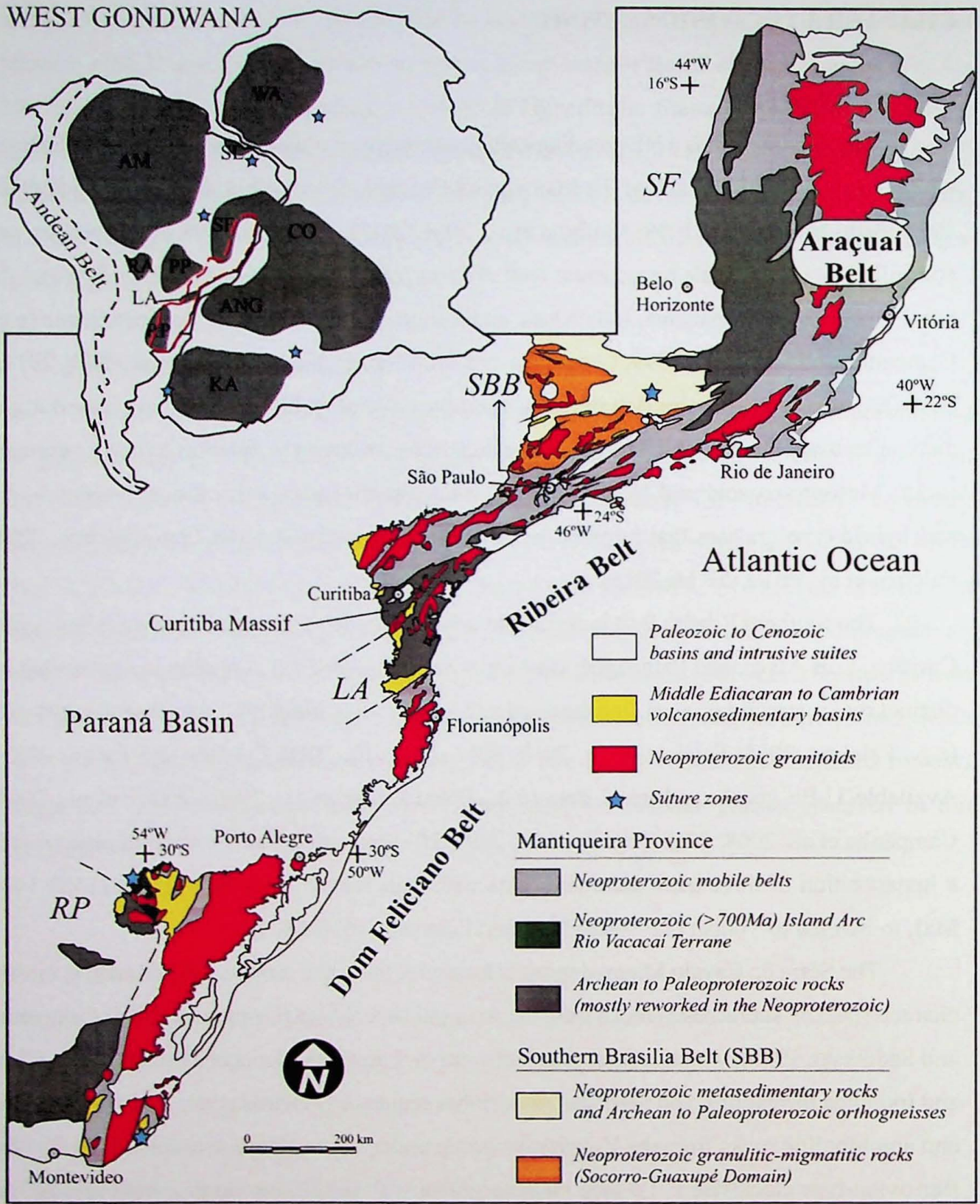

Fig. 3. Tectonic map and main geological units of the Mantiqueira Province: The inset shows the cratonic blocks of Western Gondwana. Abbreviations: AM, Amazonian Craton; ANG, Angola Block; CO, Congo Craton, KA, Kalahari Craton; KA, Kalahari Craton; LA, Luis Alves Craton; PP, Paranapanema Block; RA, Rio Apa Block; RP, Rio de La Plata Craton; SL, São Luis Craton; WA, West Africa Craton. Modified from Meira et al., (2015).

3.2 Votuverava Group

The Votuverava group was divided into five formal lithostratigraphic formations: Perau, Rubuquara, Nhunguara, Piririca, and Ribeirão das Pedras Formations, as well as others informal

and undivided units (Faleiros et al., 2010, 2012; Faleiros and Pavan, 2013; Campanha et al., 2015). This group is mainly formed by metamorphosed pelitic successions, whose depositional environment was interpreted as distal turbidites (Campanha et al., 2015). There are also, a large number of metabasic and metavolcanic rocks, which occurs associated with quartzites, marbles, calc-silicate rocks, metaconglomerates, metacherts, iron formations, and Pb-Zn-Ag-Cu sulfides deposits (Campanha, 1991).

These rocks showed a Barrovian-type metamorphism ranging from lower greenschist to middle amphibolite facies (Faleiros, 2003, 2008; Faleiros et al. 2010). Mineral assemblages and geothermobarometric data from metapelites and metabasites (chlorite to garnet zones) indicates metamorphic conditions of 380-630 °C and 6-8 kbar, and clockwise P-T-t paths (Faleiros et al., 2010). Available geochemical data from metabasic rocks revealed signatures of back-arc basin basalts - BABB (Faleiros et al., 2011b; Campanha et al., 2015) and U-Pb zircon data provided ages of 1475-1490 Ma, which was interpreted as the depositional event (e.g., Campanha et al., 2015).

3.2.1 Piririca formation

The Piririca Formation was originally defined by Perrotta (1996) as a volcanosedimentary sequence mostly formed of carbonaceous and carbonatic phyllites, sericite-quartz phyllites, and marbles metamorphosed under lower greenschist facies conditions (chlorite zone). These rocks occur intercalated with long lenses of metabasic to meta-ultrabasic lithotypes, which commonly show carbonation and chloritization hydrothermal alterations. Metabasic rocks are divided into two distinct sets with tholeiitic magmatic affinities (Nogueira, 1990), where the type-1 comprises FeO and TiO_2-rich rocks and the type-2 includes CaO and MgO-rich rocks. According to Perrotta (1996), the SiO_2 and MgO average contents are compatible with basanites of alkaline tendency generated in an insular volcanic arc. In addition, this unit is well-known for hosting orogenetic gold deposits related to the veins (Perrotta, 1996). Nogueira (1990) obtained Pb-Pb model ages of 1270 and 1303 Ma for galena crystals that occur in gold-bearing quartz veins, whereas fluid inclusion data showed low-salinity aqueous (4 wt% NaCl eq.) and CO_2-bearing (>25 mol % CO_2) ore-fluids with depositional temperatures ranging from 200 to 400°C.

3.3 Agudos Grandes Batholith

The Agudos Grandes Batholith represents one of the most voluminous magmatic events of the Ribeira Belt, extending more than 200 km among the Embu and Apiaí terranes (Janasi et

al., 2001). Available zircon and monazite U-Pb data indicate ages of 610-615 Ma, 600-605 Ma and 565-585 Ma for accretionary, collisional, and post-collisional tectonic events, respectively, (eg., Janasi et al., 2001; Martins, 2001; Leite, 2003).

Syn-orogenic rocks correspond primarily to the Ibiúna, Tapiraí and Turvo granite-types. The Ibiúna granite is constituted by isotropic to slightly foliated, porphyritic, hornblende-biotite monzogranites with pink K-feldspar up to 4 cm-large set in the matrix (e.g., Janasi et al., 2001; Martins, 2001), whereas the Tapiraí granite is characterized by foliated, titanite-allanite-bearing monzogranites (Leite, 2003). Both types consist of intermediate to felsic, and metaluminous high-K calc-alkaline granites formed by multiple non-consanguineous magmatic pulses with variable oxygen fugacity (fO_2) at pressures between 3-5 kbar (Martins, 2001). The Turvo body is characterized by fractionated leucogranites with peraluminous geochemical character, in which reveal its crustal origin (Janasi et al., 2001).

Late- and post-orogenic lithotypes correspond the Piedade and Serra da Bateia granites, respectively. The Piedade type comprises an elliptical intrusion essentially composed of slightly foliated, porphyritic granodiorites to monzogranites, displaying metaluminous to peraluminous geochemical affinities (Leite, 1997; Martins, 2001; Leite et al., 2006). The Serra da Bateia type is an elongated body intrusive in the SW border of the Piedade granite, which suggest its youngest crustal emplacement (Janasi et al., 2001; Leite, 2003). The dominant lithotype is a porphyritic syenogranite rich in K-feldspar megacrystals oriented along a magmatic-flux foliation (Janasi et al., 2001). This unit shows A-type granites geochemical affinities evidenced by lower mg#, high contents of Zr, Nb, and Y, and low contents of Ca, Sr, and Ba (Janasi et al., 1994).

CHAPTER 4 P-T-FLUID-DEFORMATION REGIME OF THE SERRA DO CAVALO MAGRO OROGENIC GOLD DEPOSIT, SOUTHERN RIBEIRA BELT, BRAZIL

Isaac S. Malta [a, *], Frederico M. Faleiros [a], Lena V. S. Monteiro [a], Marcelo B. de Andrade [b], Bruna Coldebella [a], Melina C. B. Esteves [a]

[a] Departamento de Mineralogia e Geotectônica, Instituto de Geociências, Universidade de São Paulo, Rua do Lago, 562; CEP: 05508-080, São Paulo, SP, Brazil.

[b] Departamento de Física e Ciência Interdisciplinar, Instituto de Física de São Carlos, Universidade de São Paulo, Av. Trabalhador São-Carlense, 400; CEP: 13566-590, São Carlos, SP, Brazil.

[*] E-mail Address: isaacmalta@usp.br (I.S. Malta)

Abstract

The Serra do Cavalo Magro orogenic gold deposit is located in the southern Ribeira Belt, Brazil. Gold-quartz veins are hosted by Calymmian (1500-1450 Ma) metasedimentary and metabasic rocks and Ediacaran (610-600 Ma) granitic rocks. Petrological modeling indicates peak metamorphic conditions from 560 °C and 7 kbar (chlorite-biotite phyllite) to 625 °C and 6.8 kbar (garnet-biotite phyllite) recorded in immediate host rocks. Gold mineralization occurs in extensional and shear quartz veins structurally-controlled by NE-trending second-third order sinistral transcurrent shear zones. NNW-trending, vertical and subhorizontal extensional veins are oriented 55-85° in relation to the fault planes, indicating that the shear zones were severely misoriented for frictional reactivation. Deformation within the shear zones was accommodated by bulging recrystallization of quartz aggregates, while feldspar aggregates from granitic protoliths underwent cataclastic flow or were replaced by sericite-epidote producing phyllonites. Gold precipitated during stages of vein deformation within microfractures in mylonitized shear veins with quartz previously subjected to bulging recrystallization. Ore-fluids are recorded in coexisting CO_2-N_2, H_2O-NaCl-$CaCl_2$ and H_2O-CO_2-N_2-NaCl-$CaCl_2$ fluid inclusions of low to moderate salinities (1-18 wt.% NaCl eq.). Microthermometric data indicate entrapment conditions of 240-260 °C and 0.4-2.5 kbar, recording hydrostatic to supralithostatic fluid pressure conditions. High-temperature H_2O-NaCl-$CaCl_2$-KCl brine inclusions (up to 475 °C, 25-33 wt.% NaCl eq.) are considered unrelated with gold mineralization. Strong fluid pressure fluctuations from 0.4 to 1.6 kbar are associated with earthquake cycles and the fault-valve behavior. In this scenario, gold mineralization was associated with fluid immiscibility. There is evidence for restricted fluid mixing, but this process is interpreted as unrelated with gold mineralization. Available geochronological data and structural-petrological relationships with host rocks and shear zones indicate that mineralization was formed within 580-540 Ma in post-peak metamorphic episodes. The hydrothermal ore-fluids were likely produced by devolatilization reactions during prograde metamorphism at deeper levels. Subsequently, the metamorphic-hydrothermal fluids were channeled upwards within the strike-slip shear zones into rocks that have been metamorphosed and devolatilized at earlier times.

Keywords: Serra do Cavalo orogenic gold deposit; Au-quartz veins; Seismic faulting processes; Fluid inclusions; Gold precipitation; Fault-valve behavior

4.1 Introduction

The term "orogenic gold deposits" was firstly introduced by Groves et al. (1998) in an attempt to unify a model for hydrothermal gold-bearing quartz vein-type deposits in metamorphic terranes, formed in compressional settings related with accretionary and collisional orogens (e.g., Groves et al., 1998, 2000, 2003; Bierlein et al., 2004; Goldfarb et al., 2005; Goldfarb and Groves, 2015; Groves and Santosh, 2016). Orogenic gold deposits are formed from Archean to Phanerozoic, mostly within time periods closely correlated with major crustal growth and the supercontinent cycle (Goldfarb et al., 2001; Cawood and Hawkesworth, 2015). These deposits display strong structural controls, being formed over depths from 3-5 to 15-20 km along second- and third-order subsidiary shear zones associated with transcrustal shear zone systems that acted as large conduits for regional fluid flow (e.g., Cox et al., 1987; Boullier and Robert, 1992; Robert et al., 1995; Nguyen et al., 1998; Cox, 1999; Groves et al., 2000; Parnell et al., 2000; Kolb et al., 2004; Yang et al., 2017). Besides most orogenic gold deposits share many common features, as the strong structural controls, association with minor shear zones, similar hydrothermal alteration patterns and similar ore-forming fluids (primarily low-to-moderate salinity H_2O-$CO_2 \pm CH_4 \pm N_2 \pm H_2S$ fluids) (Groves et al., 1998; Tomkins, 2013), some issues remain contentious, including the sources for mineralizing fluids and gold, the relationships between ore genesis and peak metamorphism, and the role of immediate host rocks and of contemporaneous igneous activities. The formation of most shear zones that host orogenic gold deposits involved cyclic fluctuations in tectonic stress and fluid pressure values correlated with earthquake cycles, the called fault-valve behavior (e.g., Sibson et al., 1988; Boullier and Robert, 1992; Cox, 1995, 1999; Robert et al., 1995; Nguyen et al., 1998; Sibson and Scott, 1998; Dugdale and Hagemann, 2001; Kolb et al., 2004; Faleiros et al., 2014). If on the one hand the fault-valve behavior allows the mineralizing fluids rapidly traverse large thicknesses of the crust, from the presumably deeper sources to the sites of gold deposition (Tomkins, 2013), on the other hand, it is inherently expected that fluids from many different sources, including metamorphic, magmatic and meteoric sources, should be near instantaneously pumped to the opened shear zones during earthquake rupture events and then mixed (Sibson et al., 1975, 1988). This behavior is clearly demonstrated in regionally distributed, non-mineralized fault-valve-related vein systems (e.g., Faleiros et al., 2007). This behavior can also be the major responsible for discrepant proposed models for orogenic gold deposits, including (1) metamorphic devolatilization of sedimentary piles and volcanic rocks (e.g., Phillips and Groves, 1983; Goldfarb et al., 1988; Cox et al., 1991; McCuaig and Kerrich, 1998; Pettke et al., 1999, 2000, Pitcairn et al., 2006, 2014; Tomkins, 2010; Phillips and Powell, 2010; Yardley and Cleverley, 2013; Fusswinkel et al., 2017); (2) release of magmatic-

hydrothermal fluids from granitic intrusions (e.g., Burrows et al., 1986; Neumayr et al., 2008; Bath et al., 2013; Lawrence et al., 2013a, b; Treloar et al., 2014); (3) deep-seated circulation of meteoric water (e.g., Hagemann et al., 1994); (4) mantle-derived fluids (e.g., Cameron, 1988; Graupner et al., 2006; Mao et al., 2015; Tan et al., 2017); (5) fluids expelled from devolatilization of subducting oceanic slabs (e.g., Goldfarb and Santosh, 2014; Goldfarb and Groves, 2015; Li et al., 2018); (6) mixture of magmatic and metamorphic fluids (e.g., Rogers et al., 2013; Shen et al., 2016; Mishra et al., 2018; Sahoo et al., 2018; Augustin and Gaboury, 2019; Liu et al., 2019), and (7) mixing between metamorphic fluids and meteoric water (e.g., Gao et al., 2018).

The Serra do Cavalo Magro gold deposit (Lat. 24°13'16.39" S; Long. 48°06'59.19" W) is located in the southern portion of the Ribeira Belt (Figs. 4 and 5a), Brazil, which is an accretionary-to-collision orogen related with Gondwana assembly primarily during the Ediacaran (Brito Neves et al., 1999; Heilbron et al., 2004; Faleiros et al., 2011a). Gold was firstly discovered at Serra do Cavalo Magro in 1930s, when pathfinders found it in alluviums of the Forquilha River and its tributaries. However, it was between 1960s and 1970s that illegal miners extracted primary gold until the landowner company Banespa SA Mineração e Empreendimentos requested to the army suspension of all activities. Detailed geological mapping supported by geochemical and geophysical investigations were performed by the Geological Survey of Brazil (CPRM), who estimated Au reserves of 8,000 tons with an average content of 20.0 g/ton (Addas et al., 1985). Addas et al. (1985) demonstrated that gold-bearing quartz veins are hosted by metasedimentary, metabasite, granitic and fault-related rocks, but the possible role of faulting processes, igneous activity and fluid-rock interaction on the gold mineralization were not investigated until now.

In this paper, we used a multi-technique approach, including field geology, petrographic and microstructural characterization of ore and host rock samples, detailed microthermometric and Raman spectroscopy analysis of fluid inclusions from mineralized veins and metamorphic modeling and geothermobarometry of host rocks from the Serra do Cavalo Magro gold deposit. The results are used to: (a) stablish the structural controls of Au-quartz veins, (b) investigate their relationships with local and regional shear zones and the involved fault-related process, (c) characterize the P-T-X fluid evolution and its relationships with the regional metamorphic P-T path and deformation phases. The achieved results from this paper contribute to elucidate how faulting processes and related fluid flow, felsic magmatic activity, fluid-rock interaction and regional metamorphism could be related with orogenic gold mineralization.

4.2 Geological Setting

The Ribeira Belt (Fig. 4) is a NE-trending collisional orogen subparallel to the coastline of SE Brazil that forms the central branch of the Mantiqueira Orogenic System (e.g., Almeida et al., 1977, 1981; Brito Neves et al., 1999). The architecture of this orogen was controlled by a crustal-scale transcurrent shear zone system (Fig. 4) related to an oblique collision between the São Francisco, Paranapanema, Luís Alves, and Congo cratons during the Neoproterozoic (e.g., Campanha and Brito Neves, 2004; Faleiros et al., 2010, 2011a, 2016; Ribeiro et al., 2019). As result, the Ribeira Belt displays a complex evolution history involving reworking of distinct tectonic blocks, which includes allochthonous Archaean to Paleoproterozoic basement rocks, Mesoproterozoic and Neoproterozoic volcanosedimentary units, besides I-, S-, and hybrid-type granites that intruded both basement and supracrustal rocks (e.g., Heilbron et al., 2004; Faleiros et al., 2011a, 2016; Campanha et al., 2019).

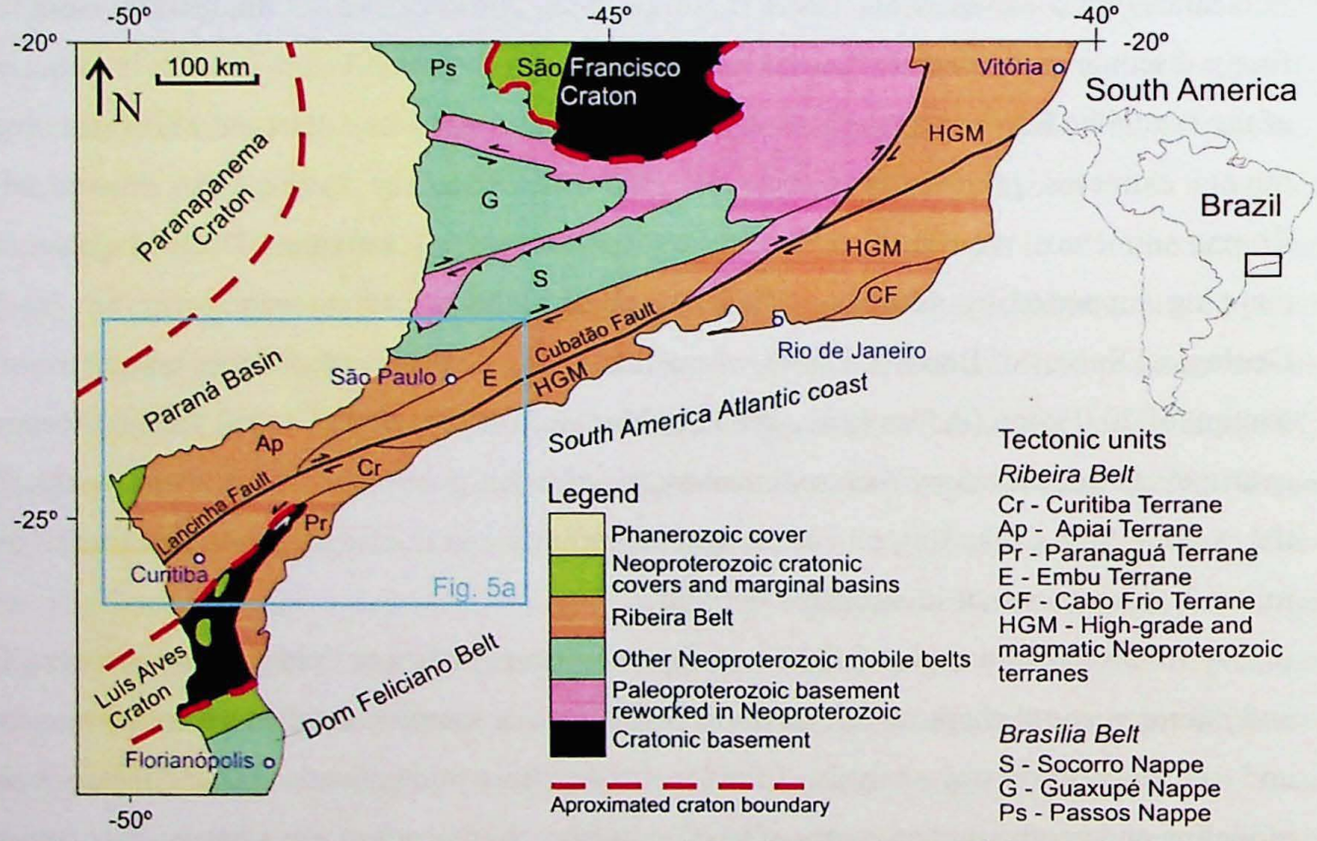

Fig. 4. Regional geological context of southeastern and south Brazil (adapted from Faleiros et al., 2016). The map uses geographical coordinates in degrees (WGS-84 datum).

The southern Ribeira Belt is divided into fault-bounded composite terranes called Apiaí, Curitiba, Luís Alves, and Paranaguá Terranes (Fig. 5a), in which contrasting geological evolution is represented by distinct rock associations, structures, ages, geochemical and isotopic signatures, and metamorphic histories (e.g., Faleiros et al., 2011, 2016). The Apiaí Terrane (Fig. 5a, b) is considered as an important metallogenetic province, which comprises major base metal

and non-metallic deposits largely distributed in the Ribeira Valley (Brazilian States of São Paulo and Paraná). Since 1970s this region has been the target of several geochemical recognition projects with the purpose to find mineral resources (e.g., Addas and Vinha, 1975; Morgental et al., 1975, 1978; Pinto and Borin Junior, 1982; Borin Junior and Ferrari, 1986; Drews and Vasconcelos, 1992). These works indicated relevant anomalies of Cu, Pb, and Zn that served as a guide to detecting areas to prospect gold and sulfides. Thus, the Piririca, Ivaporunduva, Serra do Cavalo Magro and Mina Morro do Ouro auriferous deposits (Fig. 5a) were found (Paiva and Morgental, 1980; Nogueira, 1990; Câmara, 1992; Lopes Jr et al., 1994, 1995; Perrotta and Campos Neto, 1999).

The Apiaí Terrane is comprised by the juxtaposition of different supracrustal rock units, including the Água Clara Formation (1500-1470 Ma; zircon U-Pb data from Weber et al., 2004), Votuverava Group (1490-1475 Ma; zircon U-Pb data from Siga Jr. et al., 2011; Campanha et al., 2015), Lajedo Group (1200-880 Ma; zircon U-Pb data from Campanha et al., 2016), Itaiacoca Group (1000-900 Ma and 640-630 Ma subunits; zircon U-Pb data from Siga Jr. et al., 2009), and Iporanga Formation (590-580 Ma; zircon U-Pb data from Campanha et al., 2008). Paleoproterozoic basement rocks occur in the cores of broad antiforms, being primarily composed of mylonitic syenogranites with geochemical affinities of A-type granites and zircon U-Pb ages between 1748 and 1772 Ma (Cury et al., 2002). Furthermore, this terrane was intruded by Neoproterozoic (ca. 650-580 Ma) granitic plutons formed in accretionary, collisional and post-collisional episodes (e.g., Janasi et al., 2001; Prazeres Filho, 2005).

The gold deposits from the Apiaí Terrane are primarily hosted by rocks considered as fertile to gold mineralization, as metavolcano-sedimentary rocks and iron formations with syngenetic gold mineralizations from the Água Clara Formation (Mina Morro do Ouro deposit; Faleiros et al., 2014), metabasic rocks from the Votuverava Group (Piririca and Ivaporunduva deposits; Nogueira, 1990) and Ediacaran granitic rocks (Passa Três deposit; Picanço, 2000; Dressel et al., 2018); and Serra do Cavalo Magro deposit; this work) (Fig. 5a). This raised the interpretation that some orogenic gold mineralizations at the Apiaí Terrane were influenced by fluid interaction with immediate host rocks (Nogueira, 1990; Faleiros et al., 2014), while the Passa Três deposit was recently reinterpreted as an intrusion-related deposit (Dressel et al., 2018). Geochemical and isotope data suggest that the metasedimentary and metabasic rocks from the Água Clara Formation and Votuverava Group were formed in ca. 1500-1450 Ma Calymmian back-arc basin environments (Maniesi, 1997; Weber et al., 2004; Campanha et al., 2015). On the other hand, available geochronological data and field geological relationships indicate that the orogenic gold deposits were formed during the Ediacaran (Brasiliano-Pan

African tectonic event) (Faleiros et al., 2014).

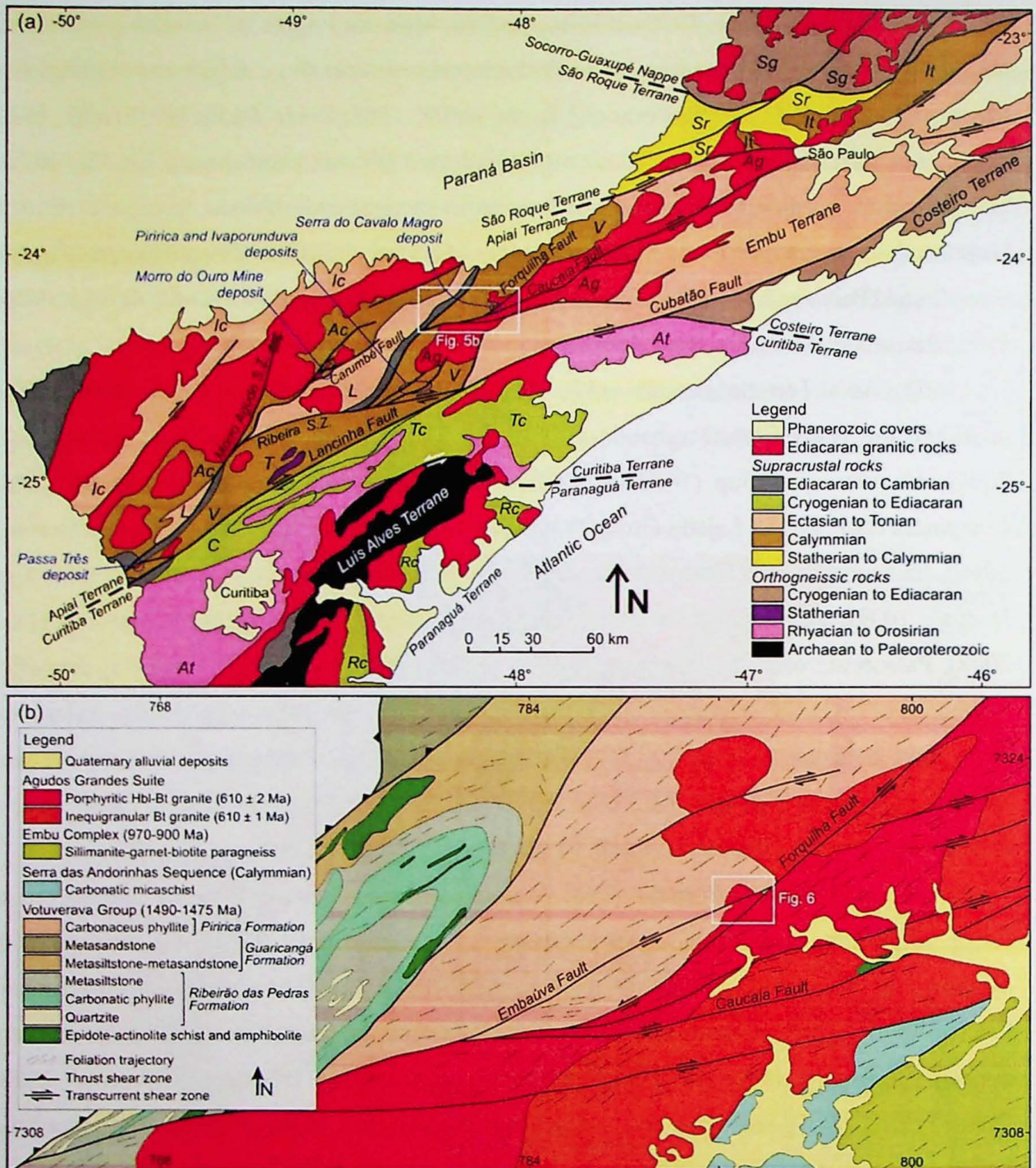

Fig. 5. Simplified geological map of the southern and central portions of the Ribeira Belt with the location of Fig. 5b. Geological units: Itaiacoca Group (Ic), Água Clara Formation (Ac), Lajeado Group (L), Votuverava Group (V), Betara Formation (B), São Roque Group (Sr), Serra do Itaberaba Group (It), Socorro-Guaxupé Nappe (Sg), Tigre Gneiss (T), Capiru Formation (C), Turvo-Cajati Formation (Tc), Rio das Cobras Formation (Rc), Atuba Complex (At). Modified after Campanha et al. (2015).

4.3 Analytical Methods

Scanning electron microscope analyses were performed on 8 polished thin sections (100 µm-thick) from the host rocks and Au-quartz veins to complement mineralogical and texture data and identify ore minerals. The equipment used was a FEI Quanta 600F scanning electron

microscope under high vacuum conditions of 20.0 kV, 14.0 mm of working distance, and spot of 5.8 μm diameter.

Bulk chemical compositions of 2 representative phyllite host rock samples (IM-1b and IM-4b) were performed at the X-Ray Fluorescence Laboratory, NAP-Geoanalítica Facility, University of São Paulo, Brazil. Whole-rock samples were crushed using a hydraulic press and then powdered in an agate shatter box. Major element analyses were carried out in fused pellet discs using an automatic AXIOS-MAX Advanced PANalytical X-Ray fluorescence spectrometer following the methods described by Mori et al. (1999). Detection limits are 0.002 wt.% (MnO), 0.003 wt.% (TiO_2, P_2O_5), 0.01 wt.% (Fe_2O_3, MgO, CaO, K_2O, loss on ignition), 0.02 wt.% (Al_2O_3, Na_2O), and 0.03 wt.% (SiO_2).

Major element concentrations of garnet, muscovite, biotite, chlorite, and felsdpar from samples IM-1b and IM-4b were acquired using a JXA-8530 HyperProbe Electron Probe Microanalyzer (EMPA), at Electron Microprobe Laboratory, NAP-Geoanalítica Facility. The analytical parameters were: 15.0 kv voltage, 20.0 nA beam current, and spot of 5.0 μm diameter.

Microthermometric fluid inclusion data were taken on 8 doubly-polished thin sections (100 μm-thick) of the Au-quartz veins, using a CHAIXMECA heating-freezing stage MTM-85, which has been calibrated with the Merck MSP standard for high temperatures and Merck Signotherm standard for low-temperatures. The accuracy estimates of microthermometric analyses were ± 0.1 °C for temperatures of CO_2 homogenization (T_hCO_2), and CO_2 melting (T_mCO_2), ± 0.2 °C for clathrate dissociation (T_dCl) and ice melting (T_mIce), ± 1 °C for eutectic melting of aqueous-carbonic and aqueous inclusions (T_E) and ± 2 °C for total homogenization (T_h). Data processing was carried out using the software packages FLUIDS (Bakker, 1997) and CLATHRATES (Bakker, 2003), applying state equations for determining the composition and density of CO_2-rich inclusions and carbonic phases of H_2O-CO_2 inclusions (Duschek et al., 1990; Span and Wagner, 1996); density and salinity of aqueous phases, as well as bulk properties of H_2O-CO_2 inclusions (Duan et al., 1992a, b); bulk properties and densities (Zhang and Frantz, 1987) and the volumetric proportions of aqueous fluid inclusions (Archer, 1992).

Raman spectroscopy analyses were carried out in representative gaseous fluid inclusions at the Structural Crystallography Laboratory, Physics Institute of São Carlos, University of São Paulo (Brazil), using a Raman Spectroscopy System Horiba LabRAM HR Evolution UV-VIS-NIR. Quantitative data were estimated considering the peak areas of gaseous components from Raman spectra and the wavelength-dependent Raman scattering efficiencies for a laser beam of 532 nm (CO_2 v1: 1 (Garrabos et al., 1980), CO_2 2v2: 1.5 (Kerkhof and Olsen, 1990); N_2: 1.0 (Andersen et al., 1993), CH_4 v1: 7.5 (Kerkhof, 1987), following the procedure described in

Burke (2001).

4.4 Serra do Cavalo Magro Deposit (SCMD)

4.4.1 Host rocks

The gold mineralization of the SCMD occurs in quartz veins hosted in metasedimentary and metabasite rocks from the Piririca Formation (Votuverava Group; Faleiros et al., 2012) and granitic rocks from the Agudos Grandes Suite (Janasi et al., 2001) (Figs. 5 and 6).

The Piririca Formation at the deposit district is primarily composed of phyllites with minor lenses of amphibolite (Fig. 6), and centimeter- to meter-thick layers of calc-silicate rocks and tourmalinites. The metasedimentary rocks show a main schistosity (S_1) parallel to a millimeter- to centimeter-thick compositional layering (Fig. 7a-f) with subvertical NE-trending orientation (Fig. 6). The phyllite rocks present two main mineral assemblages along the S_1 schistosity: biotite-chlorite-muscovite-albite-oligoclase-quartz-hematite (Fig. 7a) and garnet-biotite-muscovite-hematite/ilmenite-magnetite (Fig. 7b). Tourmaline, monazite and zircon are the main accessory phases present in both lithotypes. Calc-silicate layers are formed by quartz, K-feldspar, garnet, muscovite, epidote, carbonate, and hornblende (Fig. 7c). Amphibolite bodies are primarily composed of hornblende, plagioclase, titanite and ilmenite and show a nematoblastic texture defining the S_1 schistosity (Fig. 7d). Tourmalinite bodies present a lamination parallel to the S_1 schistosity, with alternating tourmaline-rich and quartz-rich layers (Fig. 7e, f). The metamorphic assemblages of all lithotypes are compatible with medium greenschist to lower amphibolite facies metamorphic conditions.

The Agudos Grandes Suite at the deposit district is composed of a pinkish-grey, porphyritic monzogranite with centimetric K-feldspar phenocrysts (up to 4 cm) (Fig. 8a) in a medium- to coarse-grained matrix composed of plagioclase, orthoclase, microcline, quartz, biotite (Fig. 8b) and hornblende. A subordinate lithotype is characterized by pinkish, medium- to fine-grained, massive, leucocratic syenogranite composed of orthoclase, plagioclase, microcline, quartz, biotite (Fig. 8c-d) and hornblende. Minor bodies of granitic rocks occur within mylonite zones, including centimeter to meter-sized deformed boudins (Fig. 8e), and dikes up to 3 m-long and 1 m-thick that truncated the metasedimentary rocks in abrupt contacts (Fig. 8f). They are pinkish-grey, massive, fine- to medium-grained, and present leucogranitic composition, being composed of orthoclase, plagioclase, quartz, biotite and muscovite. All granitic rocks present intense hydrothermal alteration, with sericitization of plagioclase and K-feldspar (Fig. 8b-d) and substitution of biotite and hornblende by aggregates of intergrown chlorite, epidote, titanite and apatite. Magnetite, hematite and sulfides (primarily pyrite) are

minor alteration products.

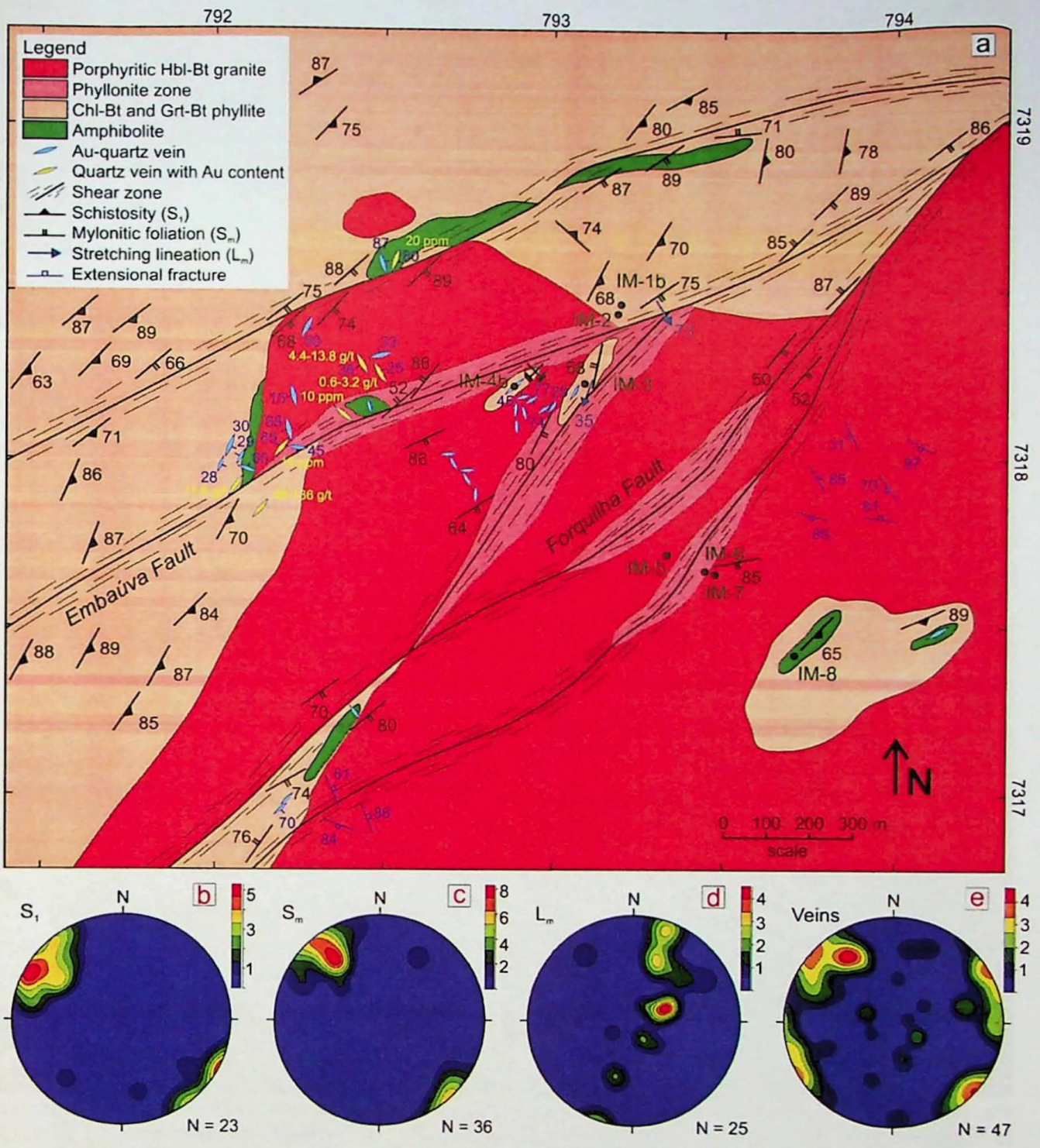

Fig. 6. (a) Detailed geological map of the Serra do Cavalo Magro orogenic gold deposit (Brazilian State of São Paulo). Equal-area, lower hemisphere stereoplots of (b) poles to regional foliation (S_1), (c) mylonitic foliation (S_m), (d) stretching lineation (L_m), and (e) poles to mineralized veins.

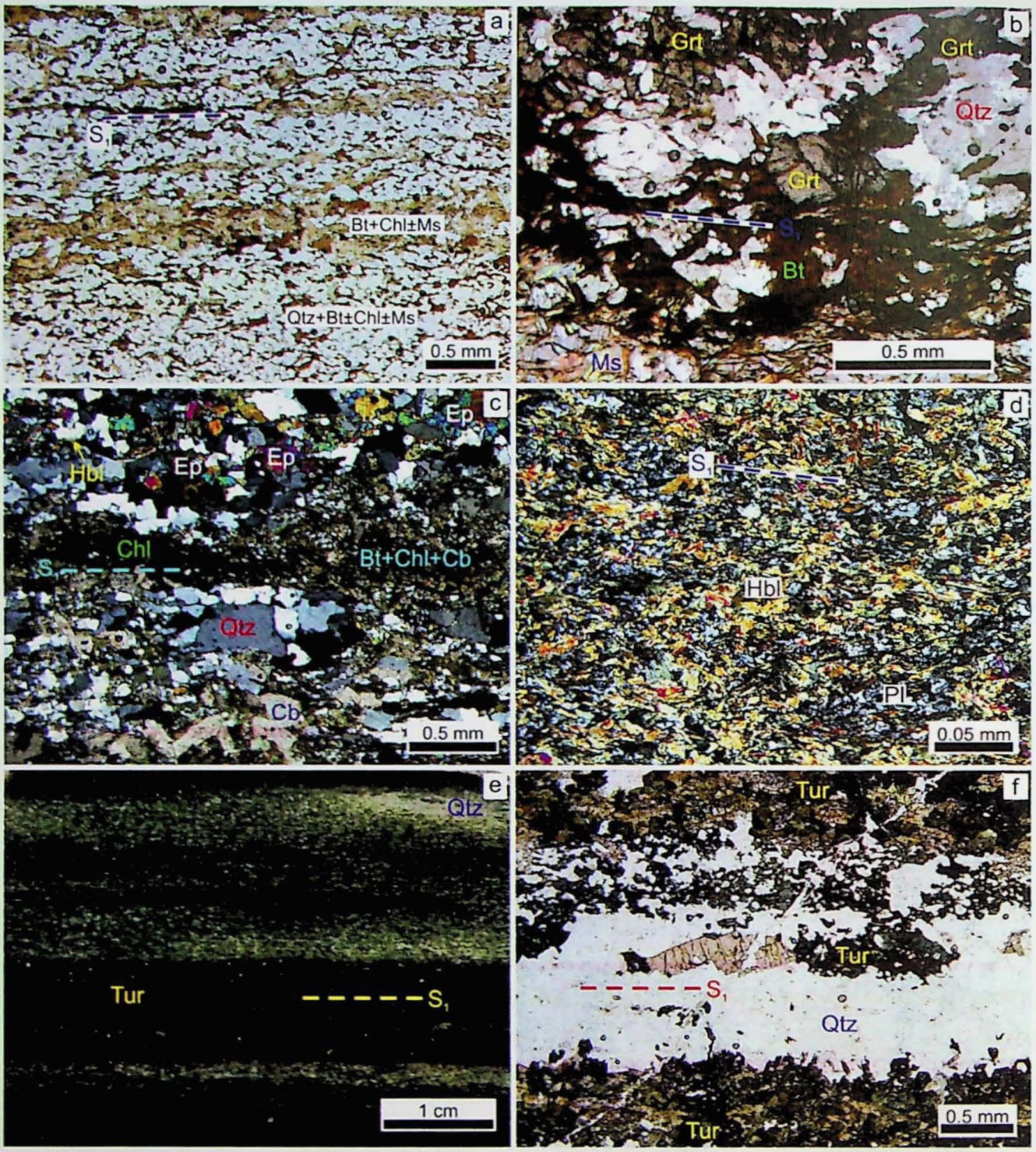

Fig. 7. Photographs and photomicrographs of the metavolcano-sedimentary lithotypes from the Piririca Formation: (a-b) phyllite rocks with granolepidoblastic levels defining S_1 schistosity, composed of two main assemblages: Qtz + Bt + Chl + Ms and Qtz + Grt + Bt + Ms. (c) granonematoblastic calc-silicate bands formed by Qtz + Ep + Hbl + Cb and lepidoblastic Chl + Bt levels parallel to S_1. (d) amphibolitic rocks with a nematoblastic texture essentially represented by Hbl + Pl along the S_1 foliation. (e-f) well-developed tourmaline-rich layers aligned parallel to the S_1 schistosity.

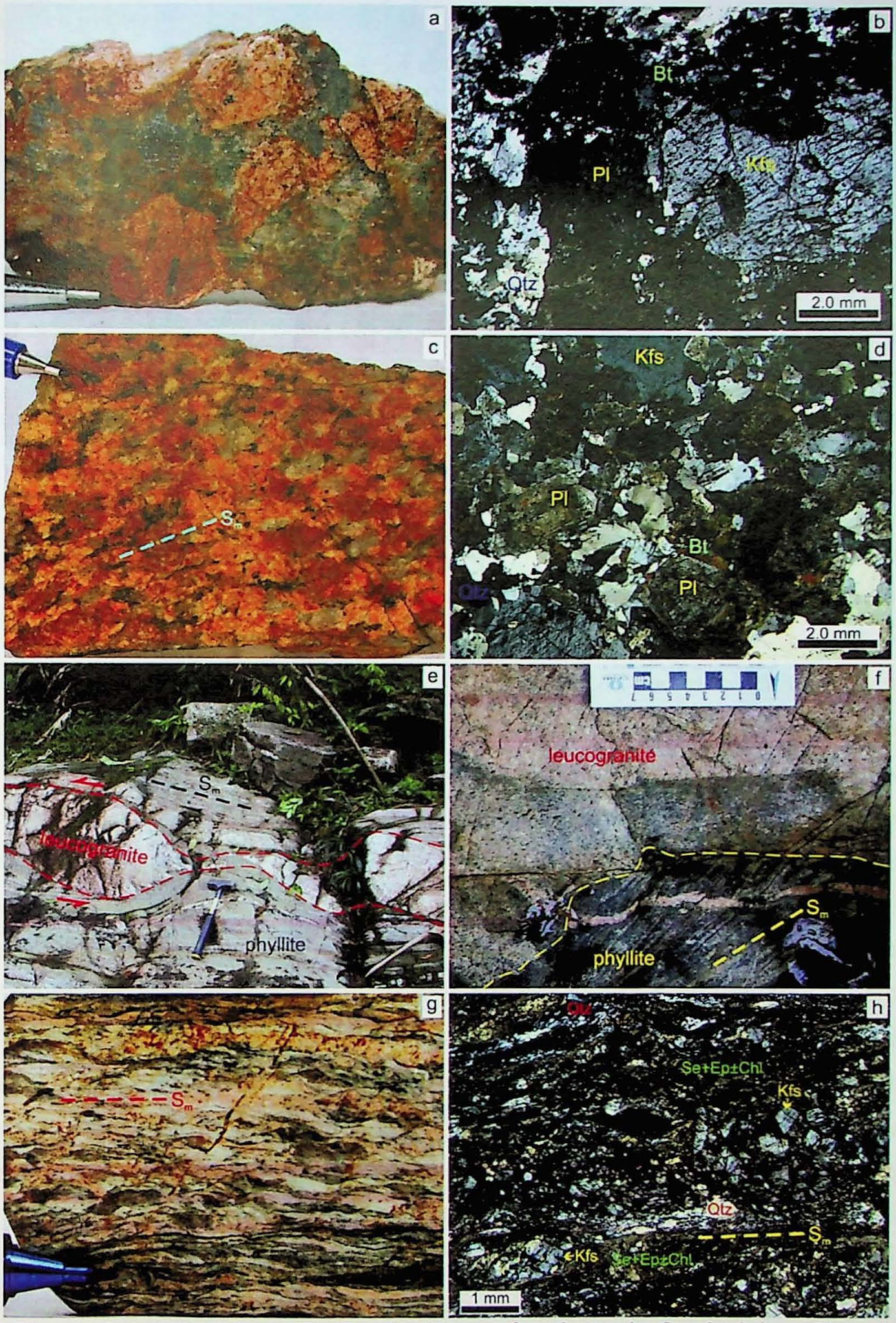

Fig. 8. Photographs and photomicrographs of granitic lithotypes from the Agudos Grandes Suite: (a-b) porphyritic monzogranite with a strong reddish weathering colour formed by Pl + Kfs + Qtz + Bt. (c-d) syenogranite composed of Kfs + Qtz + Pl + Bt. (b-d) Note the intense hydrothermal alteration, with the intense sericitization of plagioclase and K-feldspar. (e) deformed meter-sized boudins within mylonite zones indicating a sinistral sense of shear. (f) phyllite rocks intruded by leucogranitic dikes. (g-h) mylonitic fabric (S_m) well-defined in the granitic rocks, being composed of K-feldspar porfiroclasts in a very fine-matrix formed by Se + Chl + Ep + Qtz. (e-f) IM-3 outcrops location, see in Fig. 6a.

4.4.2 Structural controls

At a regional perspective, the SCMD is located close to the intersection between the Caucaia, Forquilha and Embaúva Faults (Fig. 5a-b). The Caucaia Fault extends for approximately 330 km along the N65E direction (Fig. 5a) and, in its western portion, it terminates in a first-order dextral transcurrent fault splay (Fig. 5b). The Forquilha and Embaúva Faults are sinistral transcurrent structures that extend for approximately 42 km along the N48E direction and 15 km along the N63E direction, respectively. The Forquilha Fault mostly represents the contact zone between rocks from the Votuverava Group and Agudos Grandes Suite (Fig. 6a). Truncated contacts from the latter indicate dextral displacements from 1 to 21 km along individual synthetic faults from the Caucaia Fault (Fig. 5b), and sinistral displacements up to 2 km along the Forquilha Fault and of 0.27-0.28 km along the Embaúva Fault (Figs. 5b and 6a).

At the deposit scale, the mineralization occurs in gold-bearing quartz veins concentrated within or in dilatant zones surrounding the Embaúva Fault and third-order segments of the Forquilha Fault, which form an anastomosed map-scale pattern (Fig. 6a) that reflects the structural pattern observed in field and thin-section scales. These shear zones deformed the Piririca Formation rocks and granitic rocks from the Agudos Grandes Suite. Associated mylonitic rocks display a vertical NE-trending mylonitic foliation (S_m) and an associated stretching lineation (L_m) with a bimodal subhorizontal and subvertical distribution of plunges (Fig. 6c, d). Mylonites and phyllonites from granitic protoliths display angular fragments of feldspar porphyroclasts and sigmoidal quartz aggregates in a very fine-grained matrix composed of sericite, chlorite, epidote and quartz (Fig. 8g-h). Quartz aggregates present core-and-mantle structures with elongated porphyroclasts with patchy undulose extinction surrounded by recrystallized grains of 5-20 μm in size (Fig. 8h). Sense of shear indicators (macroscopic dislocation of geological contacts (Fig. 6a), C-type shear band cleavage, asymmetric boudins (Fig. 8e), and sigma-type porphyroclasts with asymmetric strain shadows) suggest dominant sinistral strike-slip movements along the Embaúva and Forquilha Faults. Subvertical stretching lineations suggest subordinate reverse movements.

4.4.3 Mineralized vein types: morphology and microstructures

Three groups of Au-quartz veins with distinct orientation occur in the SCMD: subvertical NE-trending veins parallel to the S_m mylonitic foliation, subvertical NW-trending veins at angles of 55-85° to the fault planes, and subhorizontal NW- and NE-trending veins (Figs. 6a, 9a-f). Based on growth microstructures the subvertical NE-trending veins are

subdivided in shear veins and extensional veins, while the other vein groups are all extensional veins, as described below.

4.4.3.1 NE-trending Veins

NE-trending veins are very abundant along the mylonite zones of the Embaúva and Forquilha faults and its related second- and third-order faults, and occurs as milky-white, tabular and continuous bands (Fig. 9a-e) up to 120 m-long and 20-80 cm-thick, and as lenticular bodies and boudins within the highest deformed zones. Quartz is the essential constituent of the veins, while ore minerals occur infilling microfractures (Figs. 9d and 10a), being dominated by hematite and magnetite with minor contents of pyrite, chalcopyrite, galena, native silver, native Cu-Sn alloy and gold (Fig. 10b-d). Gold and silver occur free (Fig. 10b) or associated with pyrite filling microfractures in hematite grains (Fig. 10c). Deformation structures as boudinage, stretched and recrystallized grains (Fig. 10a), are evidence of variable degrees of shearing indicating that the Au-quartz veins were formed during the activation of the shear zones. The vein structures allow to classify them as shear veins (Hodgson, 1989; Vearncombe, 1993).

NE-trending Au-quartz veins within second and third mylonite zones display flattened quartz porphyroclasts (up to 3 mm size) with patchy-undulose extinction and deformation lamellae/bands surrounded by matrix of very fine-grained recrystallized grains (5-20 μm in size) that lead to development of a core-mantle structure (Fig. 10a). They show C-type and C'-type shear band cleavage, conjugate sets of shear bands, and microfractures filled dominantly with hematite and magnetite, with subordinate pyrite, chalcopyrite, gold, silver and Cu-Sn alloy (Fig. 10a-d). Vein growth structures are absent.

Some NE-trending veins hosted in metasedimentary rocks present elongated blocky texture with subhedral and elongated (2-4 mm size) grains oriented between 60 and 90° in relation to the veins-walls (Fig. 10e), indicating they are primarily extensional veins. Most quartz grains develop small bulges along their limits and triple junctions, while undulose extinction (Fig. 10e) and deformation lamellae are common intracrystalline deformation microstructures. These veins show solid inclusion bands (Fig. 10e) that suggest multiple crack-seal stages during their growth.

4.4.3.2 NW-trending Subvertical and Subhorizontal Extensional Veins

Extensional veins occur in dilatant zones surrounding the mylonite zones associated with the Embaúva and Forquilha Faults. They are milky, lenticular to tabular shaped veins (Fig. 9b, e, f) up to 40 m-long and 5 m-thick. Subvertical (NW-trending) and subhorizontal (NW-

and NE-trending) extensional veins cut in high-angle the S_m mylonitic foliation and the S_1 schistosity (Fig. 9b, e, f) and are oriented between 55 and 85° in relation to the Embaúva and Forquilha Faults planes.

The extensional veins are dominated by elongate blocky texture with an internal domain (vein center) formed by elongated 0.8-1.2 mm-size quartz grains with aspect ratio from 2:1 to 3:1 and oriented between 70-90° perpendicular to the walls. Quartz grains show undulose extinction, deformation lamellae, and grain boundaries decorated by restricted domains of recrystallized grains of 5-20 μm in size. An external domain is defined by fine-grained (0.4 mm size) equidimensional quartz grains parallel to the walls. A mineralogical zoning represented by the alternation between quartz-rich domains and solid inclusion bands of the same vein-walls composition suggest that mineral precipitation occurred as a response to cyclic stages of crack-seal during vein growth. Field and microstructural geometric patterns indicate the extensional veins were crystallized during syn- to late- deformation events, once they were folded in the highest deformed zones and assimilate small fragments of surrounding host rocks (Fig. 9f), cross-cut the NE-trending Au-quartz shear veins (Fig. 9b), and show intracrystalline and dynamic recrystallization microstructures.

4.5 Metamorphic history of metasedimentary host rocks

Two representative phyllite samples (IM-1b and IM-4b) hosting Au-quartz veins were selected to petrological modelling and geothermobarometry. Table 1 presents representative chemical mineral analyses.

Sample IM-1b comprises the assemblage biotite-chlorite-muscovite-albite-oligoclase-quartz-hematite and shows a well-developed schistosity (S_1) defined by the orientation of biotite (X_{Mg} from 0.321-0.361), muscovite (X_{Mg} from 0.277-0.437), and chlorite (X_{Mg} from 4.820-5.171). These minerals occur within the matrix as highly elongated flakes (up to 0.5 mm large) that in most cases are oblique to the S_1 schistosity, defining a C-type shear band cleavage. Locally, muscovite and chlorite are present along axial surfaces of kinked schistosity S_1. Matrix plagioclase grains (up to 0.2 mm large) display a strongly variation of anorthite content (1-18 mol%) (Table 1). Quartz occurs as isolated porfiroclasts and/or forming polycrystalline ribbon-shaped aggregates with grain-sizes from 0.2-0.5 mm, showing patchy-undulose extinction, deformation lamellae, serrated limits.

Sample IM-4b comprises the assemblage garnet-biotite-muscovite-hematite/ilmenite-magnetite. Biotite (X_{Mg} from 0.157-0.248; Table 1) and muscovite flakes are within the matrix defining the main schistosity (S_1). Garnet occurs as anhedral to fragmentated porfiroblasts (3-5

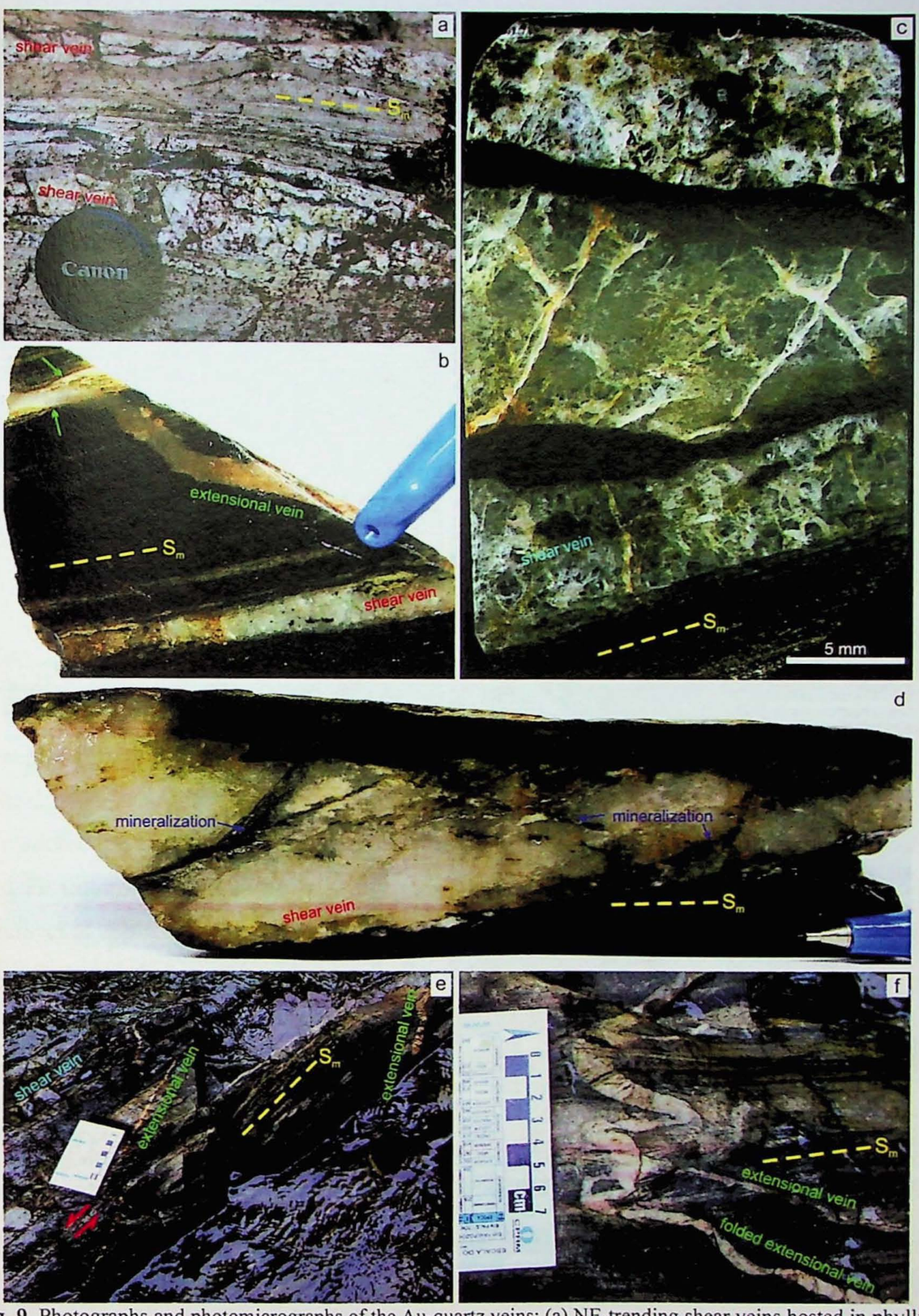

Fig. 9. Photographs and photomicrographs of the Au-quartz veins: (a) NE-trending shear veins hosted in phyllite rocks from Piririca Formation. (b) millimeter-thick extensional vein cross-cutting the NE-trending shear veins. (c) macro-scale of quartz grains elongated blocky texture in shear veins parallel to the S_m foliation. (d) detail of white-quartz shear vein full-filled by gold, silver, sulfides and iron oxides in the microfractures. (e) centimeter-thick extensional veins cross-cutting at high-angle the phyllite rocks (Piririca Formation) and shear veins. Note the small sinistral displacement in red arrows. (f) folded extensional vein assimilating small fragment of the immediate host rocks. (a-e) IM-3 outcrops location, see in Fig. 6a.

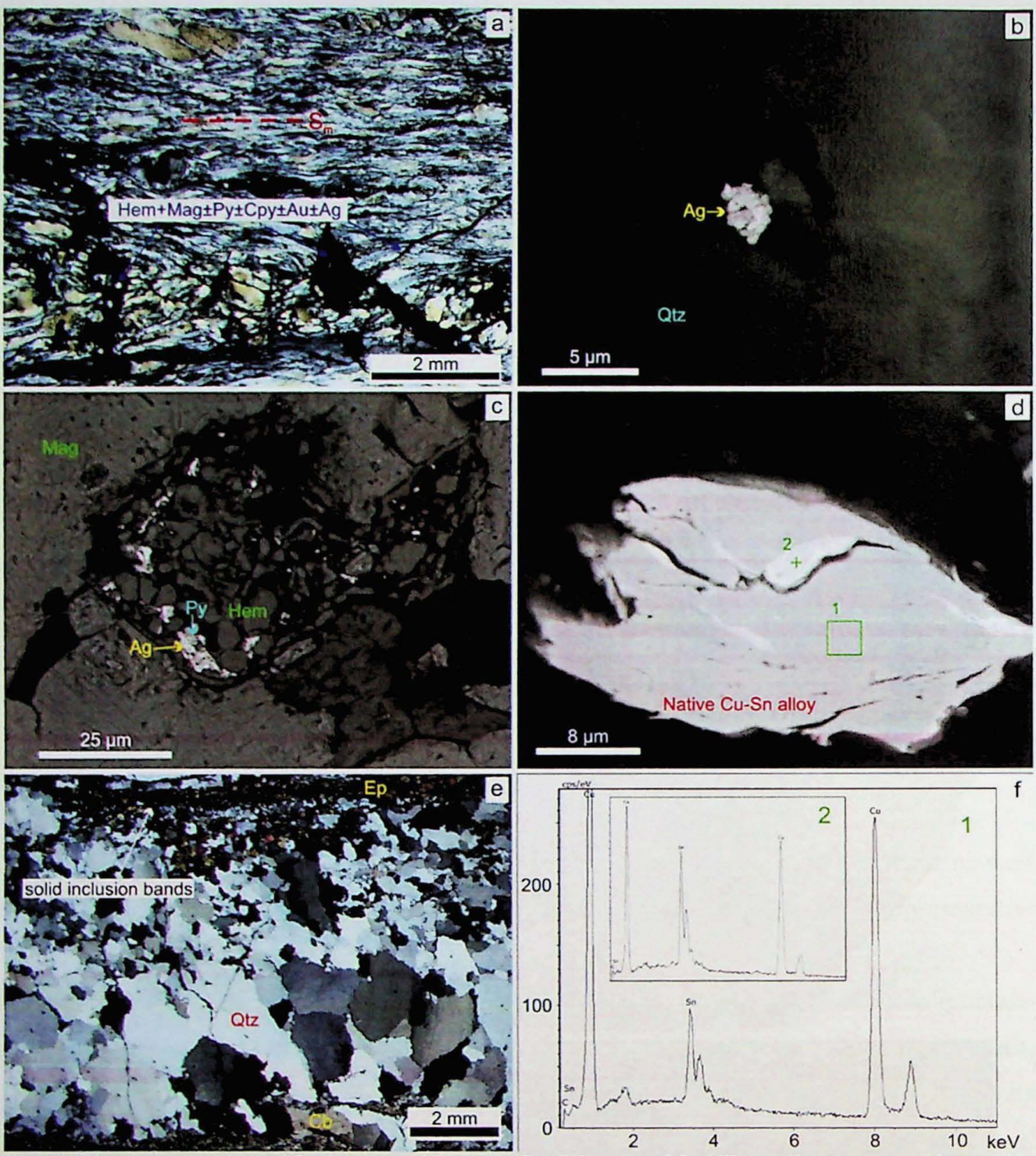

Fig. 10. Photomicrographs and Back-scattered Electron (BSE) images of the NE-trending Au-quartz shear veins: (a) microscopic features showing flattened quartz porphyroclasts and shear fractures filled by Hem + Mag ± Py ± Cpy ± Au ± Ag along with the S_m foliation. (b-c) detail of the ore minerals that occurs infilling microfractures. (d-f) native Sn-Cu alloy as indicated by Energy-Dispersive X-ray Spectroscopy (EDS) analyses. (e) elongated blocky texture of quartz and solid inclusion bands composed of Ep + Cb.

mm large) (Fig. 11a-e) and is dominated by almandine (28-52 mol%) and spessartine (35-48 mol%) components (Table 1). Compositional X-ray maps (Fig. 11a-d) show truncated chemical zoning with depletion in spessartine and grossular contents and increase in almandine and pyrope contents from cores to rims (Fig. 11e-f). This zoning pattern strongly suggests partial preservation of prograde growth zoning and superposed post-growth resorption. Quartz grains

are present as aggregates (up to 0.6 mm-large) with lobate boundaries and undulose extinction.

4.5.1 Isochemical phase diagram modeling

P-T isochemical phase diagrams were constructed for samples IM-1b and IM-4b compositions using the Perple_X software (Connolly, 2005), version 6.7.5, and the internally consistent thermodynamic database of Holland and Powell (2011). Samples were modeled in the MnO-Na_2O-CaO-K_2O-FeO-MgO-Al_2O_3-SiO_2-H_2O-TiO_2-Fe_2O_3 (MnNCKFMASHTO) system. The solution models for chlorite, muscovite, biotite, garnet, staurolite, and ilmenite are from White et al. (2014), while epidote is from Holland and Powell (2011) and feldspar is from Fuhrman and Lindsley (1988). Quartz, titanite, and rutile are considered as pure phases, while H_2O is considered as saturated component. The Fe_2O_3 content was adjusted for each single bulk rock composition to reproduce the minor Fe-Ti-oxide phases observed in thin sections.

In the *P-T* phase diagram calculated for sample IM-1b (Fig. 12a) the five-variant peak metamorphic assemblage (Bt-Chl-Ms-Ab-Qtz-Hem-oligoclase; abbreviations after Whitney and Evans, 2010) is stable at conditions of 465-570 °C and 1-8 kbar. This stability field is limited by reactions where biotite is stabilized at expense of chlorite and epidote and rutile become unstable (lower temperature limit) and albite coexists with oligoclase. For the considered bulk composition, chlorite becomes unstable above 500 °C at 1 kbar and 580 °C at 8 kbar, and staurolite firstly appears above 530 °C (Fig. 12a). Garnet is not stable at the considered P-T range. The peak assemblage field was contoured with isopleths of X_{Mg} in biotite and Fe (atoms per formula unitary - a.p.f.u) in muscovite, and the measured compositions intersect at approximately at 560 °C and 7 kbar, which are inferred as the best estimate for the peak metamorphic conditions for sample IM-1b.

In the phase diagram calculated for sample IM-4b (Fig. 12b) the observed peak assemblage (Grt-Bt-Ms-Hem/Ilm-Mag) is stable at conditions of 500-750 °C and above 4 kbar. This field is limited by reactions where garnet is stabilized at expense of chlorite, which is exhausted (lower temperature limit), and muscovite breaks-down to form a melt phase (upper temperature limit). The peak assemblage field was contoured with isopleths of the ratio grossular/spessartine in garnet and Si (a.p.f.u) in muscovite, and the measured compositions intersect at approximately at 625 °C and 6.8 kbar, which are inferred as the best estimate for the peak metamorphic conditions for sample IM-4b.

Table 1: Representative microprobe analyses of the metamorphic minerals from the Piririca Formation.

Sample	IM-4b					IM-1b				
Mineral	Grt	Grt	Grt	Ms	Ms	Bt	Bt	Chl	Ms	Pl
Location	C	I		-	-	C	R	-	-	-
SiO_2	36.74	36.59	36.06	44.76	44.9	32.54	29.05	23.09	45.64	64.76
Al_2O_3	20.44	19.79	20.65	32.84	32.02	19.99	19.97	22.36	37.24	22.40
FeO (*)	14.92	13.96	23.55	4.28	4.39	24.62	27.46	30.95	1.13	0.09
MnO	21.44	20.76	15.07	0.05	0.05	0.13	0.13	0.20	0.00	0.00
CaO	6.12	7.93	3.73	0.00	0.00	0.00	0.05	0.00	0.00	3.13
Cr_2O_3	0.00	0.00	0.00	n.a	n.a	n.a	n.a	n.a	n.a	n.a
ZnO	n.a	n.a	n.a	0.04	0.00	0.02	0.01	0.01	0.02	n.a
Cl	n.a	n.a	n.a	0.00	0.01	0.07	0.09	0.03	0.00	n.a
K_2O	n.a	n.a	n.a	11.36	11.45	9.19	5.92	0.01	10.03	0.06
SrO	n.a	n.a	n.a	n.a	n.a	n.a	n.a	n.a	n.a	0.08
TiO_2	0.11	0.067	0.03	0.15	0.03	1.31	1.20	0.04	0.23	0.00
BaO	n.a	n.a	n.a	0.16	0.04	0.02	0.00	0.00	0.13	0.00
F	n.a	n.a	n.a	0.06	0.06	0.04	0.03	0.02	0.01	n.a
Na_2O	n.a	n.a	n.a	0.13	0.12	0.06	0.05	0.00	0.96	9.78
MgO	0.15	0.17	0.26	0.58	0.67	6.91	7.76	10.10	0.4	0.00
Total	99.93	99.27	99.35	94.43	93.77	94.90	91.72	86.82	95.83	100.3
Oxygen	12	12	12	22	22	22	22	14	22	8
Si	2.989	2.988	2.966	6.163	6.228	5.138	4.779	3.643	6.034	2.844
Al	1.960	1.905	2.002	-	-	-	-	-	-	-
Al^{iv}	-	-	-	1.837	1.772	2.862	3.221	4.357	1.966	-
Al^{vi}	-	-	-	3.494	3.463	0.858	0.652	0.210	3.837	-
Fe	-	-	-	0.493	0.509	3.251	3.778	4.084	0.125	0.003
Fe^{3+}	0.0484	0.112	0.063	-	-	-	-	-	-	-
Fe^{2+}	0.9668	0.842	1.557	-	-	-	-	-	-	-
Mn	-	-		0.006	0.006	0.018	0.018	0.0269	0.00	0.000
Mn^{3+}	0.000	0.000	0.000	-	-	-	-	-	-	-
Mn^{2+}	1.477	1.436	1.050	-	-	-	-	-	-	-
Zn	-	-	-	0.004	0.000	0.003	0.001	0.001	0.002	-
Cl	-	-		0.000	0.002	0.020	0.026	0.017	0.000	-
K				1.995	2.026	1.851	1.242	0.005	1.691	0.003
Ca	0.533	0.694	0.329	0.000	0.000	0.000	0.008	0.000	0.000	0.147
Sr	-	-		-	-	-	-	-	-	0.002
Cr	0.000	0.000	0.000	-	-	-	-	-	-	-
Ti	0.007	0.004	0.002	0.016	0.003	0.155	0.148	0.005	0.023	0.000
Ba	-	-	-	0.009	0.002	0.001	0.000	0.000	0.007	0.000
F	-	-	-	0.027	0.026	0.018	0.017	0.021	0.004	-
Na	-	-	-	0.035	0.032	0.018	0.015	0.000	0.246	0.833
Mg	0.018	0.021	0.032	0.119	0.139	1.626	1.903	2.376	0.079	0.000
Total	8.000	8.000	8.000	14.198	14.209	15.820	15.808	14.745	14.015	4.993
X_{Mg}	0.018	0.021	0.019	0.195	0.214	0.333	0.335	5.084	0.386	-
X_{Fe}	0.982	0.979	0.981	0.805	0.786	0.667	0.665	0.632	0.614	-
$X_{Alm\ (\%)}$	32.23	28.05	51.91	-	-	-	-	-	-	-
$X_{Grs\ (\%)}$	15.37	18.01	10.40	-	-	-	-	-	-	-
$X_{Sps\ (\%)}$	49.25	47.86	34.99	-	-	-	-	-	-	-
$X_{And\ (\%)}$	2.07	4.91	0.45	-	-	-	-	-	-	-
An (%)	-	-	-	-	-	-	-	-	-	14.976
Ab (%)	-	-	-	-	-	-	-	-	-	84.682
	-	-	-	-	-	-	-	-	-	0.342

(*) Fe_2O_3 for Pl analyses; n.a. - not analyzed; C - core, R - rim, I - intermediate.
Mineral abbreviations from Whitney and Evans (2010)

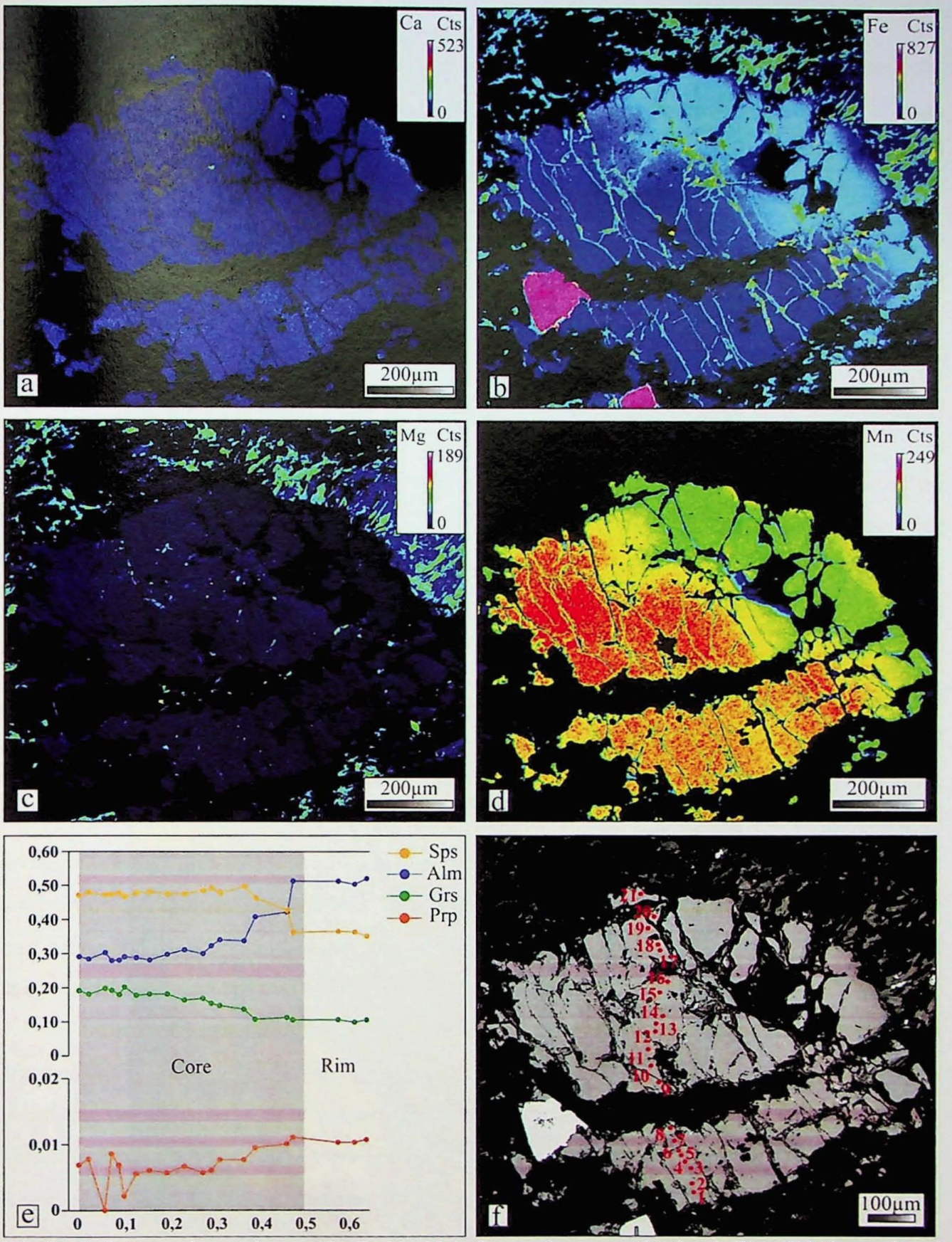

Fig. 11. (a-d) X-ray elemental maps (Ca, Fe, Mg, Mn) of garnet from garnet-biotite phyllites (IM-4b sample) of the Piririca Formation. The images emphasize the partial preservation of prograde growth zoning of Ca, Fe, and Mn. (e) chemical profile of garnet porphyroblast from sample IM4-b. (f) location of microprobe spot analyses.

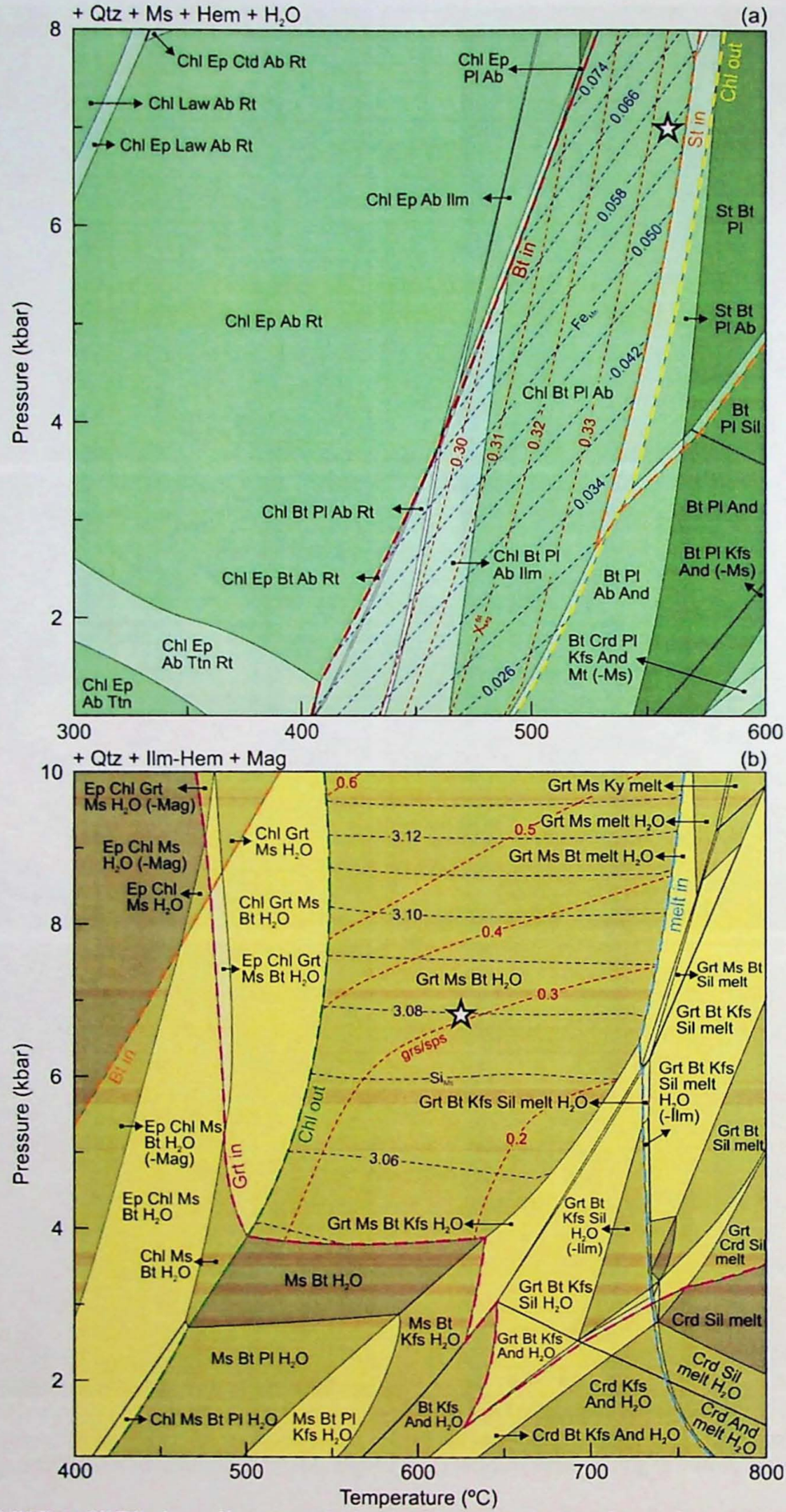

Fig. 12. MnNCKFMASHTO phase diagrams calculated with the Perple_X software for samples IM-1b (a) and IM-4b (b). The fields of equilibrium peak assemblages are superimposed by the isopleths crossing of X_{Mg} in biotite and FeO in muscovite (a) and of grs/sps in garnet and SiO_2 in muscovite (b). In both, the peak P-T conditions are shown by white stars.

4.6 Fluid Inclusions

Detailed fluid inclusion petrography was performed on 20 double-polished thin sections (100-200 μm-thick) of the NE-trending Au-quartz shear and extensional veins, and from these, 8 samples were selected for microthermometric analyses, including samples with preserved vein-growth microstructures, weak and strong ductile deformation. The presence of well-preserved secondary fluid inclusion trails occurring along sealed microfractures was the criteria adopted for sample selection, once microstructural and textural evidence suggests that the gold precipitation was coeval with the deformation stages of these veins. Thus, we have evidence to interpret that the primary fluid inclusions are unrelated with the gold mineralization event.

4.6.1 Fluid inclusion types and assemblages

Four fluid inclusions types with size ranging from 2-20 μm were identified based on phases observed at room temperature and components determined from heating-freezing experiments and Raman spectroscopy analyses. These are, in decreasing order of abundance, carbonic (CO_2-rich), aqueous (H_2O), aqueous-carbonic (H_2O-CO_2), and multiphase (H_2O-salt) inclusions.

Carbonic inclusions are common and comprise a liquid CO_2 of darkish color with rounded, irregular, and flattened shapes. Aqueous inclusions consist of tubular, oblate, and negative crystal shaped-inclusions and contain a liquid-phase and a vapor-phase representing 10-30 vol.% of the total inclusions. Aqueous-carbonic inclusions usually exhibit rounded or irregular shapes, consisting of liquid H_2O-rich and liquid CO_2-rich phases. The CO_2 volumetric proportion varies from 30 to 99 vol.% of the total inclusions. Multiphase inclusions display negative crystal or irregular shapes, and contain a liquid and a vapor H_2O-rich phase (5-30% of the total inclusions), and one or more sylvite daughter crystals.

Fluid inclusion assemblages (FIAs) are defined as associations of coeval fluid inclusions trapped at about the same time and petrographically associated (Goldstein and Reynolds, 1994). Applying this definition, three assemblages have been recognized in the NE-trending Au-quartz shear and extensional veins: FIA-1 (carbonic, aqueous, and aqueous-carbonic inclusions; Fig. 13a-c), FIA-2 (carbonic and aqueous inclusions; Fig. 13d), and FIA-3 (two-phase solid-absent hypersaline inclusions and multiphase solid-bearing inclusions; Fig. 13e-f). The physicochemical data of each group is summarized in Table 2.

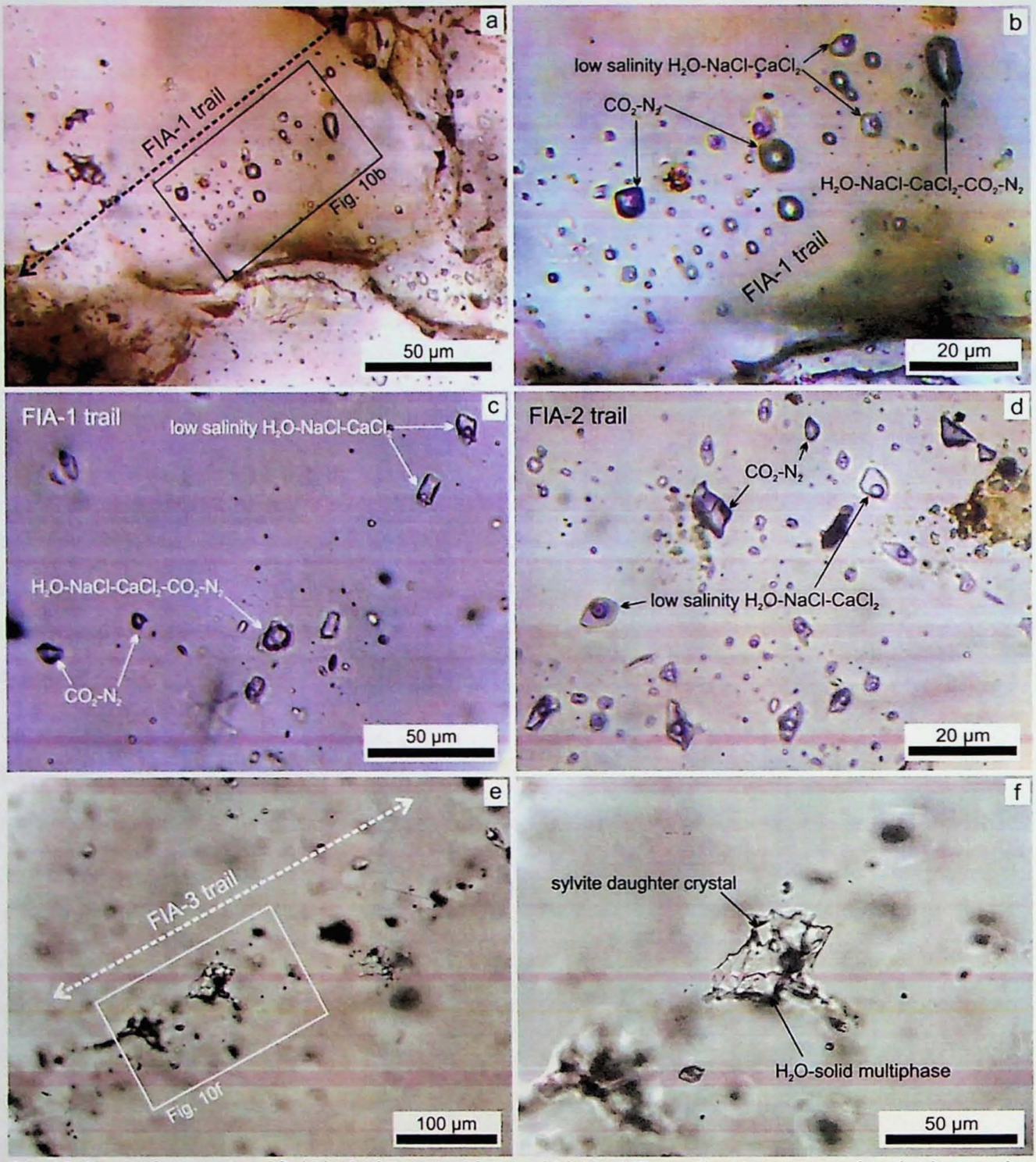

Fig. 13. Photomicrographs of fluid inclusion assemblages within the NE-trending Au-quartz veins. (a-c) secondary well-preserved trails showing the coexistence of carbonic, aqueous, and aqueous-carbonic inclusions (FIA-1). (d) FIA-2 represented by aqueous and carbonic inclusions of highly varied sizes. (e) well-defined secondary trail of multiphase solid-bearing and solid-absent hypersaline inclusions. (f) multiphase inclusion exhibiting one sylvite daughter crystal.

Carbonic inclusions (FIA-1 and 2) show nearly consistent T_mCO_2 values between -57.5 and -56.6 °C with only a few exceptions ranging from -58 to -59 °C (Fig. 14a). Homogenization occurred into the liquid state between -3 and 31 °C (Fig. 14b). Laser Raman analyses detected 98-99 mol% of CO_2 and 1-2 mol% of N_2 (Fig. 15). Homogenization temperature (T_hCO_2) values indicate density in the interval of 0.5-0.9 g/cm^3, taking into account the minor N_2 contents.

Aqueous inclusions are divided into two types based on T_E, $T_m$ice, and defined assemblages. Initial eutectic melting occurred in the intervals of -55.4 and -36.5 °C (FIA-1 and FIA-2), and -66.5 and -60.3 °C (FIA-3) (Fig. 14c). Final ice melting values and respective salinities range from -12.4 to -0.4 °C (1-16 wt.% NaCl eq.) (FIA-1 and FIA-2), and from -24.6 to -22.9 °C (25 wt.% NaCl eq.) (FIA-3) (Fig. 14d, e). Homogenization (T_h) occurred into the liquid state ranging from 150-350 °C (FIA-1 and 2), and 222-286 °C (FIA-3) (Fig. 14f).

Aqueous-carbonic inclusions showed a narrow T_mCO_2 interval between -57.4 and -56.6°C (Fig 14a), very close to the triple point for pure CO_2, which suggests very small amounts of others volatile species. Laser Raman analyses confirmed that these inclusions are constituted of 99 mol% of CO_2 and 1 mol% of N_2 (Fig. 15). Clathrate dissociation occurred in the presence of CO_2 vapor within the range of 1.5-14.5 °C (Fig. 14h), corresponding to salinities of 1-18 wt.% NaCl eq. Initial eutectic melting was recognized only in a few inclusions between -55.2 and -42.2 °C. T_hCO_2 varies within 20.6-30.4 °C (into a liquid state) (Fig. 14b) and yield densities in the range of 0.5-0.8 g/cm^3. T_h occurred upon expansion of carbonic-rich phase or into the liquid state between 209 and 366 °C (Fig. 14f).

Multiphase inclusions display T_E and $T_m$ice values ranging from -79.7 to -63.3 °C, and -41.4 to -23.7°C (Fig. 14c), respectively. Sylvite dissolution (T_s) occurred mainly before aqueous phase homogenization from 196 to 283 °C (Fig. 14i), corresponding to salinities of 25-33 wt.% NaCl eq. (Fig. 14d). Aqueous phases homogenized into a liquid and vapor state between 234 and 475 °C (Fig. 14g). This inclusion type corresponds a distinct event of fluid percolation unrelated to gold mineralization, and therefore, was disregarded from interpretation.

The microthermometric data of each inclusion type are summarized in Table 3.

Table 2: Summary of fluid inclusion assemblages with respect to fluid inclusion type, timing, and vein type.

Assemblage	Type	Timing	Vein type
1	C, Aq*, AqC	Secondary	NE-trending Au-quartz veins
2	C, Aq*		
3	M, Aq**		

(*) Low to moderate salinity; (**) High salinity. Abbreviations and major components: C - carbonic ($CO_2 \pm N2$), Aq - aqueous (H_2O-NaCl-$CaCl_2$), AqC - aqueous-carbonic (H_2O-NaCl-$CaCl_2$-$CO_2 \pm N_2$), M - multiphase and aqueous (H_2O-NaCl-$CaCl_2$-KCl) inclusions

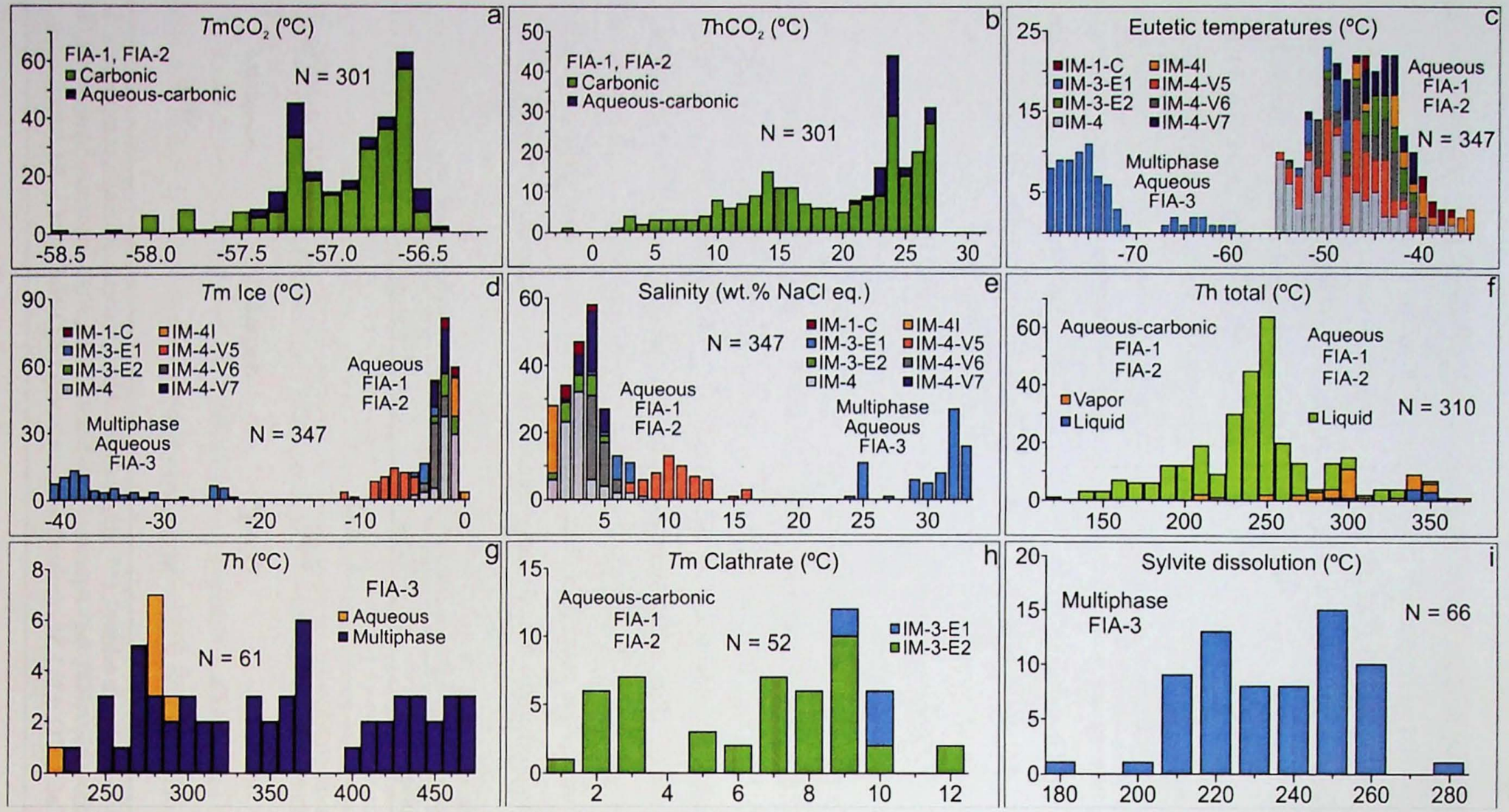

Fig. 14. Histograms showing microthermometric data obtained on FIA-1, FIA-2, and FIA-3 from NE-trending Au-quartz veins at the Serra do Cavalo Magro deposit.

Table 3: Summary of the microthermometric fluid inclusion data from NE-trending Au-quartz veins.

Vein Type	FIA	Fluid System	Mode of occurrence	TmCO$_2$ (°C)	ThCO$_2$ (°C)	TmCl (°C)	TE (°C)	Tm ice (°C)	Th (°C)	Ts (°C)	Salinity (wt.% NaCl equivalent)	n	Samples	Deformation grade
NE-trending Au-quartz veins	1	H_2O-NaCl-$CaCl_2$	Trail				-41.1 to -52.5	-0.6 to -4.5	138 to 335 L		1.05 to 7.16	46	IM-3-E1 IM-3-E2	Extensional veins ⊖
		CO_2-N_2		-57.3 to -56.6	22.3 to 31							45	IM-3-E1 IM-3-E2	
		H_2O-NaCl-$CaCl_2$-CO_2-N_2		-56.4 to -57.4	20.6 to 31	1 to 11.5	-42.2 to -55.2		295 to 362 L 209 to 366 V		0.7 to 17.68	50	IM-3-E1 IM-3-E2	
	2	H_2O-NaCl-$CaCl_2$					-55.4 to -34.6	-12.4 to -0.4	140 to 351 L		0.7 to 16.33	226	IM-4 IM-4-I IM-4-V5 IM-4-V6 IM-4-V7	Shear veins ⊕
		CO_2-N_2		-58.5 to -56.5	-3.0 to 30							240	IM-4 IM-4-I IM-4-V5 IM-4-V6 IM-4-V7	
	3	H_2O-NaCl-$CaCl_2$-KCl					-60.3 to -65.9	-22.9 to -24.6	222 to 286 L		24.23 to 25.24	6	IM-3-E1	Extensional veins ⊖
		H_2O-solid multiphase					-79.9 to -61.8	-41.4 to -23.7	234 to 475 L 423 to 467 V	180 to 283	24.71 to 33.23	69	IM-3-E1	

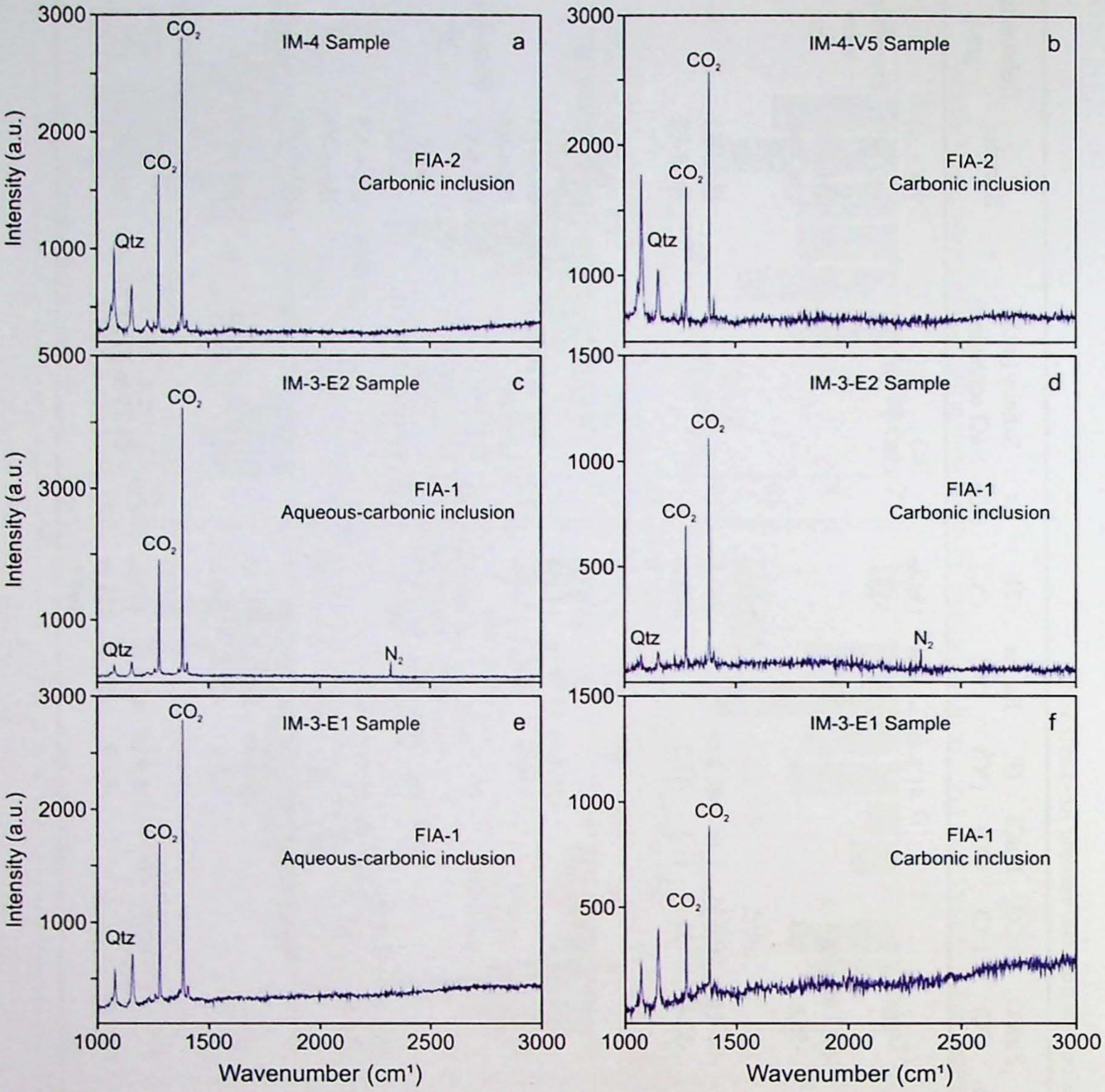

Fig. 15. Representative Raman spectra obtained on carbonic and aqueous-carbonic inclusions from FIA-1 and 2 of the NE-trending Au-quartz shear (IM4 and IM-4-V5 sample) and extensional veins (IM-3-E1 and IM-3-E2 sample).

4.6.2 Interpretation of fluid inclusion data

The presence of aqueous-carbonic, carbonic-rich, and aqueous inclusions in the FIA-1, could be explained by (1) post-entrapment selective H_2O-loss from a homogenous H_2O-CO_2 parental fluid during the crystal-plastic deformation (e.g., Crawford and Hollister, 1986; Bakker and Jansen, 1990; Hollister, 1990; Johnson and Hollister, 1995; Faleiros et al., 2010); by (2) entrapment of two unmixed fluids from a parental homogeneous fluid (fluid immiscibility) (e.g., Ramboz et al., 1982; Dugdale and Hagemann, 2001; Faleiros et al., 2007, 2014); or by (3) mechanical mixing between fluids of different compositions (e.g., Ramboz et al., 1982; Anderson et al., 1992). If post-entrapment modifications and selective H_2O-loss acted in the

aqueous-carbonic fluid inclusions, it would be possible to test its effects using plots of CO_2 volumetric ratio (V_{CO2}) against density and salinity (e.g., Faleiros et al., 2007, 2014). Fig. 16a shows a large fluctuation of CO_2-rich phase density from 0.5 to 0.8 g/cm^3, without V_{CO2} dependency factor. In this case, the H_2O-loss cannot be responsible for changes of V_{CO2}, once it would be expected a correlation with CO_2 density (e.g., Faleiros et al., 2007, 2010). Furthermore, Fig. 16b displays of negative correlation between V_{CO2} and salinity, which does not corroborate with the strain-induced H_2O-loss, once this post-entrapment process leads to the increase of NaCl and $CaCl_2$ (e.g., Hollister, 1990).

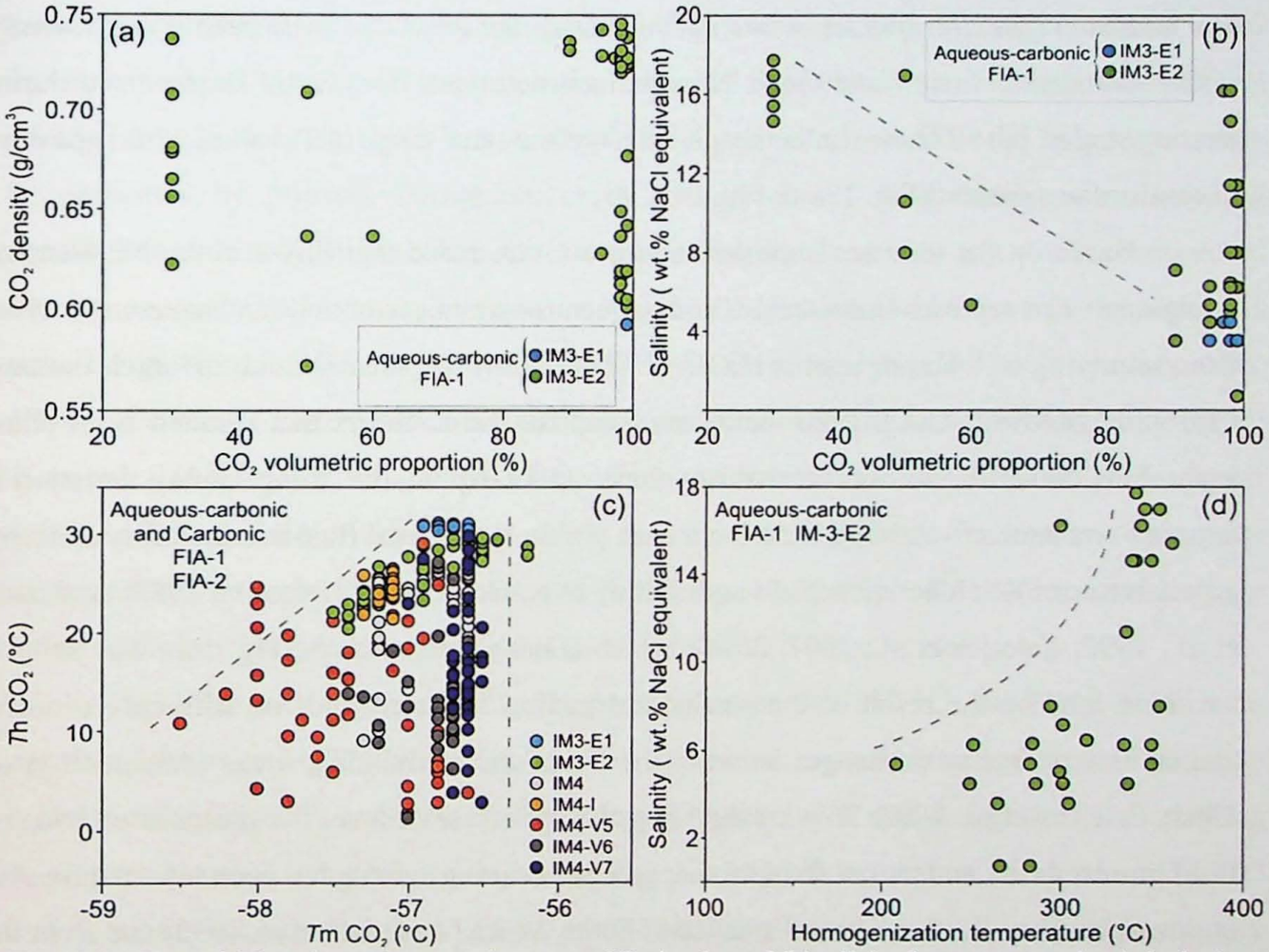

Fig. 16. (a) Plots of CO_2 volumetric proportion versus CO_2 density and (b) salinity for aqueous-carbonic inclusions (FIA-1). (c) variation diagram relating triple point and homogenization temperatures of CO_2 carbonic and aqueous-carbonic inclusions (FIA-1 and 2). The positive correlation is interpreted as a consequence of N_2 depletion through time. (d) plot of salinity against total homogenization temperature for aqueous-carbonic inclusions (FIA-1). Note a general positive correlation.

If fluid immiscibility operated as the main mechanism, three general criteria must be satisfied, according to Ramboz et al. (1982):

The different inclusion types must occur in the same regions of the same sample, and there must be excellent evidence of their contemporaneous trapping. The FIA-1 consist of three

distinct inclusion types (carbonic, aqueous-carbonic and aqueous) occurring within individual secondary trail (Fig. 13a-c), which is unequivocal evidence for coeval trapping.

The different inclusion types must homogenize within the same range of temperature by opposite modes (into the liquid and vapor phase), reflecting contrasting densities. The FIA-1 exhibits the same T_h values from aqueous inclusions (homogenization into the liquid state) and aqueous-carbonic inclusions (homogenization upon expansion of the carbonic-rich phase or into the liquid state) (Fig. 14f).

The bulk molar volumes of lower and higher density phase-rich fluid inclusions types must be compatible with equilibrium coexistence at a unique value of T_h. As consequence, if one inclusion type decrepitates before homogenizing, the other type must behave equivalently, if they are similar in size and shape. None of inclusion types from FIA-1 decrepitated during heating stages, but all show similar shape, size, and the same range of T_h values, although some exceptions are present (Fig. 13a-d; Fig. 14f).

Based on the tests accomplished above, we concluded that FIA-1 in the NE-trending Au-quartz veins represent immiscible fluids (aqueous-carbonic, carbonic, and aqueous) derived from unmixing of a homogeneous H_2O-NaCl-$CaCl_2$-CO_2-N_2 parental fluid, in which the pure CO_2 and H_2O-NaCl-$CaCl_2$ fluid inclusions comprise end-members that resulted from phase separation. Nevertheless, this mechanism alone cannot explain the strong salinity variation in aqueous and aqueous-carbonic fluid inclusions (Table 3), once the fluid immiscibility endorses a positive correlation between X_{H2O} and salinity (e.g., Bowers and Helgeson, 1983; Anderson et al., 1992; Faleiros et al., 2007, 2014), which is not observed in the Fig. 16b. The salinity variation may be the result of the mechanical mixing between fluids of different salinities; and/or heterogeneous exchanges between the fluids and surrounding rocks (Anderson et al. 1992; Faleiros et al. 2007, 2014). Regarding the hypotheses above, the presence of coupled fluid immiscibility and partial fluid mixing processes during veining has been reported for Au-quartz veins from the Transvaal Sequence of South Africa (Anderson et al.,1992) and from the Morro do Ouro Mine orogenic gold deposit, southern Ribeira Belt, Brazil (Faleiros et al., 2014).

Fig. 16c exhibits a positive correlation between T_mCO_2 and T_hCO_2 for aqueous-carbonic and carbonic inclusions (FIA-1, 2), suggesting an evolution of the CO_2-N_2-bearing fluid system associated with N_2 depletion through time. Furthermore, Fig. 16c shows a systematic variation of T_hCO_2 regardless T_mCO_2 values, which strongly indicates pressure fluctuations at the time of fluid entrapment (e.g., Robert and Kelly, 1987; Dugdale and Hagemann, 2001; Faleiros et al., 2007, 2014; Wang et al., 2015). Fig. 16d displays of a positive correlation between salinity and T_h for aqueous-carbonic inclusions, which suggests a concomitant salinity depletion.

4.6.2.1 Aqueous Fluids

Eutectic melting temperatures from aqueous inclusions (FIA-1 and FIA-2) range mainly between -56 and -42 °C (Fig. 17a), suggesting a compositional system composed by H_2O-NaCl-$CaCl_2$ (e.g., Roedder, 1984; Goldstein and Reynolds, 1994; Steele-MacInnis et al., 2016). Large deviation of values in relation to the stable eutectic of this pure system (-52 °C) may indicate the presence of others dissolved salts such as $MgCl_2$ and $FeCl_2$, or may be related with metastability of the H_2O-NaCl-$CaCl_2$ system (e.g., Goldstein and Reynolds, 1994).

Bivariate plots of salinity against homogenization temperature (T_h) from aqueous fluids were used to evaluate the processes involved during their evolution. Fig. 17b displays two main patterns, one that reflects a clustering of T_h at 230-250 °C and small dispersion towards lower T_h values with salinity relatively constant for individual fluid inclusion trails within the interval of 0.5-2.5 wt.% NaCl eq. (trails 2, 3, 4; sample IM-4; trail 1; sample IM-4-I). This pattern may be explained by pressure fluctuation, or by a trajectory of fluid cooling. Post-trapping modifications do not justify a strong concentration at highest T_h values, as it would be expected a major concentration in lower T_h values and a minor dispersion of data towards the higher T_h values (e.g., Kerrich, 1976; Wilkins and Barkas, 1978; Roedder, 1984; Goldstein and Reynolds, 1994). The second pattern presents a positive correlation between T_h and salinity values (trail 1, sample IM-4; trail 1, sample IM-3-E1), which can be explained by the mixing of a lower saline and cold fluid with a higher saline hot fluid, but pressure fluctuations cannot be disregarded. The same pattern is observed in the Fig. 17c (sample IM-4-V5), considering a larger spectrum for T_h values (150-300 °C) and salinities (7-16 wt.% NaCl eq.).

Fig. 17d presents two distinct T_h populations at 240-260 °C and 180-200 °C with constant salinity (trail 3), while the trail 1 shows a continuous clustering and forms a negative correlation between T_h and salinity. Considering both trails 1 and 3 together, the trending suggests a heterogeneous mixing trajectory. Fig. 17e exhibits a constant T_h value at ~250 °C and a subtle salinity variation (2.5-5.5 wt.% NaCl eq.), which could indicate a slightly heterogeneous fluid-rock interaction. The small dispersion in the direction of lower T_h values suggest pressure fluctuations (trail 1, sample IM-4-V7).

Fig. 17f shows three trails, 1, 2, and 3 (sample IM-3-E2) composed by aqueous (Aq) and aqueous-carbonic (AqC) inclusions. The trail 3 is only constituted by AqC fluids with T_h within 340-360 °C and salinity of 14-17 wt.% NaCl eq. The trail 2 displays a clustering of AqC and Aq fluids with T_h values slightly dispersed spanning 250-300 °C and low salinity of 2-5 wt.% NaCl eq. The trail 1 shows a full mixing path among the trails 2 and 3. Therefore, we interpret that the trail 2 corresponds a final mixing product where the Aq fluids were heated and

concomitantly increased the salinity contents, while the trail 3 represents a more primitive AqC fluids prior to mixing, which was cooled and decreased their salinity, almost reaching equilibrium conditions.

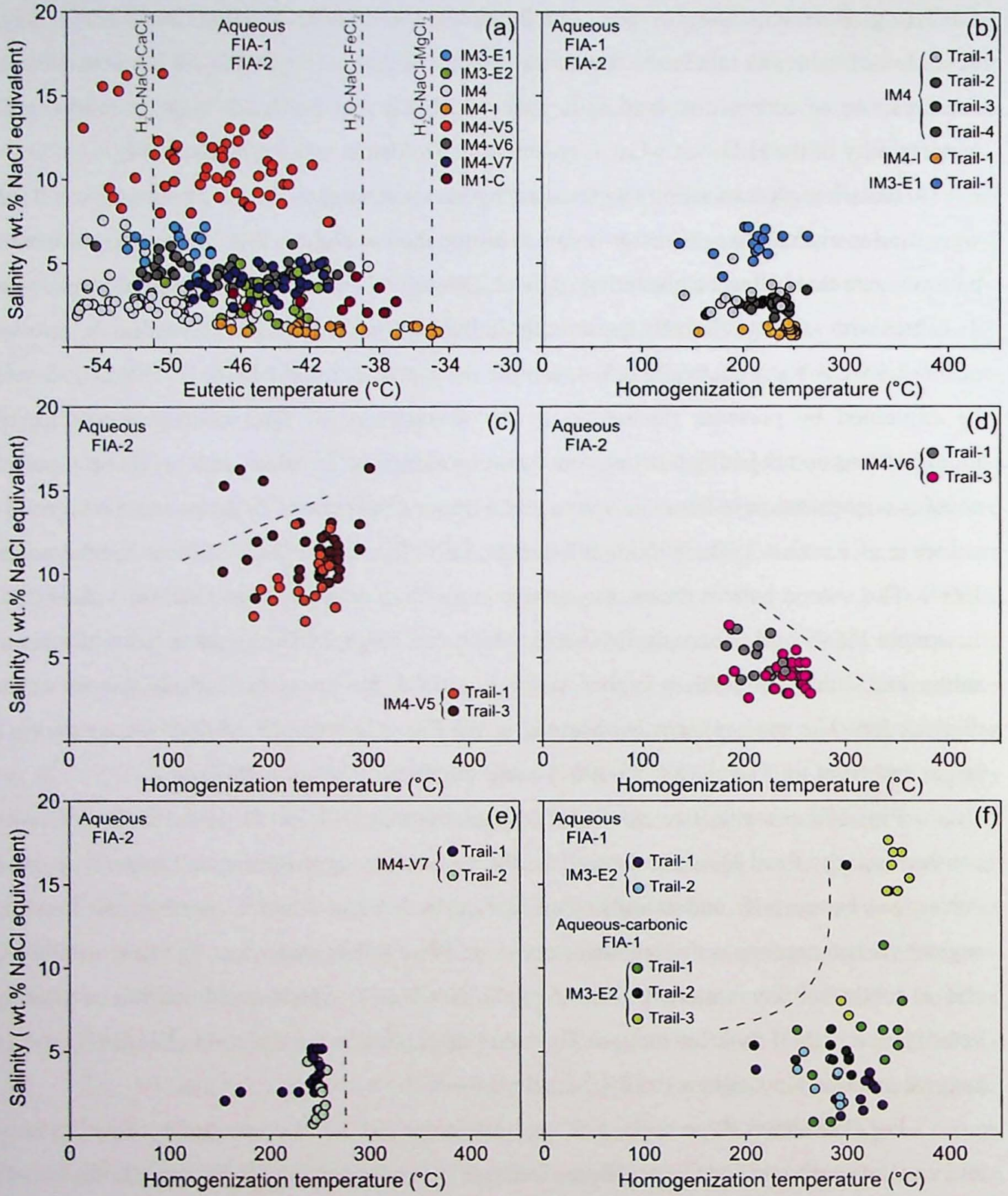

Fig. 17. Plots of salinity against eutectic (a) and homogenization (b-f) temperatures of aqueous and aqueous-carbonic inclusions (FIA 1 and 2).

4.6.3 P-T conditions during fluid entrapment

Fluid inclusions isochores were calculated based on equations by Duan et al. (1992a, b)

for CO_2-rich inclusions, and Zhang and Frantz (1987) for aqueous inclusions, using the ISOC software (Bakker, 2003). Estimations of lithostatic and hydrostatic pressure gradients to use as reference were calculated based on possible geothermal gradients of 30 and 40 °C/km, average rock density of 2.7 g/cm³, and water density of 1.0 g/cm³.

Isochore intersections from trails of aqueous and carbonic inclusions (FIA-1, 2) within or close to the average lower T_h fields (Fig. 18a-l) provide entrapment conditions of 240 °C and 0.52-1.96 kbar (trail 1, sample IM-4); 245 °C and 0.67-1.41 kbar (trail 2, sample IM-4); 250 °C and 0.88-2.50 kbar (trail 3, sample IM-4-V6); 248 °C and 0.23-1.75 kbar (trail 1, sample IM-4-I); 252 °C and 0.52-2.14 kbar (trail 1, sample IM-4-V5); 253 °C and 0.47-1.99 kbar (trails 1, 2, sample IM-4-V7); 250 °C and 0.71-1.26 kbar (trail 2, sample IM-4-V5); 255 °C and 0.45-2.03 kbar (trail 3, sample IM-4-V5); 230 °C and 0.47-1.69 kbar (trail 1, sample IM-3-E1); 310 °C and 0.40-1.73 kbar (trail 1, sample IM-3-E2); 295 °C and 0.57-1.28 kbar (trail 2, sample IM-3-E2); 298 °C and 0.73-1.16 kbar (trail 3, sample IM-3-E2).

Most individual samples showed relevant pressure variation. Disregarding post-entrapment modifications in the FIA-1 and FIA-2, as discussed above, we concluded that this large pressure variation was resulted from pressure fluctuations at the time of fluid entrapment, during the syn-deformational stages (post-veining) and gold precipitation.

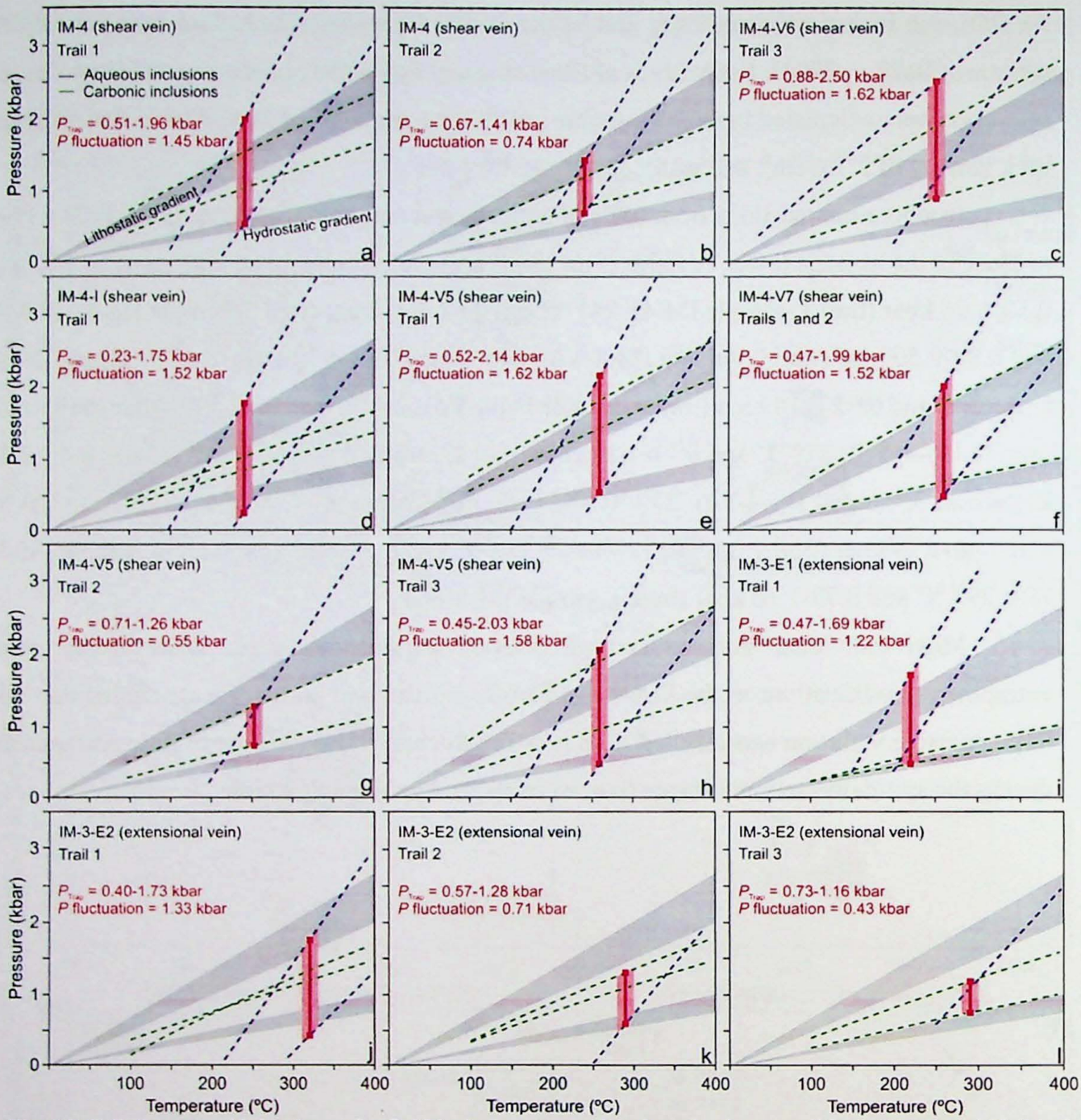

Fig. 18. P-T diagram with isochores for fluid inclusions trapped under subsolvus conditions (FIA-1 and 2). Black vertical boxes are the average lower Th values obtained from microthermometric data. Estimations of lithostatic and hydrostatic pressure gradients to use as reference were calculated based on possible geothermal gradients of 30 °C/km and 40 °C/km, average rock density of 2.7 g/cm³, and water density of 1.0 g/cm³.

CHAPTER 5 DISCUSSIONS

5.1. Fault-Valve Behavior and its Implications for Ore Genesis

Since the 1980's, extensive veining and gold mineralization in high fluid flux fault systems have been explained as a response of coupled cyclic changes in tectonic stress and fluid pressure correlated with earthquakes cycles, so-called fault-valve behavior (e.g., Cox, 1995, 1999; Sibson et al., 1988; Boullier and Robert, 1992; Robert et al., 1995; Sibson and Scott, 1998; Sibson, 2004; Faleiros et al., 2014). In such process, firstly, the fluid pressure promotes a decrease in the effective stresses leading the opening of extensional fractures inside a dilatant zone during pre-seismic periods. When fluid pressure exceeds the time-dependent fault shear strength; shear failure occurs all over the main fault zone causing a transient fracture permeability and a sudden drop in fluid pressure. As an effect, the surrounding hydrothermal fluids migrate forward to the opened fault zone and forms fault-fill or shear veins (e.g., Sibson et al., 1988). This process can repeat itself several times as fractures are sealed by mineral precipitation; only to be reopened when fluid pressure and tectonic stresses are rebuilt, initiating a new cycle (Sibson et al., 1988).

High-angle reverse fault systems are notably to be more efficient to fault-valve behavior, because they are severely misoriented for reactivation (i.e., σ_1 inclined greater than 60° to the fault planes), and therefore, frictional shear failure can only initiate when elevated fluid pressure (P_f) exceeds the minimum compressive stress (σ_3) reaching supralithostatic values (Sibson et al., 1988; Sibson, 1990. In such circumstances, several cases have been reported involving the cyclic development of extensional and fault-fill gold-bearing veins alternated with stages of ductile deformation (e.g., Boullier and Robert, 1992; Cox, 1995, 1999; Robert et al., 1995; Henderson and McCaig, 1996; Faleiros et al., 2014). Fault-valve behavior and associated veining are less pronounced along shear zone systems optimally oriented for frictional reactivation (i.e., σ_1 inclined below 30° to the fault planes) (e.g., Kolb et al., 2004; Nguyen et al., 1998). In such case, frictional reactivation of the faults occurs before fluid pressure build up to the point in which it would induce slips ($P_f < \sigma_3$) and, as a consequence, the fluid pressures never attain supralithostatic levels (Sibson et al., 1988; Sibson, 1990). Similar natural cases were described by Kolb et al. (2004) for auriferous shear zones at Hutti Gold Mine, India, and by Nguyen et al. (1998) for gold-quartz vein systems associated with shear zones at Revenge Mine, Australia. Faleiros et al. (2007) studied an intermediate case between faults favorably oriented and severely misoriented for frictional reactivation (i.e., σ_1 inclined between 40-50° to the fault surfaces), in which non-mineralized quartz vein systems were developed in the strike-

slip Ribeira Shear Zone, Southeastern Brazil (see Fig. 5a).

The Serra do Cavalo Magro gold deposit lies mainly along second-third order faults associated with the Embaúva and Forquilha Faults (Figs. 5 and 6a), which host Au-quartz shear and extensional veins. Displaced geological contacts at map scales (Figs. 5b and 6a) and shear sense indicators described at outcrops and thin section indicate dominant sinistral movements (Figs. 8e and 9e). On the other hand, the L_m stretching lineation presents a bimodal orientation distribution with subhorizontal-plunging and subvertical-plunging lineations (Fig. 6d). This pattern can be explained as evidence of (1) high-angle reverse faulting reactivation, or (2) a transpressional deformation with strain partitioning and vertical extrusion in some segments of the shear zones. The geometrical relationships between the shear zones (NE-trending vertical) and the NNW-trending vertical extensional veins (Fig. 6) suggest a paleostress regime with subhorizontal NNW-trending maximum compression (σ_1), and a subhorizontal ENE-trending least-compressive stress (σ_3) related to the transcurrent regime. On the other hand, subhorizontal extensional veins present at the Serra do Cavalo Magro deposit are evidence of a paleostress regime with horizontal σ_1 and vertical σ_3, which are compatible with high-angle reverse faulting. The subhorizontal extensional veins are also diagnostic of overpressure conditions with fluid pressure values exceeding lithostatic pressures. Thus, the available data suggest that the vein systems and shear zones at the Serra do Cavalo Magro deposit were formed in a dominant sinistral transcurrent system with episodic high-angle reverse faulting reactivation, similar to examples described for Sibson et al. (1988). The geometrical relationships between subvertical and subhorizontal extensional veins and the shear zones indicate σ_1 oriented between 55 and 85° to the fault planes, indicating that the Embaúva and Forquilha Faults were severely misoriented ($\sigma_1 > 60°$) for frictional reactivation. Microstructural relationships indicate that gold mineralization occurs primarily filling fractures in mylonitic shear veins. As associated fluid inclusions record expressive fluid pressure fluctuation, this scenario indicates alternating episodes of brittle deformation (i.e., vein opening, fracturing and fluid circulation) and ductile deformation (i.e., dynamic recrystallization, boudinage, and folding), which is diagnostic for cyclic oscillations in fluid pressure and tectonic stress during the shear zone evolution (e.g., Nguyen et al., 1998; Faleiros et al., 2007).

Fluid inclusion studies performed on faults and shear zone-hosted auriferous veins of distinct tectonic environments generally have identified pressures fluctuating between near-hydrostatic and near-lithostatic levels (e.g., Boullier and Robert, 1992; Cox, 1995; Robert et al., 1995; Faleiros et al., 2014; Wang et al., 2015; Yang et al., 2016, 2017). The most notable natural cases involving large pressure fluctuation of the order of 2.0-3.5 kbar and 0.8-1.75 kbar

have been observed in high-angle reverse faults at the Sigma Mine, Canada (Robert et al., 1995), and the Wattle Gully Mine, Australia (Cox, 1995), respectively. Faleiros et al. (2014) quantified high pressure changes of 0.4-2.2 kbar for extensional gold-quartz veins related to the Carumbé transcurrent fault zone, in the southern Ribeira Belt, Brazil. Wang et al. (2015) and Yang et al. (2016, 2017) recognized pressure variations of 0.4-2.08 kbar for disseminated and stockwork-style Au-quartz veins associated with fault systems in the Xincheng, giant Taishang, and Wang'ershan gold deposits, respectively, at Jiaodong Peninsula, China. The NE-trending Au-quartz veins present at the Serra do Cavalo Magro deposit record pressure variations of 0.4-1.6 kbar, which suggests it was developed under near-hydrostatic to supralithostatic values (Fig. 18), being compatible with a shear zone system severely misoriented for frictional reactivation.

Fluid inclusion data indicates that mineralization formed under conditions of 240-260 °C and 0.4-2.5 kbar, while petrological modeling indicates that metapelite host rocks attained peak metamorphic conditions from 560 °C and 7 kbar (chlorite-biotite phyllite) to 625 °C and 6.8 kbar (garnet-biotite phyllite). Additionally, microstructural relationships indicate that the vein-related fluids caused a retrograde overprint of the peak metamorphic assemblage, as biotite and garnet were partially to completely replaced by chlorite at the vein proximities. Thus, the gold mineralization is clearly retrograde and postdate the peak metamorphism recorded in immediate host rocks.

Janasi et al. (2001) present zircon and monazite U-Pb (ID-TIMS) ages of 610 ± 1 Ma, 605 ± 7 Ma, 604 ± 8 Ma and 601 ± 2 Ma for different lithofacies of the Agudos Grandes Suite, all of them corresponding to those that host the Au-quartz veins at the Serra do Cavalo Magro deposit. These represent the maximum ages for the gold mineralization. Available metamorphic ages for Votuverava Group rocks include a hornblende Ar-Ar age of 603 ± 7 Ma (amphibolite), inferred as the metamorphic peak age of staurolite zone grade rocks, and monazite U-Pb (LA-MC-ICP-MS) ages spanning 580-572 Ma (garnet-biotite and garnet-staurolite-biotite schists), inferred as a late metamorphic decompression event coeval with the history of the transcurrent shear zones (Yogi et al., unpublished). Available U-Pb and Ar-Ar data constrain the nucleation of the Ribeira Belt transcurrent shear zones within 610-580 Ma and low-temperature ductile activation until 540 Ma (Picanço, 2000; Faleiros et al., 2011, 2016; Passarelli et al., 2011; Dressel et al., 2018). Thus, petrological-structural relationships indicate that gold mineralization at the Serra do Cavalo Magro deposit was formed within 580-540 Ma in post-peak metamorphic episodes (Fig. 19a).

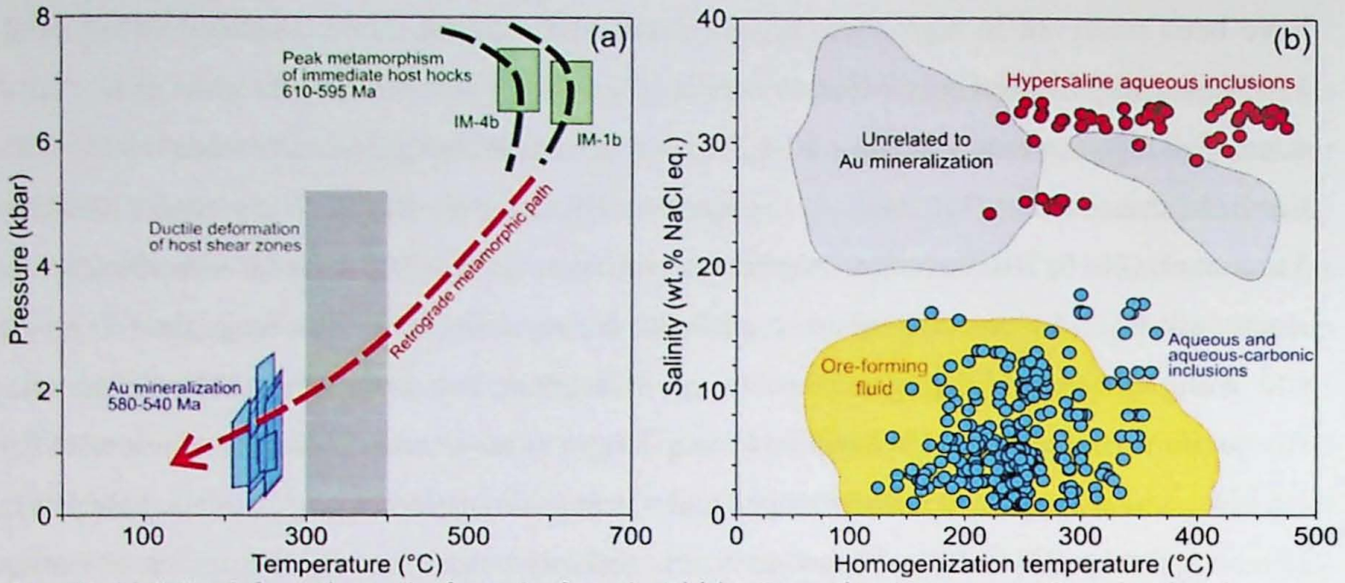

Fig. 19. (a) P-T-t-deformation paths for rocks from the Piririca Formation (Votuverava Group). Also shown are geochronological data from Faleiros et al. (2011, 2016) and Yogi et al. (unpublished). (b) Homogenization temperature-salinity pairs from aqueous and aqueous carbonic inclusions (FIA-1 and FIA-2) and hypersaline aqueous and multiphase inclusions (FIA-3) of the NE-trending Au-quartz veins at Serra do Cavalo Magro deposit. Literature data compiled in Bodnar et al. (2014) of 2733 fluid inclusions from several orogenic gold deposits. Yellow and gray shaded fields delimiting the ore-fluids and unrelated Au-fluids, respectively.

Based on the above discussions, Au-quartz veins of the Serra do Cavalo Magro deposit fulfills all of the predicted conditions for the fault-valve activity (e.g., Cox, 1995, 1999; Sibson et al., 1988). Therefore, we proposed a descriptive-genetic model, where the Au-quartz veins were formed by successive small increments (crack-seal mechanism) (Ramsay, 1980) as a response to the seismic faulting processes (Sibson et al., 1988) coeval with alternated periods of brittle and ductile deformation along the evolution of the Embaúva and Forquilha Faults and subsidiary shear zones. Gold mineralization is intimately linked to syn-deformational stages (post-veining), once microfractures and shear fractures in almost all quartz veins are filled not just by gold, but also silver, native Cu-Sn alloy, galena, pyrite, chalcopyrite, magnetite and hematite. The seismically-introduced hydrothermal fluids in these auriferous veins present highly contrasting compositions, which suggest that fluids from distinct sources were drained to the mineralized area, as will be discussed below.

5.2 Sources of Fluids in Orogenic Gold Deposits: Fluid Inclusion Evidence

Debates regarding the sources of ore-forming fluids in orogenic gold deposits have been a long-standing issue and yet is not well-understood (e.g., McCuaig and Kerrich, 1998; Ridley and Diamond, 2000; Goldfarb et al., 2005; Pitcairn et al., 2006; Phillips and Powell, 2009, 2010; Tomkins, 2013; Goldfarb and Groves, 2015; Fusswinkel et al., 2017). Over the past decades, a model based on fluids derived from metamorphic devolatilization of volcano-sedimentary rocks (e.g., McCuaig and Kerrich, 1998; Pettke et al., 1999, 2000, Pitcairn et al., 2006, 2014, Phillips

and Powell, 2009, 2010; Yardley and Cleverley, 2013) has gained larger approval, in part as a result of several careful fluid inclusion studies (e.g., Ridley and Diamond, 2000; Bodnar et al., 2014; Garofalo et al., 2014; Rauchenstein-Martinek et al., 2014; Fusswinkel et al., 2017). However, "mixed source" of deep-seated metamorphic fluids and magmatic fluids have been proposed in some orogenic gold deposits (e.g., Rogers et al., 2013; Shen et al., 2016; Mishra et al., 2018; Sahoo et al., 2018).

Despite these issues, the fluid inclusion assemblages (FIAs) mainly of quartz veins from many orogenic gold deposits are relatively consistent ore-forming fluids formed by H_2O-NaCl-$CO_2 \pm CH_4 \pm N_2$ system (e.g., Ridley and Diamond, 2000; Bodnar et al., 2014; Garofalo et al., 2014), which is probably characteristic of a single main-fluid source (e.g., Goldfarb and Groves, 2015). Ridley and Diamond (2000) argued that it is hard to discern between metamorphic fluids or magmatic fluids signatures based merely on fluid inclusion investigations, once the ore-fluids traveled for long pathways across the crust from source until come to the deposition region. For this reason, fluid geochemistry should not be expected to indicate the original source, but rather to reflect fluid-rock interactions or mixed signature of the sources (Ridley and Diamond, 2000).

Nevertheless, Fusswinkel et al. (2017) performed major and trace element measurement by LA-ICP-MS for individual fluid inclusions in auriferous veins from the Pampalo orogenic gold deposit, Eastern Finland. Mass balance calculations using metal concentrations and Cl/Br ratios suggest that the Au-rich fluid was derived purely by the metamorphic devolatilization process without any substantial magmatic-hydrothermal fluid contribution (Fusswinkel et al., 2017).

Bodnar et al. (2014) have compiled compositional and microthermometric fluid inclusion data from approximately 140 orogenic gold deposits, which allowed defining the main characteristics of the ore-forming fluids. In summary, homogenization temperatures (T_h) of aqueous-carbonic and aqueous inclusions range primarily from 150 to 300°C. CO_2-rich (carbonic) inclusions with little or without H_2O displayed a broad T_hCO_2 interval between -50 and +30°C. Salinities of aqueous inclusions vary within 0-10 wt.% NaCl equivalent, although hypersaline and multiphase fluids may be present up to about 40 wt.% NaCl equivalent (e.g., Bodnar et al., 2014). In most cases, halite-bearing inclusions are accepted to be derived from a saline groundwater source and are unrelated to Au mineralization (Robert et al., 1995). These fluids usually show low T_h varying from <100°C up to about 200°C (Robert and Kelly, 1987). On the other hand, Faleiros et al. (2014) have been described halite-bearing inclusions with high T_h values (up to 400°C), which was interpreted to carry a magmatic signature and likely related to ore formation.

Under these circumstances, FIA-1 and FIA-2 of the NE-trending Au-quartz veins from the Serra do Cavalo Magro deposit are partially consistent with a metamorphic fluid source (low-salinity aqueous fluids and CO_2-N_2-bearing fluids with or without H_2O) and gather all the main features of several orogenic gold deposits (Fig. 19b), although some exceptions may occur. The FIA-3, conversely, suggests a magmatic fluid origin represented by hypersaline and solid-multiphase inclusions of high temperatures (Fig. 19b). As Au-quartz veins were formed after-metamorphic peak of immediate host rocks we argued that the ore-forming fluids were produced by devolatilization reactions during prograde metamorphism at depth levels and moved up into sinistral transcurrent shear zone systems into rocks that have been metamorphosed and devolatilized at earlier times, as demonstrated by the deep-later model of Stüwe, (1998). The long-lived activity of the shear zone systems favored the seismic pumping (e.g., Sibson et al. 1988) of metamorphic fluids from great depths to shallow crustal levels and and perhaps allowed their mixing with magmatic fluids unrelated with gold mineralization.

As consequence to the fault-valve activity (Sibson et al., 1988), the mechanisms of Au precipitation in orogenic gold deposits has been related to fluid immiscibility (e.g., Robert and Kelly, 1987; Boullier and Robert, 1992; Craw, 1992; Dugdale and Hagemann, 2001; Coulibaly et al., 2008; Zoheir and Moritz, 2014; Wang et al., 2015; Sun et al., 2016; Yang et al., 2017), and in rarer cases, to coupled fluid immiscibility and fluid mixing (e.g., Anderson et al., 1992; Faleiros et al., 2014). Fluid inclusion data collected from NE-trending Au-quartz veins of the Serra do Cavalo Magro deposit provides robust evidence that the fluid immiscibility acted favoring Au precipitation. There is evidence for restricted fluid mixing (Fig. 17f), but this but this process is considered as unrelated with gold mineralization.

5.3 Fluid Immiscibility, Fluid Mixing, and Their Role in Au-Precipitation

The gold deposition mechanisms from hydrothermal solutions always involve changing in the physicochemical properties of the fluid at the site of ore deposition. According to (Mikucki, 1998), most of the Archean lode-gold deposits studies have been invoked changes in ore-fluid chemistry, pressure and/or temperature, in which can be resulted from many geological processes, including: (1) the adiabatic and conductive cooling of the ore-fluids; (2) the interaction between ore-fluids and their immediate host rocks; (3) phase separation in response to pressure decreases during the rise or throttling of the ore-fluid; or (4) by the mixing of two or more different fluids. Disregarding the first two processes, phase separation (i.e., fluid immiscibility) is often attributed as the most important and effective cause of Au-precipitation in several orogenic gold deposits (e.g., Robert and Kelly, 1987; Boullier and Robert, 1992;

Craw, 1992; Dugdale and Hagemann, 2001; Coulibaly et al., 2008; Zoheir and Moritz, 2014; Wang et al., 2015; Sun et al., 2016; Yang et al., 2017). In such mechanism, Au-precipitation will occur only if environmental conditions were below those of the solvus for the fluid compositions in question (e.g., Mikucki, 1998). Therefore, three factors may satisfy this condition: (1) advection of the fluid to higher crustal levels (e.g., Spooner et al., 1985); (2) catastrophic drop in P_{fluid} due to fault-valve activity (e.g., Cox, 1995; Robert et al., 1995; Dugdale and Hagemann, 2001; Faleiros et al., 2014); or (3) by expansion of the solvus due to the fluid and graphitic host rocks interaction; or mixing with CH_4-rich fluids (e.g., Naden and Shepherd, 1989).

Mikucki (1998) argued that fluid immiscibility process will depend on the initial fluid compositions and both magnitude and relative rates at which pH, sulphur content ($m\sum s$), fO_2, and temperature vary during the Au precipitation event. According to these authors, only the change in ($m\sum s$) via phase separation will favor the gold precipitation, whereas heat loss, increase in fO_2 and pH along the initial stage of separation will act to inhibit the Au precipitation. Regarding these factors, it is almost a consensus that Au is transported as sulfide (AuHS, $Au(HS)_2^-$) or chloride ($AuCl_2^-$) complexes in hydrothermal fluids (e.g., Seward, 1973; Shenberger and Barnes, 1989; Benning and Seward, 1996; Pokrovski et al., 2014, 2015). The sulfide complexes may attain Au concentrations higher than 1ppm, in H_2S neutral-alkaline (pH > 6-7) solutions at maximum temperatures of 300ºC, while the $AuCl_2^-$ complex support to Au solubility in acidic, chloride-rich, and oxidizing solutions above 300ºC (e.g., Seward, 1973; Benning and Seward 1996; Pokrovski et al., 2014, 2015).

The FIA-1 and FIA-2 entrapped under subsolvus conditions occur in all the analyzed NE-trending Au-quartz veins from the Serra do Cavalo Magro deposit. The presence of Au within microcracks and shear fractures of these veins indicated that gold precipitation was coeval with brittle-ductile stages during the shear zones evolution. The cyclic decompression of the metamorphic-hydrothermal fluids, due to seismic processes along these shear zones, triggered fluid immiscibility and subsequently lowering the Au solubility (e.g., Dugdale and Hageman, 2001).

It is difficult to say precisely whether sulfide or chloride complexes were important for carrying gold trough hydrothermal solutions, and more studies on this subject are required. Nevertheless, based on merely ore-fluid P-T conditions and compositions from NE-trending Au-quartz veins it is possible to suppose that the AuHS and $Au(HS)_2^-$ complexes maybe were responsible to carry gold.

As recognized in some natural cases (e.g., Anderson et al., 1992; Faleiros et al., 2014),

the seismic faulting processes plays a key role in the fluid dynamics during gold mineralization as a response to cyclic pressure variations, and therefore, may influence the action of coupled fluid immiscibility and mixing mechanisms. According to Faleiros et al. (2014), the sudden decrease in fluid pressure after-failure can induce the mixing of fluids of highly contrasting salinities from distinct sources, which is a critical condition for Au precipitation. In case of the Serra do Cavalo Magro deposit, we have robust fluid inclusion evidence of the involvement of fluid immiscibility in Au precipitation and partial fluid mixing unrelated to ore-formation (FIA-1 and FIA-2).

CHAPTER 6 CONCLUSIONS

The analysis of the NE-trending Au-quartz shear and extensional veins from the Serra do Cavalo Magro deposit in southern Ribeira Belt (Brazil) provides qualitative and quantitative evidences for the fault-valve behavior, as demonstrated by the petrological-structural and fluid inclusion data. These Au-quartz veins were formed at conditions of 240-260 °C and 0.4-2.5 kbar after metamorphic peak (560-625 °C and 6.8-7 kbar). The Embaúva and Forquilha Faults and its subsidiary shear zones were activated coeval to late in time to the emplacement of granitic rocks from the Agudos Grandes Suite (610-600 Ma).

Field geology and structural data strongly suggest that the Au mineralization in the Serra do Cavalo Magro deposit has been controlled primarily by sinistral transcurrent shear zones. The geometrical relationships between extensional veins and the shear zones indicate a case of faults severely misoriented (angle between σ_1 and fault planes between 55 and 85°) for frictional reactivation. In such context, the auriferous quartz veins were formed by successive crack-seal increments due to seismic faulting processes coeval with alternating stages of brittle and ductile deformation. Gold mineralization is attributed to syn-deformational stages (post-veining).

The NE-trending Au-quartz shear and extensional veins present three fluid inclusion assemblages (FIA-1, FIA-2, and FIA-3). The FIA-1 and FIA-2 are composed of carbonic (CO_2-N_2), low-intermediate salinity aqueous (H_2O-NaCl-$CaCl_2$) and aqueous-carbonic (H_2O-NaCl-$CaCl_2$-CO_2-N_2) inclusions directly related to the Au mineralization. P-T entrapment conditions (240-260 °C and 0.4-2.5 kbar) suggest that these veins were formed under near-hydrostatic to supralithostatic values. The FIA-3 represents a distinct or posterior event of high-salinity H_2O-NaCl-$CaCl_2$-KCl fluid percolation dissociated from the ore-formation.

The hydrothermal gold-rich fluids were likely produced and released by devolatilization processes during prograde metamorphism at depth and moved up along transcurrent shear zones into rocks that have been metamorphosed and devolatilized at earlier times. The gold precipitation is attributed to fluid immiscibility process, as a consequence of cyclic fluctuations in the fluid pressure and tectonic stresses linked to episodes of fault-valve activity.

BIBLIOGRAPHIC REFERENCES

Addas, W., Alegri, V., Francisconi, O., and Bezerra, J.R.L., 1985, Projeto Banespa Mineração Serra do Cavalo Magro. CPRM: Relatório final - Etapa 1.

Addas, W., and Vinha, C.A.G., 1975, Projeto SUDELPA. CPRM: Relatório final de reconhecimento geoquímico, parte 1.

Almeida, F.F.M., Hasui, Y., Brito Neves, B.B., and Fuck, R.A., 1981, Brazilian structural provinces: An introduction: Earth-Science Reviews, v. 17, p. 1-29, doi:10.1016/0012-8252(81)90003-9.

Almeida, F.F.M., Hasui, Y., Brito Neves, B.B., and Fuck, R.A., 1977, Provínvias Estruturais Brasileiras, *in* Atas do VIII Simpósio de Geologia do Nordeste, p. 363-391.

Andersen, T., Austrheim, H., Burke, E.A.J., and Elvevold, S., 1993, N_2 and CO_2 in deep crustal fluids: evidence from the Caledonides of Norway: Chemical Geology, v. 108, p. 113-132.

Anderson, M.R., Rankin, A.H., and Spiro, B., 1992, Fluid mixing in the generation of mesothermal gold mineralisation in the Transvaal Sequence, Transvaal, South Africa: European journal of mineralogy, v. 4, p. 933-948, doi:10.1016/j.addr.2006.09.008.

Archer, D.G., 1992, Thermodynamic Properties of the NaCl + H_2O System. II. Thermodynamic Properties of NaCl (aq), NaCl2H2O (cr), and Phase Equilibria: J. Phys. and Chem. Ref. Data, v. 21, p. 793-829, doi:10.1056.

Augustin, J., and Gaboury, D., 2019, Multi-stage and multi-sourced fluid and gold in the formation of orogenic gold deposits in the world-class Mana district of Burkina Faso - Revealed by LA-ICP-MS analysis of pyrites and arsenopyrites: Ore Geology Reviews, v. 104, p. 495-521, doi:10.1016/j.oregeorev.2018.11.011.

Bakker, R.J., 1997, Clathrates: Computer programs to calculate fluid inclusion V-X properties using clathrate melting temperatures: Computers and Geosciences, v. 23, p. 1-18, doi:10.1016/S0098-3004(96)00073-8.

Bakker, R.J., 2003, Package FLUIDS 1. Computer programs for analysis of fluid inclusion data and for modelling bulk fluid properties: Chemical Geology, v. 194, p. 3-23.

Bakker, R.J., and Jansen, B.H., 1990, Preferential water leakage from fluid inclusions by means of mobile dislocations: Letters to Nature, v. 345, p. 58-60.

Bath, A.B. et al., 2013, Biotite and apatite as tools for tracking pathways of oxidized fluids in the Archean East Repulse gold deposit, Australia: Economic Geology, v. 108, p. 667-690, doi:https://doi.org/10.2113/econgeo.108.4.667.

Benning, L.G., and Seward, T.M., 1996, Hydrosulphide complexing of Au(I) in hydrothermal solutions from 150-400°C and 500-1500 bar: Geochimica et Cosmochimica Acta, v. 60, p. 1849-1871.

Bierlein, F.P., Christie, A.B., and Smith, P.K., 2004, A comparison of orogenic gold mineralisation in central Victoria (AUS), western South Island (NZ) and Nova Scotia (CAN): implications for variations in the endowment of Palaeozoic metamorphic terrains: Ore Geology Reviews, v. 25, p. 125-168, doi:10.1016/j.oregeorev.2003.09.002.

Blenkinsop, T., 2000, Deformation microstructures and mechanisms in minerals and rocks: Kluwer Academic Publishers, 133 p.

Bodnar, R.J., Lecumberri-Sanchez, P., Moncada, D., and Steele-MacInnis, M., 2014, Fluid inclusions in hydrothermal ore deposits: Elsevier Ltd., v. 13, 119-142 p., doi:10.1016/B978-

0-08-095975-7.01105-0.

Borin Junior, T., and Ferrari, C.P., 1986, Projeto Pilões. CPRM: Relatório final de pesquisa.

Boullier, A., and Robert, F., 1992, Palaeoseismic events recorded in Archaean gold-quartz vein networks, Val d'Or, Abitibi, Quebec, Canada: Journal of Structural Geology, v. 14, p. 161-179, doi:10.1016/0191-8141(92)90054-Z.

Bowers, T.S., and Helgeson, H.C., 1983, Calculation of the thermodynamic and geochemical consequences of nonideal mixing in the system H_2O-CO_2-NaCl on phase relations in geologic systems: metamorphic equilibria at high pressures and temperatures.: American Mineralogist, v. 68, p. 1059-1075, doi:10.1016/0016-7037(83)90066-2.

Brito Neves, B.B., Campos Neto, M.C., and Fuck, R.A., 1999, From Rodinia to western Gondwana; an approach to the Brasiliano-Pan African cycle and orogenic collage: Episodes, v. 22, p. 155-166, doi:10.1016/j.precamres.2007.04.018.

Bucher, K., and Grapes, R., 2011, Petrogenesis of metamorphic rocks: Springer, 419 p., doi:10.1007/978-3-540-74169-5.

Burke, E.A.J., 2001, Raman microspectrometry of fluid inclusions: Lithos, v. 55, p. 139-158, doi:10.1016/S0024-4937(00)00043-8.

Burrows, D.R., Wodd, P.C., and Spooner, E.T.C., 1986, Carbon isotope evidence for a magmatic origin for Archaean gold-quartz vein ore deposits: Nature, v. 321, p. 851-854.

Câmara, M.M., 1992, Classificação tipológica das principais mineralizações auríferas primárias do Vale do Ribeira, SP, *in* Boletim de Resumos Expandidos do 37º Congresso Brasileiro de Geologia, v.1, São Paulo, SBG, p. 236-237.

Cameron, E.M., 1988, Archean gold: Relation to granulite formation and redox zoning in the crust: Geology, v. 16, p. 109-112.

Campanha, G.A.C., 1991, Tectônica proterozóica no alto e médio Vale do Ribeira, Estados de São Paulo e Paraná: Tese de Doutorado. Universidade de São Paulo, 296 p.

Campanha, G.A.C., Basei, M.S., Faleiros, F.M., and Nutman, A.P., 2016, The Mesoproterozoic to early Neoproterozoic passive margin Lajeado Group and Apiaí Gabbro, Southeastern Brazil: Geoscience Frontiers, v. 7, p. 683-694, doi:10.1016/j.gsf.2015.08.004.

Campanha, G.A.C., Basei, M.A.S., Tassinari, C.C.G., Nutman, A.P., and Faleiros, F.M., 2008, Constraining the age of the Iporanga Formation with SHRIMP U-Pb zircon: Implications for possible Ediacaran glaciation in the Ribeira Belt, SE Brazil: Gondwana Research, v. 13, p. 117-125, doi:10.1016/j.gr.2007.05.010.

Campanha, G.A.C., and Brito Neves, B.B., 2004, Frontal and oblique tectonics in the Brazilian Shield: Episodes, v. 27, p. 255-259, doi:10.1016/S1342-937X(05)70391-9.

Campanha, G.A.C., Faleiros, F.M., Basei, M.A.S., Tassinari, C.C.G., Nutman, A.P., and Vasconcelos, P.M., 2015, Geochemistry and age of mafic rocks from the Votuverava Group, southern Ribeira Belt, Brazil: Evidence for 1490Ma oceanic back-arc magmatism: Precambrian Research, v. 266, p. 530–550, doi:10.1016/j.precamres.2015.05.026.

Campanha, G.A.C., Faleiros, F.M., Cawood, P.A., Cabrita, D.I.G., Ribeiro, B. V., and Basei, M.A.S., 2019, The Tonian Embu Complex in the Ribeira Belt (Brazil): revision, depositional age and setting in Rodinia and West Gondwana: Precambrian Research, v. 320, p. 31-45, doi:10.1016/j.precamres.2018.10.010.

Campanha, G.A.C., and Sadowski, G.R., 1999, Tectonics of the southern portion of the Ribeira

Belt (Apiai Domain): Precambrian Research, v. 98, p. 31-51, doi:10.1016/S0301-9268(99)00027-3.

Cawood, P.A., and Hawkesworth, C.J., 2015, Temporal relations between mineral deposits and global tectonic cycles, *in* Jenkin, G.R.T., Lusty, P.A.J., McDonald, I., Smith, M.P., Boyce, A.J., and Wilkinson, J.J. eds., Ore deposits in an evolving earth, Geological Society, London, Special Publications, 393, p. 9-21, doi:http://dx.doi.org/10.1144/SP393.1.

Chiodi Filho, C., Takahashi, A.T., Silva, C.R., and Ferreira, J.C.G., 1983, Projeto Capão Bonito. CPRM: Relatório final.

Connolly, J.A.D., 2005, Computation of phase equilibria by linear programming: A tool for geodynamic modeling and its application to subduction zone decarbonation: Earth and Planetary Science Letters, v. 236, p. 524-541, doi:10.1016/j.epsl.2005.04.033.

Coulibaly, Y., Boiron, M.C., Cathelineau, M., and Kouamelan, A.N., 2008, Fluid immiscibility and gold deposition in the Birimian quartz veins of the Angovia deposit (Yaouré, Ivory Coast): Journal of African Earth Sciences, v. 50, p. 234-254, doi:10.1016/j.jafrearsci.2007.09.014.

Cox, S.F., 1999, Deformational controls on the dynamics of fluid flow in mesothermal gold systems: Geological Society, London, Special Publications, v. 155, p. 123-140, doi:10.1144/GSL.SP.1999.155.01.10.

Cox, S.F., 1995, Faulting processes at high fluid pressures: An example of fault valve behavior from the Wattle Gully Fault, Victoria, Australia: Journal of Geophysical Research, v. 100, p. 12,841-12,859.

Cox, S.F., Etheridge, M.A., and Wall, V.J., 1987, The role of fluids in syntectonic mass transport, and the localization of metamorphic vein-type ore deposists: Ore Geology Reviews, v. 2, p. 65-86, doi:10.1016/0169-1368(87)90024-2.

Cox, S.F., Wall, V.J., Etheridge, M.A., and Potter, T.F., 1991, Deformational and metamorphic processes in the formation of mesothermal vein-hosted gold deposits - examples from the Lachlan Fold Belt in central Victoria, Australia: Ore Geology Reviews, v. 6, p. 391-423, doi:10.1016/0169-1368(91)90038-9.

Craw, D., 1992, Fluid evolution, fluid immiscibility and gold deposition during Cretaceous-Recent tectonics and uplift of the Otago and Alpine Schist, New Zealand: Chemical Geology, v. 98, p. 221-236, doi:10.1016/0009-2541(92)90186-9.

Crawford, M.L., and Hollister, S., 1986, Metamorphic fluids : the evidence from fluid inclusions: Fluid-rock interactions during metamorphism. Advances in Physical Geochemistry, p. 1-35, doi:10.1007/978-1-4612-4896-5_1.

Cury, L.F., Kaulfuss, G.A., Siga Jr, O., Angelo, M., Basei, M.A.S., Harara, O.M., and Sato, K., 2002, Idades U-Pb (zircões) de 1.75 Ga em granitóides alcalinos deformados dos núcleos Betara e Tigre: Evidências de regimes extensionais do Estateriano na Faixa Apiaí: Revista do Instituto de Geociências, v. 2, p. 95-108.

Dressel, B.C., Chauvet, A., Trzaskos, B., Biondi, J.C., Bruguier, O., Monié, P., Villanova, S.N., and Newton, J.B., 2018, The Passa Três lode gold deposit (Paraná State, Brazil): An example of structurally-controlled mineralisation formed during magmatic- hydrothermal transition and hosted within granite: Ore Geology Reviews, v. 102, p. 701-727, doi:10.1016/j.oregeorev.2018.09.007.

Drews, M.G.P., and Vasconcelos, C.S., 1992, Levantamento geofísico para prospecção de ouro e sulfetos no Vale do Ribeira - SP.

Duan, Z., Moller, N., and Weare, J.H., 1992a, An equation of state for the CH_4-CO_2-H_2O system: II. Mixtures from 50 to 1000°C and 0 to 1000 bar: Geochimica et Cosmochimica Acta, v. 56, p. 2619-2631.

Duan, Z., Møller, N., and Weare, J.H., 1992b, An equation of state for the CH_4-CO_2-H_2O system: I. Pure systems from 0 to 1000°C and 0 to 8000 bar: Geochimica et Cosmochimica Acta, v. 56, p. 2605–2617, doi:10.1016/0016-7037(92)90347-L.

Dugdale, A.L., and Hagemann, S.G., 2001, The Bronzewing lode-gold deposit, Western Australia: P-T-X evidence for fluid immiscibility caused by cyclic decompression in gold-bearing quartz-veins: Chemical Geology, v. 173, p. 59-90, doi:10.1016/S0009-2541(00)00268-0.

Duschek, W., Kleinrahm, R., and Wagner, W., 1990, Measurement and correlation of the (pressure, density, temperature) relation of carbon dioxide. I. The homogeneous gas and liquid regions in the temperature range from 217 K to 340 at pressures up to 9 MPa: J. Chem. Thermodynamics, v. 22, p. 827-840.

Faleiros, F.M., 2008, Evolução de terrenos tectono-metamórficos da Serrania do Ribeira e Planalto Alto Turvo (SP, PR): Tese de Doutorado. Universidade de São Paulo, 306 p.

Faleiros, F.M., 2003, Zona de Cisalhamento Ribeira: deformação, metamorfismo e termobarometria de veios Sin-tectônicos: Dissertação de Mestrado. Universidade de São Paulo, 142 p.

Faleiros, F.M., Campanha, G.A.C., Bello, R.M.S., and Fuzikawa, K., 2007, Fault-valve action and vein development during strike-slip faulting: An example from the Ribeira Shear Zone, Southeastern Brazil: Tectonophysics, v. 438, p. 1-32, doi:10.1016/j.tecto.2007.03.004.

Faleiros, F.M., Campanha, G.A.C., Bello, R.M.S., and Fuzikawa, K., 2010, Quartz recrystallization regimes, c-axis texture transitions and fluid inclusion reequilibration in a prograde greenschist to amphibolite facies mylonite zone (Ribeira Shear Zone, SE Brazil): Tectonophysics, v. 485, p. 193-214, doi:10.1016/j.tecto.2009.12.014.

Faleiros, A.M., Campanha, G.A.C., Faleiros, F.M., and Bello, R.M.S., 2014, Fluid regimes, fault-valve behavior and formation of gold-quartz veins - The Morro do Ouro Mine, Ribeira Belt, Brazil: Ore Geology Reviews, v. 56, p. 442-456, doi:10.1016/j.oregeorev.2013.05.002.

Faleiros, F.M., Campanha, G.A.C., Martins, L., Vlach, S.R.F., and Vasconcelos, P.M., 2011a, Ediacaran high-pressure collision metamorphism and tectonics of the southern Ribeira Belt (SE Brazil): Evidence for terrane accretion and dispersion during Gondwana assembly: Precambrian Research, v. 189, p. 263-291, doi:10.1016/j.precamres.2011.07.013.

Faleiros, F.M., Campanha, G.A.C., Pavan, M., Almeida, V. V., Rodrigues, S.W.O., and Araújo, B.P., 2016, Short-lived polyphase deformation during crustal thickening and exhumation of a collisional orogen (Ribeira Belt, Brazil): Journal of Structural Geology, v. 93, p. 106-130, doi:10.1016/j.jsg.2016.10.006.

Faleiros, F.M., Ferrari, V.C., Costa, V.S., and Campanha, G.A.C., 2011b, Geoquímica e petrogênese de metabasitos do Grupo Votuverava (Terreno Apiaí, Cinturão Ribeira Meridional): Evidências de uma bacia retroarco calimiana: Geologia USP - Serie Cientifica, v. 11, p. 135-155.

Faleiros, F.M., Morais, S.M., and Costa, V.S., 2012, Geologia e Recurso Minerais da Folha Apiaí SG. 22-X-B-V.

Faleiros, F.M., and Pavan, M., 2013, Geologia e Recursos Minerais da Folha Eldorado Paulista SG.22-X-B-VI.

Fleuty, M.J., 1964, The description of folds: Proceedings of the Geologists's Association, v. 75, p. 461-492, doi:10.1016/S0016-7878(64)80023-7.

Fuhrman, M.L., and Lindsley, D.H., 1988, Ternary-feldspar modeling and thermometry: American Mineralogist, v. 73, p. 201-215, doi:10.4052/tigg.24.13.

Fusswinkel, T., Wagner, T., and Sakellaris, G., 2017, Fluid evolution of the Neoarchean Pampalo orogenic gold deposit (E Finland): Constraints from LA-ICPMS fluid inclusion microanalysis Tobias: Chemical Geology, v. 450, p. 96-121, doi:10.1016/j.chemgeo.2016.12.022.

Gao, S., Xu, H., Quan, S., Zang, Y., and Wang, T., 2018, Geology, hydrothermal fluids, H-O-S-Pb isotopes, and Rb-Sr geochronology of the Daxintun orogenic gold deposit in Heilongjiang province, NE China: Ore Geology Reviews, v. 92, p. 569-587, doi:10.1016/j.oregeorev.2017.11.014.

Garofalo, P.S., Fricker, M.B., Gunnther, D., Bersani, D., and Lottici, P.P., 2014, Physical-chemical properties and metal budget of Au-transporting hydrothermal fluids in orogenic deposits, *in* Garofalo, P.S. and Ridley, J.R. eds., Gold-Transporting Hydrothermal Fluids in the Earth's Crust, Geological Society, London, Special Publications, 402, p. 71-102.

Garrabos, Y., Tufeu, R., Le Neindre, B., Zalczer, G., and Beysens, D., 1980, Rayleigh and Raman scattering near the critical point of carbon dioxide: The Journal of Chemical Physics, v. 72, p. 4637-4651, doi:10.1063/1.439706.

Goldfarb, R.J., Baker, T., Dubé, B., Groves, D.I., Hart, C.J.R., and Gosselin, P., 2005, Distribution, character, and genesis of gold deposits in metamorphic terranes: Economic Geology 100th Anniversary Volume, v. 100, p. 407-450.

Goldfarb, R.J., and Groves, D.I., 2015, Orogenic gold: Common or evolving fluid and metal sources through time: Lithos, v. 233, p. 2-26.

Goldfarb, R.J., Groves, D.I., and Gardoll, S.J., 2001, Orogenic gold and geologic time: A global synthesis: Ore Geology Reviews, v. 18, p. 1-75.

Goldfarb, R.J., Leach, D.L., Pickthom, W.J., and Paterson, C.J., 1988, Origin of lode-gold deposits of the Juneau gold belt , southeastern Alaska: Geology, v. 16, p. 440-443, doi:https://doi.org/10.1130/0091-7613(1988)016<0440:OOLGDO>2.3.CO;2.

Goldfarb, R.J., and Santosh, M., 2014, The dilemma of the Jiaodong gold deposits: Are they unique? Geoscience Frontiers, v. 5, p. 139-153.

Goldstein, R.H., and Reynolds, T.J., 1994, Systematics of fluid inclusions in diagenetic minerals: SEPM short course 31, v. 31, 199 p.

Graupner, T., Niedermann, S., Kempe, U., Klemd, R., and Bechtel, A., 2006, Origin of ore fluids in the Muruntau gold system: Constraints from noble gas, carbon isotope and halogen data Torsten: Geochimica et Cosmochimica Acta, v. 70, p. 5356-5370, doi:10.1016/j.gca.2006.08.013.

Groves, D.I., Goldfarb, R.J., Gebre-Mariam, M., Hagemann, S.G., and Robert, F., 1998, Orogenic gold deposits: a proposed classification in the context of their crustal distribution and relationship to other gold deposit types: Ore Geology Reviews, v. 13, p. 7-27, doi:10.1016/S0169-1368(97)00012-7.

Groves, D.I., Goldfarb, R.J., Knox-robinson, C.M., Ojala, J., Gardoll, S., Yun, G.Y., and Holyland, P., 2000, Late-kinematic timing of orogenic gold deposits and significance for computer-based exploration techniques with emphasis on the Yilgarn Block, Western

Australia: Ore Geology Reviews, v. 17, p. 1-38, doi:https://doi.org/10.1016/S0169-1368(00)00002-0.

Groves, D.I., Goldfarb, R.J., Robert, F., and Hart, C.J.R., 2003, Gold deposits in metamorphic belts: Overview of current understanding, outstanding problems, future research, and exploration significance: Economic Geology, v. 98, p. 1-29, doi:10.2113/gsecongeo.98.1.1.

Groves, D.I., and Santosh, M., 2016, The giant Jiaodong gold province: The key to a unified model for orogenic gold deposits? Geoscience Frontiers, v. 7, p. 409-417, doi:10.1016/j.gsf.2015.08.002.

Hackspacher, P.C., Dantas, E.L., Spoladore, A., Fetter, A.H., and Oliveira, M.A.F., 2000, Evidence of Neoproterozoic backarc basin development in the central Ribeira Belt, Southeastern Brazil: New geochronological and geochemical constraints from the São Roque - Açungui Groups: Revista Brasileira de Geociências, v. 30, p. 110-114.

Hagemann, S.G., Gebre-Mariam, M., and Groves, D.I., 1994, Surface-water influx in shallow-level Archean lode-gold deposits in Western Australia: Geology, v. 22, p. 1067-1070.

Hagemann, S.G., and Lüders, V., 2003, P-T-X conditions of hydrothermal fluids and precipitation mechanism of stibnite-gold mineralization at the Wiluna lode-gold deposits, Western Australia: Conventional and infrared microthermometric constraints: Mineralium Deposita, v. 38, p. 936-952, doi:10.1007/s00126-003-0351-6.

Heilbron, M., Cordani, U.G., and Alkimim, F.F., 2017, The São Francisco Craton and its margins (M. Heilbron, U. G. Cordani, F. F. Alkmin, Eds.): Switzerland, Springer, 331 p.

Heilbron, M., Pedrosa-Soares, A.C., Campos Neto, M.C., Silva, L.C., Trouw, R.A.J., and Janasi, V.A., 2004, Província Mantiqueira, *in* Geologia do continente sul-americano: Evolução da obra de Fernando Flávio Marques de Almeida, p. 203-234, http://segesc.paginas.ufsc.br/files/2012/05/LivroAlmeida1.pdf.

Henderson, I.H.C., and McCaig, A.M., 1996, Fluid pressure and salinity variations in shear zone-related veins, central Pyrenees, France: Implications for the fault-valve model: Tectonophysics, v. 262, p. 321-348, doi:10.1016/0040-1951(96)00018-2.

Hobbs, B.E., Means, w. D., and Willians, P.F., 1976, An outline of Structural Geology: New York, John Wiley & Sons, 571 p.

Hodgson, C.J., 1989, The structure of shear-related, vein-type gold deposits: a review: Ore Geology Reviews, v. 4, p. 231-273.

Holland, T.J.B., and Powell, R., 2011, An improved and extended internally consistent thermodynamic dataset for phases of petrological interest, involving a new equation of state for solids: Journal of Metamorphic Geology, v. 29, p. 333-383, doi:10.1111/j.1525-1314.2010.00923.x.

Hollister, L.S., 1990, Enrichment of CO2 in fluid inclusions in quartz by removal of H2O during crystal-plastic deformation: Journal of Structural Geology, v. 12, p. 895-901.

Janasi, V.A., Leite, R.J., and Van Schmus, W.R., 2001, U-Pb chronostratigraphy of the granitic magmatism in the Agudos Grandes Batholith (West of São Paulo, Brazil) - Implications for the evolution of the Ribeira Belt: Journal of South American Earth Sciences, v. 14, p. 363-376, doi:10.1016/S0895-9811(01)00034-7.

Janasi, V.A., Leite, R.J., and Ulbrich, H.H.G.J., 1994, Diversidade do magmatismo granítico tardi-brasiliano na região de Piedade, SP: Aspectos petrográficos e geoquímicos, *in* Anais do 37° Congresso Brasileiro de Geologia, Balneário Camburiú, p. 131-133.

Johnson, E.L., and Hollister, L.S., 1995, Syndeformational fluid trapping in quartz: determining the pressure-temperature conditions of deformation from fluid inclusions and the formation of pure CO_2 fluid inclusions during grain-boundary migration: Journal of Metamorphic Geology, v. 13, p. 239-249, doi:10.1111/j.1525-1314.1995.tb00216.x.

Kerkhof, A.M., 1987, The fluid evolution of the Harmsarvet ore deposit, central Sweden: Gff, v. 109, p. 1-12, doi:10.1080/11035898709454735.

Kerkhof, A.M., and Olsen, S.N., 1990, A natural example of superdense CO_2 inclusions: Microthermometry and Raman analysis: Geochimica et Cosmochimica Acta, v. 54, p. 895-901, doi:10.1016/0016-7037(90)90383-V.

Kerrich, R., 1976, Some effects of tectonic recrystallization on fluid inclusions in vein quartz.: Contributions to Mineralogy and Petrology, v. 59, p. 195-202.

Klein, E.L., 2014, Ore fluids of orogenic gold deposits of the Gurupi Belt, Brazil: a review of the physico-chemical properties, sources, and mechanisms of Au transport and deposition: Geological Society, London, Special Publications, v. 402, p. 121-145, doi:10.1144/SP402.2.

Kolb, J., Rogers, A., Meyer, F.M., and Vennemann, T.W., 2004, Development of fluid conduits in the auriferous shear zones of the Hutti Gold Mine, India: Evidence for spatially and temporally heterogeneous fluid flow: Tectonophysics, v. 378, p. 65-84, doi:10.1016/j.tecto.2003.10.009.

Lawrence, D.M., Treloar, P.J., Rankin, A.H., Boyce, A., and Harbidge, P., 2013a, A fluid inclusion and stable isotope study at the Loulo Mining District, Mali, West Africa: Implications for multifluid sources in the generation of orogenic gold deposits: Economic Geology, v. 108, p. 229-257.

Lawrence, D.M., Treloar, P.J., Rankin, A.H., Harbidge, P., and Holliday, J., 2013b, The geology and mineralogy of the Loulo Mining District, Mali, West Africa: Evidence for two distinct styles of orogenic gold mineralization: Economic Geology, v. 108, p. 199-227.

Leite, R.J., 1997, Geologia, petrografia e gequímica dos granitóides da região de Piedade, SP: Dissertação de Mestrado. Universidade de São Paulo, 158 p.

Leite, R.J., 2003, Petrogênese e geocronologia U-Pb do magmatismo granítico tardi- a pós-orogênico no Batólito Agudos Grandes (SP): Tese de Doutorado. Universidade de São Paulo.

Leite, R.J., Janasi, V.A., and Martins, L., 2006, Contamination in mafic mineral-rich calc-alkaline granites: A geochemical and Sr-Nd isotope study of the Neoproterozoic Piedade Granite, SE Brazil: Anais da Academia Brasileira de Ciencias, v. 78, p. 345-371, doi:10.1590/S0001-37652006000200013.

Li, N., Deng, J., Yang, L., Groves, D.I., Liu, X., and Dai, W., 2018, Constraints on depositional conditions and ore-fluid source for orogenic gold districts in the West Qinling Orogen, China: Implications from sulfide assemblages and their trace-element geochemistry: Ore Geology Reviews, v. 102, p. 204-219, doi:10.1016/j.oregeorev.2018.08.025.

Liu, Q., Shao, Y., Chen, M., Algeo, T.J., Li, H., Dick, J.M., Wang, C., Wang, W., Li, Z., and Liu, Z., 2019, Insights into the genesis of orogenic gold deposits from the Zhengchong gold field, northeastern Hunan Province, China: Ore Geology Reviews, v. 105, p. 337-355, doi:10.1016/j.oregeorev.2019.01.002.

Lopes Jr, I., Câmara, M.M., Vasconcelos, C.S., and Pizzatto, L.G., 1994, A Prospecção Geoquímica Descobrindo Novas Mineralizações Auríferas no Vale do Ribeira, *in* Boletim de Resumos Expandidos do 38º Congresso Brasileiro de Geologia, v.3, Camboriú, SBG, p.

170-171.

Lopes Jr, I., Câmara, M.M., Vasconcelos, C.S., and Pizzatto, L.G., 1995, Novas mineralizações auríferas no Vale do Ribeira - Um trabalho de prospecção geoquímica, *in* Boletim de Resumos do 4º Simpósio de Geologia do Sudeste, Águas de São Pedro, SBG, p. 121.

Maniesi, V., 1997, Petrologia das rochas anfibolíticas das regiões de Adrianópolis, Campo Largo e Rio Branco do Sul/PR: Tese de Doutorado: Universidade Estadual Paulista, 215 p.

Mao, J., Wang, Y., Li, H., and Pirajno, F., 2015, The relationship of mantle-derived fluids to gold metallogenesis in the Jiaodong Peninsula: Evidence from D-O-C-S isotope systematics: Ore Geology Reviews, v. 33, p. 361-381, doi:10.1016/j.oregeorev.2007.01.003.

Martins, L., 2001, Condições de cristalização de granitos sin- e tardi- orogênicos da porção central do Batólito Agudos Grandes, Sp, com base em geoquímica de minerais e rochas: Dissertação de Mestrado. Universidade de São Paulo, 127 p.

McClay, K.R., 1987, The mapping of geological structures: John Wiley & Sons, 168 p., doi:10.1180/minmag.1988.052.367.25.

McCuaig, T.C., and Kerrich, R., 1998, P-T-t-deformation-fluid characteristics of lode gold deposits : evidence from alteration systematics: Ore Geology Reviews, v. 12, p. 381-453.

Meira, V.T., García-Casco, A., Juliani, C., Almeida, R.P., and Schorscher, J.H.D., 2015, The role of intracontinental deformation in supercontinent assembly: insights from the Ribeira Belt, Southeastern Brazil (Neoproterozoic West Gondwana): Terra Nova, v. 27, p. 206-217, doi:10.1111/ter.12149.

Mikucki, E.J., 1998, Hydrothermal transport and depositional processes in Archean lode-gold systems: a review: Ore Geology Reviews, v. 13, p. 307-321, doi:10.1016/S0169-1368(97)00025-5.

Mishra, B., Pruseth, K.L., Hazarika, P., and Chinnasamy, S.S., 2018, Nature and source of the ore-forming fluids associated with orogenic gold deposits in the Dharwar Craton: Geoscience Frontiers, v. 9, p. 715-726, doi:10.1016/j.gsf.2017.09.005.

Morgental, A., Batolla Jr, F., Pinto, G.G., Paiva, I.P., and Drumond, J.B. V., 1975, Projeto SUDELPA. CPRM: Relatório final - Geologia.

Morgental, A., Borin Junior, T., Silva, A.A.G.P., Alegri, V., Oliveira, P.E.P., Machado, G.J., and Addas, W., 1978, Projeto geoquímica no Vale do Ribeira. CPRM: Relatório final.

Morgental, A., Paiva, I.P., Borin Junior, T., Pinto, G.G., and Carmo, L.S., 1981, Pesquisa de ouro no Vale do Ribeira - Atuação da CPRM, *in* Atas do 3º Simpósio Regional de Geologia, v.1, Curitiba, SBG, p. 56-70.

Mori, P.E., Reeves, S., Correia, C.T., and Haukka, M., 1999, Development of a fused glass disc XRF facility and comparison with the pressed powder pellet technique at Instituto de Geociencias, São Paulo University.: Revista Brasileira de Geociências, v. 29, p. 441-446, doi:10.5327/rbg.v29i3.715.

Naden, J., and Shepherd, T.J., 1989, Role of methane and carbon dioxide in gold deposition: Letters to Nature, v. 342, p. 793-795, doi:10.1038/340301a0.

Neumayr, P., Walshe, J., Hagemann, S., Petersen, K., Roache, A., Frikken, P., Horn, L., and Halley, S., 2008, Oxidized and reduced mineral assemblages in greenstone belt rocks of the St. Ives gold camp, Western Australia: vectors to high-grade ore bodies in Archaean gold deposits? Mineralium Deposita, v. 43, p. 363-371, doi:10.1007/s00126-007-0170-2.

Nguyen, P.T., Harris, L.B., Powell, C.M., and Cox, S.F., 1998, Fault-valve behaviour in optimally oriented shear zones: An example at the Revenge gold mine, Kambalda, Western Australia: Journal of Structural Geology, v. 20, p. 1625-1640, doi:10.1016/S0191-8141(98)00054-6.

Nogueira, S.A.A., 1990, Estudo das mineralizações filoneanas auríferas do Depósito de Piririca, Vale do Ribeira, SP: Dissertação de Mestrado. University de São Paulo, 88 p.

Paiva, I.P., and Addas, W., 1982, Projeto ouro aluvionar na área da SUDELPA, fase II. CPRM: Relatório final.

Paiva, I.P., and Morgental, A., 1980, Prospecto: Ouro nas regiões auríferas dos Agudos Grandes e Morro do Ouro, Vale do Ribeira.

Parnell, J.P. et al., 2000, Regional fluid flow and gold mineralization in the Dalradian of the Sperrin Mountains, Northern Ireland: Economic Geology, v. 95, p. 1389-1416.

Passarelli, C.R., Basei, M.A.S., Wemmer, K., Siga Jr., O., and Oyhantçabal, P., 2011, Major shear zones of southern Brazil and Uruguay: escape tectonics in the eastern border of Rio de La plata and Paranapanema cratons during the Western Gondwana amalgamation: International Journal of Earth Sciences, v. 100, p. 391-414, doi:10.1007/s00531-010-0594-2.

Passchier, C.W., and Trouw, R., 2005, Microtectonics: Springer, 366 p., doi:10.1007/978-3-662-08734-3.

Perrotta, M.M., 1996, Potencial aurífero de uma região no vale do Ribeira, São Paulo, estimado por modelagem de dados geológicos, geofísicos, geoquímicos e de sensores remotos num sistema de informações geográficas: Tese de Doutorado. Universidade de São Paulo, 149 p.

Perrotta, M.M., and Campos Neto, M.C., 1999, Potencial aurífero no Vale do Ribeira estimado por meio de um sistema de informações geográficas: Revista Brasileira de Geociências, v. 29, p. 639-648.

Pettke, T., Diamond, L.W., and Kramers, J.D., 2000, Mesothermal gold lodes in the north-western Alps: A review of genetic constraints from radiogenic isotopes: European Journal of Mineralogy, v. 12, p. 213-230, doi:10.1127/ejm/12/1/0213.

Pettke, T., Diamond, L.W., and Villa, I.M., 1999, Mesothermal gold veins and metamorphic devolatilization in the northwestern Alps: The temporal link: Geology, v. 27, p. 641–644, doi:10.1130/0091-7613(1999)027<0641:MGVAMD>2.3.CO;2.

Phillips, G.N., and Groves, D.I., 1983, The nature of Archaean gold-bearing fluids as deduced from gold deposits of Western Australia: Journal of the Geological Society of Australia, v. 30, p. 25-39, doi:10.1080/00167618308729234.

Phillips, G.N., and Powell, R., 2010, Formation of gold deposits: A metamorphic devolatilization model: Journal of Metamorphic Geology, v. 28, p. 689-718, doi:10.1111/j.1525-1314.2010.00887.x.

Phillips, G.N., and Powell, R., 2009, Formation of gold deposits: Review and evaluation of the continuum model: Earth-Science Reviews, v. 94, p. 1-21, doi:10.1016/j.earscirev.2009.02.002.

Picanço, J.L., 2000, Composição isotópica e processos hidrotermais associados aos veios auríferos do maciço granítico Passa Três, Campo Largo, PR: Tese de Doutorado. Universidade de São Paulo, 166 p.

Pinto, G.G., and Borin Junior, T., 1982, Projeto Eldorado. CPRM: Relatório integrado final de

pesquisa.

Pitcairn, I.K., Craw, D., and Teagle, D.A.H., 2014, Metabasalts as sources of metals in orogenic gold deposits: Mineralium Deposita, v. 50, p. 373-390, doi:10.1007/s00126-014-0547-y.

Pitcairn, I.K., Teagle, D.A.H., Craw, D., Olivo, G.R., Kerrich, R., and Brewer, T.S., 2006, Sources of metals and fluids in orogenic gold deposits: Insights from the Otago and Alpine schists, New Zealand: Economic Geology, v. 101, p. 1525-1546, doi:10.2113/gsecongeo.101.8.1525.

Pokrovski, G.S. et al., 2015, Sulfur radical species form gold deposits on Earth: Proceedings of the National Academy of Sciences, v. 112, p. 13484-13489, doi:10.1073/pnas.1506378112.

Pokrovski, G.S., Akinfiev, N.N., Borisova, A.Y., Zotov, A. V., and Kouzmanov, K., 2014, Gold speciation and transport in geological fluids: insights from experiments and physical-chemical modelling: Geological Society, London, Special Publications, v. 402, p. 9-70, doi:10.1144/SP402.4.

Prazeres Filho, H.J., 2005, Caracterização geológica e petrogenética do Batólito Granítico Três Córregos (PR-SP): Geoquímica isotópica (Nd-Sr-Pb), idades (ID-TIMS/SHIRIMP) e δ18 em zircão: Tese de Doutorado. Universidade de São Paulo, 207 p., doi:10.11606/T.44.2005.tde-29102015-131336.

Ramboz, C., Pichavant, M., and Weisbrod, A., 1982, Fluid immiscibility in natural processes: use and misuse of fluid inclusion data. II. Interpretation of fluid inclusion data in terms of immiscibility: Chemical Geology, v. 37, p. 29-48.

Ramsay, J.G., 1980, The crack-seal mechanism of rock deformation: Nature, v. 284, p. 135-139.

Ramsay, J.G., and Huber, M.I., 1983, The techniques of modern structural geology, v. 1: Strain Analysis: Academic Press, 307 p.

Rauchenstein-Martinek, K., Wagner, T., Wälle, M., and Heinrich, C.A., 2014, Gold concentrations in metamorphic fluids: A LA-ICPMS study of fluid inclusions from the Alpine orogenic belt: Chemical Geology, v. 385, p. 70-83, doi:10.1016/j.chemgeo.2014.07.018.

Ribeiro, B. V., Faleiros, F.M., Campanha, G.A.C., Lagoeiro, L., Weinberg, R.F., and Hunter, N.J.R., 2019, Kinematics, nature of deformation and tectonic setting of the Taxaquara Shear Zone, a major transpressional zone of the Ribeira Belt (SE Brazil): Tectonophysics, v. 751, p. 83-108, doi:10.1016/j.tecto.2018.12.025.

Ridley, J.R., and Diamond, L.W., 2000, Fluid chemistry of orogenic lode gold deposits and Implications for Genetic Models, *in* Hagemann, S.G. and Brown, P.E. eds., Reviews in Economica Geology., Gold in 2000.

Robert, F., Boullier, A., and Firdaous, K., 1995, Gold-quartz veins in metamorphic terranes and their bearing on the role of fluids in faulting: Journal of Geophysical Research, v. 100, p. 12,861-12,879.

Robert, F., and Kelly, W.C., 1987, Ore-forming fluids in archean gold-bearing quartz veins at the sigma mine, Abitibi greenstone belt, Quebec, Canada: Economic Geology, v. 82, p. 1464-1482, doi:10.2113/gsecongeo.82.6.1464.

Roedder, E., 1984, Fluid Inclusions, *in* Ribbe, P.H. ed., Reviews in Mineralogy, Vol. 12, Mineralogical Society of America, p. 646, doi:http://www.fluidsurveys.com/.

Rogers, A.J., Kolb, J., Meyer, F.M., and Vennemann, T., 2013, Two stages of gold

mineralization at Hutti mine, India: Mineralium Deposita, v. 48, p. 99-114, doi:10.1007/s00126-012-0416-5.

Röller, K., and Trepmann, C., 2011, Stereo32. Version 1.03:, http://www.ruhr-uni-bochum.de/hardrock/downloads.html.

Sahoo, A.K., Krishnamurthi, R., and Sangurmath, P., 2018, Nature of ore forming fluids, wallrock alteration and P-T conditions of gold mineralization at Hira-Buddini, Hutti-Maski Greenstone Belt, Dharwar Craton, India: Ore Geology Reviews, v. 99, p. 195-216.

Seward, T.M., 1973, Thio complexes of gold and the transport of gold in hydrothermal ore solutions: Geochimica et Cosmochimica Acta, v. 37, p. 379-399, doi:10.1016/0016-7037(73)90207-X.

Shen, P., Pan, H., and Zhu, H., 2016, Two fluid sources and genetic implications for the Hatu gold deposit, Xinjiang, China: Ore Geology Reviews, v. 73, p. 298-312, doi:10.1016/j.oregeorev.2015.03.008.

Shenberger, D.M., and Barnes, H.L., 1989, Solubility of gold in aqueous sulfide solutions from 150 to 350°C: Geochimica et Cosmochimica Acta, v. 53, p. 269-278, doi:10.1016/0016-7037(89)90379-7.

Sibson, R.H., 1990, Conditions for fault-valve behaviour: Geological Society, London, Special Publications, v. 1, p. 15-28.

Sibson, R.H., 2004, Controls on maximum fluid overpressure defining conditions for mesozonal mineralisation: Journal of Structural Geology, v. 26, p. 1127-1136, doi:10.1016/j.jsg.2003.11.003.

Sibson, R.H., Moore, J.M.M., and Rankin, A.H., 1975, Seismic pumping - a hydrothermal fluid transport mechanism: Journal of the Geological Society, v. 131, p. 653-659, doi:10.1144/gsjgs.131.6.0653.

Sibson, R.H., Robert, F., and Poulsen, K.H., 1988, High-angle reverse faults, fluid-pressure cycling, and mesothermal gold-quartz deposits: Geology, v. 16, p. 551-555, doi:10.1130/0091-7613(1988)016<0551:HARFFP>2.3.CO;2.

Sibson, R.H., and Scott, J., 1998, Stress/fault controls on the containment and release of overpressured fluids: examples from gold-quartz vein systems in Juneau, Alaska; Victoria, Australia and Otago, New Zealand: Ore Geology Reviews, v. 13, p. 293-306, doi:10.1016/S0169-1368(97)00023-1.

Siga Jr., O., Basei, M.A.S., Passarelli, C.R., Sato, K., Cury, L.F., and McReath, I., 2009, Lower and Upper Neoproterozoic magmatic records in Itaiacoca Belt (Paraná-Brazil): Zircon ages and lithostratigraphy studies: Gondwana Research, v. 15, p. 197-208, doi:10.1016/j.gr.2008.11.002.

Siga Jr., O., Basei, M.A.S., Sato, K., Passarelli, C.R., Nutman, A., McReath, I., and Prazeres Filho, H.J., 2011, Calymmian (1.50-1.45 Ga) magmatic records in Votuverava and Perau sequences, south-southeastern Brazil: Zircon ages and Nd-Sr isotopic geochemistry: Journal of South American Earth Sciences, v. 32, p. 301-308, doi:10.1016/j.jsames.2011.03.015.

Silva, A.T.F., Francisconi, O., Godoy, A.M., and Batolla Jr, F., 1981, Projeto integração e detalhe geológico no Vale do Ribeira. CPRM: Relatório Final.

Silva, L.C., McNaughton, N.J., Armstrong, R., Hartmann, L.A., and Fletcher, I.R., 2005, The neoproterozoic Mantiqueira Province and its African connections: A zircon-based U-Pb geochronologic subdivision for the Brasiliano/Pan-African systems of orogens: Precambrian

Research, v. 136, p. 203–240, doi:10.1016/j.precamres.2004.10.004.

Span, R., and Wagner, W., 1996, A new equation of state for carbon dioxide covering the fluid region from the triple-point temperature to 1100 K at pressures up to 800 MPa: Journal of Physical and Chemical Reference Data, v. 25, p. 1509-1596.

Spooner, E.T.C., Bray, C.J., Wood, P.., Burrows, D.R., and Callan, N.., 1985, Au-quartz vein and Cu-Au-Ag-Mo-anhydrite mineralization, Hollinger-McIntyre Mines, Timmins, Ontario: del ^{13}C values (McIntyre), fluid inclusion gas chemistry, pressure (depth) estimation, and H_2O-CO_2 phase separation as a precipitation and dilation mechanism: Ont. Geol. Surv. Misc., v. 127, p. 229-246.

Steele-MacInnis, M., Ridley, J., Lecumberri-Sanchez, P., Schlegel, T.U., and Heinrich, C.A., 2016, Application of low-temperature microthermometric data for interpreting multicomponent fluid inclusion compositions: Earth-Science Reviews, v. 159, p. 14-35, doi:10.1016/j.earscirev.2016.04.011.

Stüwe, K., 1998, Tectonic constraints on the timing relationships of metamorphism, fluid production and gold-bearing quartz vein emplacement: Ore Geology Reviews, v. 13, p. 219-228, doi:10.1016/S0169-1368(97)00019-X.

Sun, X., Wei, H., Zhai, W., Shi, G., Liang, Y., Mo, R., Han, M., Yi, J., and Zhang, X., 2016, Fluid inclusion geochemistry and Ar-Ar geochronology of the Cenozoic Bangbu orogenic gold deposit, southern Tibet, China: Ore Geology Reviews, v. 74, p. 196-210, doi:10.1016/j.oregeorev.2015.11.021.

Tan, J. et al., 2017, Noble gases in pyrites from the Guocheng-Liaoshang gold belt in the Jiaodong province: Evidence for a mantle source of gold Jun: Chemical Geology, p. xxx, doi:10.1016/j.chemgeo.2017.09.027.

Tomkins, A.G., 2013, On the source of orogenic gold: Geology, v. 41, p. 1255-1256, doi:10.1130/focus122013.1.

Tomkins, A.G., 2010, Windows of metamorphic sulfur liberation in the crust: Implications for gold deposit genesis: Geochimica et Cosmochimica Acta, v. 74, p. 3246-3259, doi:10.1016/j.gca.2010.03.003.

Treloar, P.J., Lawrence, D.M., Senghor, D., Boyce, A., and Harbidge, P., 2014, The Massawa gold deposit, Eastern Senegal, West Africa: an orogenic gold deposit sourced from magmatically derived fluids? Geological Society, London, Special Publications, v. 393, doi:10.1144/SP393.12.

Turner, F.J., and Weiss, L.E., 1963, Structural analysis of metamorphic tectonites: New York, McGraw Hill, 545 p.

Vearncombe, J.R., 1993, Quartz vein morphology and implications for formation depth and classification of Archaean gold-vein deposits: Ore Geology Reviews, v. 8, p. 407-424, doi:10.1016/0169-1368(93)90036-X.

Wang, Z.L. et al., 2015, Fluid immiscibility and gold deposition in the Xincheng deposit, Jiaodong Peninsula, China: A fluid inclusion study: Ore Geology Reviews, v. 65, p. 701-717, doi:10.1016/j.oregeorev.2014.06.006.

Weber, W., Siga, O., Sato, K., Neto, J.M.R., Basei, M.A.S., and Nutman, A.P., 2004, A Formação Água Clara na região de Araçaíba - SP: Registro U-Pb de uma bacia Mesoproterozoica: Geologia USP - Serie Cientifica, v. 4, p. 101-110, doi:10.5327/S1519-874X2004000100007.

White, R.W., Powell, R., and Johnson, T.E., 2014, The effect of Mn on mineral stability in metapelites revisited: new a-x relations for manganese-bearing minerals: Journal of Metamorphic Petrology, v. 4, p. e868, doi:10.1111/jmg.12.

Whitney, D.L., and Evans, B.W., 2010, Abbreviations for names of rock-forming minerals: American Mineralogist, v. 95, p. 185-187, doi:10.2138/am.2010.3371.

Wilkins, R.W.T., and Barkas, J.P., 1978, Fluid inclusions, deformation and recrystallization in granite tectonites: Contributions to Mineralogy and Petrology, v. 65, p. 293-299.

Yang, L.Q., Deng, J., Guo, L.N., Wang, Z.L., Li, X.Z., and Li, J.L., 2016, Origin and evolution of ore fluid, and gold-deposition processes at the giant Taishang gold deposit, Jiaodong Peninsula, eastern China: Ore Geology Reviews, v. 72, p. 585-602, doi:10.1016/j.oregeorev.2015.08.021.

Yang, L.Q., Guo, L.N., Wang, Z.L., Zhao, R.X., Song, M.C., and Zheng, X.L., 2017, Timing and mechanism of gold mineralization at the Wang'ershan gold deposit, Jiaodong Peninsula, eastern China: Ore Geology Reviews, v. 88, p. 491-510, doi:10.1016/j.oregeorev.2016.06.027.

Yardley, B.W.D., and Cleverley, J.S., 2013, The role of metamorphic fluids in the formation of ore deposits: Geological Society, London, Special Publications, v. 393, p. 117-134, doi:10.1144/SP393.5.

Zhang, Y.G., and Frantz, J.D., 1987, Determination of the homogenization temperatures and densities of supercritical fluids in the system NaCl-KCl-$CaCl_2$-H_2O using synthentic fluid inclusions: Chemical Geology, v. 64, p. 335-350.

Zoheir, B., and Moritz, R., 2014, Fluid evolution in the El-Sid gold deposit, Eastern Desert, Egypt: Geological Society, London, Special Publications, v. 402, p. 147-175, doi:10.1144/SP402.3.

Universidade de São Paulo

Pós Graduação em Geociências
Programa de Mineralogia e Petrologia